ISBN 978-82-326-0618-4 (printed version)
ISBN 978-82-326-0619-1 (electronic version)
ISSN 1503-8181

Doctoral theses at NTNU, 2014:353

Mari Helene Farstad

Titania Thin Films on Gold and Palladium Surfaces

Structure and Properties

Mari Helene Farstad

Doctoral Thesis

Doctoral theses at NTNU, 2014:353

NTNU
Norwegian University of
Science and Technology
Faculty of Natural
Sciences and Technology
Department of Physics

NTNU – Trondheim
Norwegian University of
Science and Technology

NTNU – Trondheim
Norwegian University of
Science and Technology

NTNU

Mari Helene Farstad

Titania Thin Films on Gold and Palladium Surfaces

Structure and Properties

Thesis for the degree of Philosophiae Doctor

Trondheim, November 2014

Norwegian University of Science and Technology
Faculty of Natural Sciences and Technology
Department of Physics

NTNU – Trondheim
Norwegian University of
Science and Technology

NTNU
Norwegian University of Science and Technology

Thesis for the degree of Philosophiae Doctor

Faculty of Natural Sciences and Technology
Department of Physics

© Mari Helene Farstad

ISBN 978-82-326-0618-4 (printed version)
ISBN 978-82-326-0619-1 (electronic version)
ISSN 1503-8181

Doctoral theses at NTNU, 2014:353

Printed by Skipnes Kommunikasjon as

Abstract

Motivated by the catalytic properties of titanium dioxide (TiO_2), palladium (Pd) and gold (Au) combined with TiO_2, growth and properties of TiO_x thin films on Au(111), Pd(100) and Pd(111) have been investigated. The TiO_x thin films were grown by chemical vapor deposition (CVD) using titanium (IV)isopropoxide (TTIP) as precursor. For the TiO_x structures found on Au(111) the interaction with water have been studied and for the TiO_x structures on the two Pd surfaces the oxidation and reduction behavior were studied.

High resolution photoelectron spectroscopy (HRPES), scanning tunneling microscopy (STM) and low energy electron diffraction (LEED) was used to characterize the structure of the TiO_x thin films. Additionally, density functional theory (DFT) calculations were used to investigate a Ti-Pd alloy formation in the Pd(100) surface.

On Au(111) four different TiO_x structures were characterized, two partially oxidized wetting layers, Honeycomb (HC) and Pinwheel (PW), and two fully oxidized TiO_2 phases, Star and TiO_2(B). The HC phase and the star phase are both grown directly by TTIP deposition, while the PW and TiO_2(B) phases require a post annealing step.

The water interaction with the TiO_x phases on Au(111) was found to be different for all four phases, water dissociation was observed on three of the phases, Star, PW and TiO_2(B). The Star phase showed a water dissociation comparable to that of rutile TiO_2(110), whereas the TiO_2(B) phase only showed water dissociation in connection to domain boundaries. The PW phase got significantly oxidized during water dissociation.

The growth of TiO_x on Pd(100) and Pd(111) follow the same pattern on both surfaces. Initially a surface alloy is observed before a partially oxidized wetting layer is formed. Finally a fully oxidized TiO_2 phase is formed on top. Post-oxidation of the reduced wetting layers reveal additional, fully oxidized phases which may be reduced back to the respective partially oxidized wetting layers by annealing. Annealing of the reduced wetting layers results in removal of the oxygen and formation of surface alloys. Although the growth and oxidation/reduction behaviors are similar for the two Pd surfaces, the atomic structures of the different TiO_x phases are not the same for the two surface orientations.

Acknowledgments

I would like to thank my main supervisor, Professor Anne Borg at NTNU, for guiding and helping me through these four years. Also my co-supervisor Professor Anders Sandell at Uppsala University has been of great help especially during beamtimes and article writing, and last my other co-supervisor Associate Professor Erik Wahlström for helping out when the laboratories did not do quite what they were supposed to do.

During my PhD I have spent many weeks at the Max IV Laboratory conducting research at the beamlines D1011, I311 and I511 and I would like to give a big thanks to the staff at these beamlines who have always been very helpful. In addition to the beamline staff I would never have survived these beamtimes without the help of my colleagues, Davide, Andreas, Lars Erik, Marie, Johan and Vasco, thank you!

I would also like to thank all my friends in Lund for stopping by the beamline and making my stays there much more enjoyable:)

On a different note I would like to thank Alexandra and Paul Anton for letting me and Håvard stay at their place when our plumber thoroughly proved that everything takes more time than what you expect.

Last, I would like to thank my friends and family for standing by me and supporting me through all of this. Es-

pecially Håvard for reading and correcting my manuscripts and frequently arranging social gatherings in my apartment.

List of papers

Paper I **Chemical vapor deposition of ordered TiO_x nanostructures on Au(111)**
D. Ragazzon, A. Schaefer, M.H. Farstad, L.E. Walle, P. Palmgren, A. Borg, P. Uvdal, and A. Sandell.
Surface Science **617** (2012) 211-217

Paper II **Growth of TiO_2(B)(001) on Au(111) by Chemical Vapor Deposition**
D. Ragazzon, M.H. Farstad, A. Schaefer, L.E. Walle, P. Uvdal, A. Borg, and A. Sandell.
Surface Science, DOI: 10.1016/j.susc.2014.10.011

Paper III **Structure of a pinwheel-like TiO_x single layer phase on Au(111)**
D. Ragazzon, M.H. Farstad, A. Schaefer, L.E. Walle, P. Uvdal, P. Palmgren, A. Borg, and A. Sandell.
In manuscript

Paper IV **Water adsorption on TiO_x thin films grown on Au(111)**
M.H. Farstad, D. Ragazzon, L.E. Walle, A. Schaefer, A. Sandell, and A. Borg.
Submitted to The Journal of Physical Chemistry C

Paper V **TiO_x thin films grown on Pd(100) by chemical vapor deposition**
M.H. Farstad, D. Ragazzon, H. Grönbeck, M.D. Strømsheim, J. Gustafson, A. Sandell, and A. Borg.
In manuscript

Paper VI **Growth and oxidation/reduction of TiO_x thin films on Pd(111)**
M.H. Farstad, D. Ragazzon, M.D. Strømsheim, J. Gustafson, A. Sandell, and A. Borg.
In manuscript

My contribution to the papers

All papers are the result of team work. I participated in the experimental work and discussions of the data for all papers. I had larger responsibility for papers **IV-VI** where I also did the analysis of the data and wrote the manuscripts. The DFT-calculations in paper **V** were conducted by H. Grönbeck.

Papers not included in this Thesis

1. **H_2 reduction of surface oxides on Pd-based membrane model systems - The case of Pd(100) and $Pd_{75}Ag_{25}$(100)**
   V.R. Fernandes, J. Gustafson, M.H. Farstad, L.E. Walle, S. Blomberg, E. Lundgren, H. Venvik, and A. Borg.
   Applied Surface Science **313** (2014) 794-803

2. **Reduction behavior of oxidized Pd(100) and $Pd_{75}Ag_{25}$(100) surfaces using CO**
   V.R. Fernandes, J. Gustafson, I.H. Svennum, M.H. Farstad, L.E. Walle, S. Blomberg, E. Lundgren, and A. Borg.
   Surface Science **621** (2013) 31-39

3. **Controlled modification of nanoporous gold: Chemical Vapor deposition of TiO_2 in ultra-high vacuum**
   A. Schaefer, D. Ragazzon, L.E. Walle, M.H. Farstad, A. Wichmann, M. Bäumer, A. Borg, and A. Sandell.
   Applied Surface Science **282** (2013) 439-443

4. **Surface composition of clean and oxidized $Pd_{75}Ag_{25}$(100) from photoelectron spectroscopy and density functional theory calculations**
   L.E. Walle, H. Grönbeck, V.R. Fernandes, S. Blomberg, M.H. Farstad, K. Schulte, J. Gustafson, J. Andersen, E. Lundgren, and A. Borg.
   Surface Science **606** (2012) 1777-1782

Contents

Abbreviations

2D 2-dimensional.

3D 3-dimensional.

CVD Chemical Vapor Deposition.

DFT Density Functional Theory.

EMFP Electron inelastic Mean Free Path.

fcc face centered cubic.

FWHM full width at half maximum.

HC Honeycomb.

LEED Low Energy Electron Diffraction.

MCP Micro-Channel Plate.

PES Photoelectron Spectroscopy.

PW Pinwheel.

SCLS surface core level shift.

STM Scanning Tunneling Microscopy.

TTIP Titanium (IV)isopropoxide.

UHV Ultra High Vacuum.

UV ultraviolet.

Part I

Introduction

1 Motivation

"I would like to start by emphasizing the importance of surfaces. It is at a surface where many of our most interesting and useful phenomena occur. We live for example on the surface of a planet. It is at a surface where the catalysis of chemical reactions occur. It is essentially at a surface of a plant that sunlight is converted to a sugar. In electronics, most if not all active circuit elements involve non-equilibrium phenomena occurring at surfaces. Much of biology is concerned with reactions at a surface."

- Walter Brattain

As Walter Brattain pointed out when he and his coworkers received their Nobel Prize in 1956, surfaces are everywhere and they play an important role in many aspects of our lives. With the progression of technology the possibility to tailor the surfaces around us has emerged. Today it is not only possible to study the atomic structure of surfaces it is also possible to alter and create new surfaces with tailored properties. Water repellent clothing, self-cleaning windows and most heterogeneous catalysts are examples of surfaces that have been tailored to achieve a certain property.

Titania has received a lot of attention since it was discovered that water dissociates on the surface under ultraviolet (UV) light exposure [1]. Since then many other

properties have also been discovered, such as UV dependent hydrophilicity [2], degradation of volatile organic compounds [3] and antibacterial properties [4, 5], even cancer cells may be targeted [6]. When titania is combined with metals intriguing catalytic properties have been observed [7, 8].

Single crystals of TiO_2 are usually not particularly applicable for use in most of these applications, requirements such as of large surface area, electron transport and integration in liquids are common. Nanostructures such as nanoparticles, thin films, nano-tubes and so on are much better suited to fulfill the requirements set by the applications. In many cases is it desirable to combine metals with TiO_2, either for practical reasons or in order to create or improve a desired functionality. This is often the case in catalysis where TiO_2 are used as support for metal nanoparticles, but also the inverse system with nanoparticles of TiO_2 nanoparticles on metals have proven to be a good candidate as a catalyst [9] in addition to provide a better understanding of the detailed mechanisms involved in the relevant catalytic reactions.

Water is an integral part in many of the applications of TiO_2, either directly as in water dissociation under UV-light or other catalytic reactions involving water as one of the reactants but also indirectly when water is used as solvent or in water purification treatments. Sometimes even the presence of water may promote catalytic reactions which do not involve water to begin with [10]. As a result the water interaction with the benchmark surface, rutile $TiO_2(110)$, have been studied extensively. It has been found that water dissociation takes place on both stoichiometric TiO_2 [11–16] and in oxygen vacancies in the surface row-structure [17]. Because of the central role of water dissociation for many of the applications of TiO_2 is it also important to charac-

terize the water-interaction with the various nanostructured forms of TiO_x which is being developed.

2 Sample systems

"There's plenty of room at the bottom."

- Richard P. Feynman

The material samples used in this Thesis consist of a metal single crystal substrate, either Gold (Au) or Palladium (Pd) with thin films of titanium oxide grown on top. For some of these thin films the interaction with water was investigated more closely and for others the oxidation and reduction behavior was studied in more detail. In the following the metal single crystals and Titanium oxides will be presented.

2.1 Single crystal substrates

Metal single crystals are commonly used as substrates when the structure and properties of thin films and nanoparticles are addressed. Single crystals provide regular, well defined, flat surfaces, which are necessary for characterization down to the atomic scale. The crystal structure of both Au and Pd are face centered cubic (fcc). The fcc unit cell and the corresponding (111) and (100) surfaces are illustrated in Fig. 2.1. The (111) surface are the most closely packed surface with six nearest neighbors, whereas the (100) surface is less densely packed with four nearest neighbors. Both surfaces has an atomic spacing of $a/\sqrt{2}$ where a is the lattice

constant.

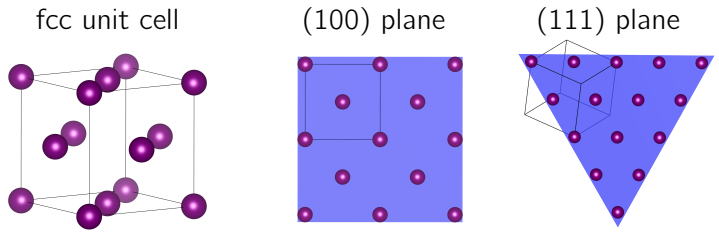

Figure 2.1. Illustrations of the fcc unit cell and the related (100) and (111) planes.

Different metals also exhibit a variable degree of chemical interaction with other substances, which is linked to the filling of their electronic bands. Metals with filled d-bands are least likely to react with their environment and are therefore referred to as noble metals. These metals are found in group 11 of the periodic table. Au is one of the noble metals and in its normal crystal form considered to be quite inert. Pd on the other hand, which can be found in group 10 is a well known catalyst for oxidation reactions.

2.2 Titanium dioxide

Titanium dioxide (TiO_2) is a semiconductor with a band gap around 3 eV, dependent on the crystal phase. In nature TiO_2 is found as a mineral and exists in three different crystalline phases, Rutile, Anatase and Brookite. In addition two more phases have been found in laboratories, lepidocrocite nanosheets [18, 19] and TiO_2(B) [20].

Titanium dioxide, TiO_2, is a material with a variety of intriguing properties and a wide range of applications. It is most commonly used as white pigment in paint, but also used for UV protection in sun screen, heterogeneous cataly-

sis, photocatalysis, gas sensor, corrosion protective coating, optical coatings and electrical components [21].

Many of these applications do not use TiO_2 in its crystal form, nano-particles, nano-structures and thin films are much more applicable and more versatile in terms of combining TiO_2 with other materials. In this Thesis TiO_x thin films have been investigated.

2.3 Thin films

Thin films are usually made by depositing and thereby growing the thin film material on a substrate. A thin film can be anything from a monolayer covering only a part of the substrate to a several nanometers thick film. The structure of thin films are influenced by the structure as well as electronic and chemical properties of the substrate upon which they are grown. Dependent on the combination of substrate and thin film materials and growth parameters it is possible to form both ordered and unordered structures. There may be formation of thin layers covering the entire substrate, islands which are several layers thick or a combination where islands form on top of of initially formed layers [22].

Thin films which are grown on single metal crystals generally have properties which makes them suitable for investigations by surface techniques. Semiconducting or insulating materials which normally would be challenging to study with techniques which require conducting samples such as Scanning Tunneling Microscopy (STM), Photoelectron Spectroscopy (PES) and Low Energy Electron Diffraction (LEED) may be studied in thin film form grown on conductive substrates.

3 Experimental techniques

"It's of no use whatsoever[...] this is just an experiment that proves Maestro Maxwell was right - we just have these mysterious electromagnetic waves that we cannot see with the naked eye. But they are there."

- Heinrich Hertz

In order to study and characterize TiO_x thin films deposited on Au(111), Pd(100) and Pd(111) three main experimental techniques were used: PES, STM and LEED. Basic principles and experimental considerations for these techniques will be presented in this chapter, as well as the techniques related to the sample preparation.

3.1 Photoelectron Spectroscopy

PES is used to measure the energy distribution of electrons in a sample. From this, information about the chemical composition and the chemical state, as well as electronic properties, can be obtained.

3.1.1 General idea and basic principle

PES is a surface sensitive characterization technique based on the photoelectric effect, in which electrons are emitted from a material when a photon is absorbed [23]. The photoelectric effect was discovered by Heinrich Hertz in 1887 [24], but it was not explained until Albert Einstein formulated the quantum theory of light in 1905 [25]. In order for an electron to be emitted, the incoming photon has to have sufficient energy to release the electron from the material. The required energy can be expressed as

$$h\nu = E_B + E_{kin} + \phi_s, \tag{3.1}$$

where $h\nu$ is the photon energy, E_B is the binding energy of the electron, E_{kin} is the kinetic energy of the emitted electron and ϕ_s is the work function of the sample. The work function is the energy required to move an electron from the fermi level, E_F, into vacuum.

The photoemission process is illustrated in Fig. 3.1, where also the relation between the electron energy levels in the sample and the measured spectrum is indicated. The measured kinetic energy of the electron, E'_{kin}, is slightly different from the E_{kin} the electrons have when they leave the sample due to the work function of the analyzer, ϕ_A, which is usually higher than the sample dependent ϕ_s. E_B can be determined from the known ϕ_A and $h\nu$, and the measured E'_{kin} by

$$E_B = h\nu - E'_{kin} - \phi_A. \tag{3.2}$$

The core level binding energy

Due to the unique electronic band structure in every material, any chemical element can be identified by its signature

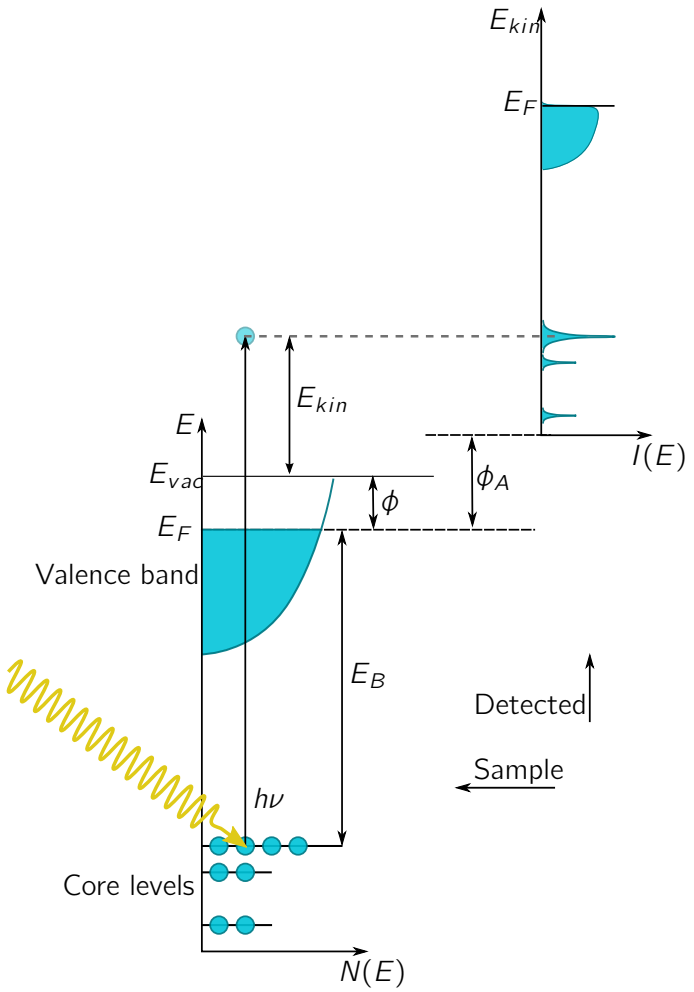

Figure 3.1. Illustration of the photoemission process and the coupling between the sample and the measured spectrum. The incoming photons excites electrons from both valence band and core levels. The electrons that gain enough energy to escape the surface can be detected, and their E'_{kin} measured. The figure is adapted from [23].

core level peaks, thus providing the powerful chemical sensitivity of the PES technique.

A more detailed picture of the photoemission process reveals that the measured E_B is the difference between total energies of the initial state with N electrons, E_i^N, and the final state with $N-1$ electrons, E_f^{N-1},

$$E_B = E_f^{N-1} - E_i^N. \tag{3.3}$$

This may look like a simple equation, however, the exact total energies are not easily obtained analytically, over the years several approximations have been developed. Even though these approximation are not really used to calculate E_B any more, they can be useful in terms of understanding exactly what contributes to E_B. A crude, but well known initial state approximation is the Koopmans' approximation which says that the remaining $N-1$ electrons are unaffected by the photoemission event [26]. In other words relaxation energies are not taken into account. This results in E_B equal to the negative orbital energy, ϵ_{orb}, as calculated by Hartree-Fock [27] of the photoemitted electron.

In order to obtain a more accurate approximation relaxation energies, E_R, which are final state effects should also be considered. There are two main contributions to E_R, the relaxation of the orbitals of the atom from which the electron was emitted, and a charge redistribution in the crystal [23, 28, 29]. This gives

$$E_B = -\epsilon_{orb} - E_R. \tag{3.4}$$

The today most used approach to estimate the E_B is to use Density Functional Theory (DFT) to calculate the total energies necessary in Eq. (3.3) directly. DFT are based on the principle that any property of a system consisting of interacting particles is a functional of the ground state density, with appropriate approximations for the ground state

functionals this is a very powerful method which have shown good agreement with experimental results [30–33].

Core level shifts

The core level electrons are localized and do not participate directly in the bonding to neighboring atoms, they are however, influenced by the surrounding electrical potential. Different types of chemical bonds and neighboring atoms may alter the electronic potential surrounding the atoms and thereby also the observed binding energies of the core level electrons. A low charge concentration around an atom will result in a lower potential and thereby lower kinetic energy and subsequently a higher binding energy for the emitted photoelectron [32]. This can be observed as chemical shifts in the PES spectrum. An example is the variable oxidation state of Ti in TiO_x thin films Fig. 3.2. The chemical state is related to the initial state of the system and is therefore considered to be an initial state effect.

An example of a final state effect is hole screening. When the photoelectron is emitted there is a hole left in the electronic structure where the photoelectron used to be, disrupting the local charge balance. The electrons in the conduction band will shift in order to correct the charge balance. This effect is strongest in metals where there are conduction band electrons readily available [32, 34]. This effect can be observed as a small shift in E_B for thin film growth where the access to conduction electrons changes with film thickness.

Another core level shift observed for surfaces is the surface core level shift (SCLS). The surface atoms have a lower coordination number than their bulk counterparts, *i.e.* they have fewer neighboring atoms. Dependent on the material both positive and negative SCLS can be observed [34].

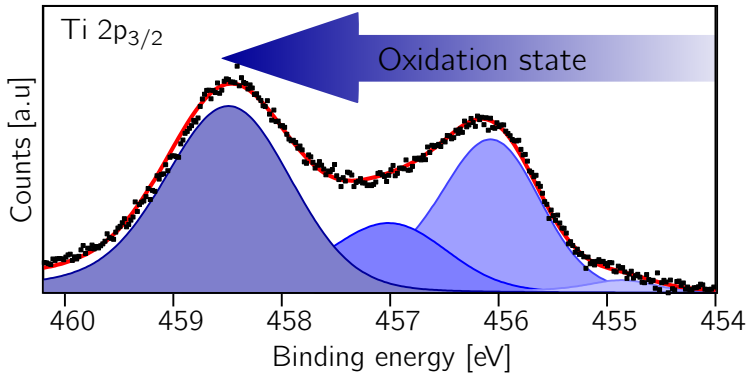

Figure 3.2. PES spectrum of the Ti $2p_{3/2}$ peak. The sample consists of Ti in four different chemical environments. Starting from the right there is a Ti alloy, the next three Ti peaks have increasing oxidationstate, where the last one is Ti^{4+}.

3.1.2 Experimental considerations

Surface sensitivity

In order to analyze and truly understand the PES spectra resulting from the detected electrons there are some secondary effects which need to be considered. On their way out of the sample the electrons may interact with other electrons, get scattered or create plasmons, resulting in reduction of the electron E_{kin}. In fact, they can only travel a limited distance before they are reabsorbed by the material. This length is called the Electron inelastic Mean Free Path (EMFP). The EMFP for electrons with kinetic energy up to 2 keV are plotted for some metals in Fig. 3.3 together with the theoretical predictions of Penn [35]. The relevant electron kinetic energy interval for PES is from about 10 to 2000 eV. In this interval the EMFP varies between 0.5 nm

and 2 nm, revealing that PES is quite surface sensitive. However, for studying the actual surface, thin films and adsorbates on the surface it is still necessary to maximize the surface sensitivity. In Fig. 3.3 a minimum EMFP is observed for kinetic energies at about 50 eV, which can be exploited by tuning the photon energy accordingly.

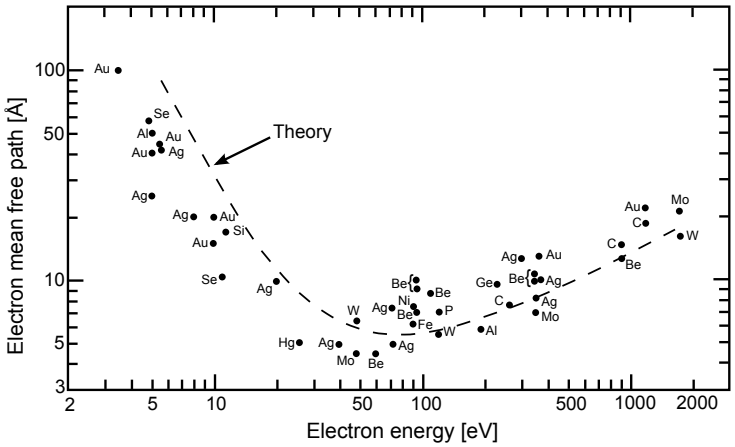

Figure 3.3. EMFP plotted against kinetic energy. Theory by Penn [35]. Reproduced from [36].

An additional way to increase the surface sensitivity is to change the emission angle recorded by the detector. Normally the detector is positioned so that the electrons emitted normal to the surface are detected in order to maximize the count rate. However, if the sample is tilted with respect to the detector, the electrons from the bulk of the sample will get a longer path to the surface and the surface to bulk signal ratio will increase.

Signal attenuation

If a surface is covered by an overlayer the PES signal will be attenuated exponentially with the EMFP, λ, of the overlayer as decay constant [23]. This gives the following expression for the measured intensity, I_s, of the substrate covered by an overlayer with thickness, a:

$$I_s = I_0 e^{-a/\lambda}, \tag{3.5}$$

where I_0 is the measured intensity of the substrate without the overlayer.

Lineshape

To the first approximation the core level PES peaks should be one narrow line. There is however, several aspects which contribute to a broadening of this line. Instrumental limitations, core hole lifetime, phonon excitation, and satellite formation all influence the line shape of the core level PES peaks. The broadening is usually divided into three different types, Gaussian, Lorentzian and asymmetric.

There are several aspects which contribute to the Gaussian broadening. Instrumental uncertainties such as detector resolution and the accuracy of the monochromator, phonon interaction, small chemical shifts and disorder are all assumed to contribute to a Gaussian broadening given by

$$I_G = I_0 e^{-\ln 2 \frac{(E-E_0)^2}{4\sigma^2}}, \tag{3.6}$$

where σ is the Gaussian full width at half maximum (FWHM).

The Lorentzian broadening is caused by the finite lifetime of the exited state after the photoemission event. The Heisenberg uncertainty principle [37] states that the energy uncertainty, ΔE, of a state with lifetime τ has to be at least

$$\Delta E = \frac{\hbar}{\tau}. \tag{3.7}$$

The lifetime of the exited state is given by

$$I(t) = I(0)e^{-2\gamma t}, \tag{3.8}$$

where t=0 is the time of excitation [27]. The Intensity function with respect to energy can then be found by a Fourier transform of Eq. (3.8) with respect to energy and gives

$$I_L(E) = I_0 \frac{\gamma^2}{(E - E_0)^2 - \gamma^2}, \tag{3.9}$$

which is a Lorentzian distribution with γ as FWHM [38].

Interactions with between the core hole and conduction electrons may create electron-hole pairs in the conduction band which also affect the lineshape. This leads to an energy loss for the photoelectron which can be observed as an asymmetric lineshape [23]. For metals this effect combined with the lifetime broadening has been successfully by Doniach and Sunjic [39], the resulting lineshape are described by

$$I_{DS}(E) = I_0 \frac{\Gamma(1-\alpha)\cos\left[\frac{\pi\alpha}{2} + (1-\alpha)\arctan\left(\frac{E-E_0}{\gamma}\right)\right]}{[(E-E_0)^2 + \gamma^2]^{\frac{(1-\alpha)}{2}}}, \tag{3.10}$$

where Γ represents the Γ-function, α is the asymmetry parameter and 2γ is the lifetime width. For $\alpha = 0$ reduces I_{DS} to I_L.

Background

In addition to PES peaks the PES spectrum also consists of a background of inelastically scattered electrons. Under

the PES peaks this background is usually modeled by either a straight line, a Shirley [40, 41] or a Tougaard [42] background. The different methods are compared in [43].

3.1.3 Experimental setup

A typical experimental setup for PES measurements is illustrated in Fig. 3.4. It consists of a suitable photon source, an electron energy analyzer and detector, and an Ultra High Vacuum (UHV) chamber. There are two reasons to for using a UHV chamber, one arises from the need to detect electrons and measure their kinetic energy. Electrons do not travel very far in air before they are adsorbed or scattered by gas molecules. Henceforth, in order for these electrons to reach the detector the distance between the sample and the detector has to be in UHV. The other reason is the cleanliness of the sample, in order to study the surface of the sample it has to be clean, without any adsorbates. In order to get a time frame of 1 hour or more before a monolayer of adsorbates may have formed is it necessary to keep the sample in pressures below 10^{-9} mbar, usually pressures in the low 10^{-10} mbar range is used.

Photon source

When it comes to photon sources there are three main types to choose from, x-ray anode, noble gas-discharge lamps and synchrotron radiation. The x-ray anodes are well suited for core level spectroscopy with photon energies of 1486.6 eV and 1253.6 eV for Mg and Al anodes, respectively. The energy resolution is not the best, but combined with a monochromator a line width of about 0.35 eV can be reached [44]. The gas-discharge lamps have discrete photon energies in the range of 10 - 50 eV with line widths

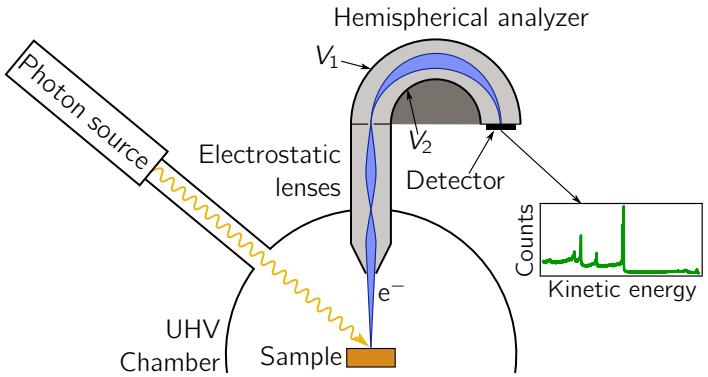

Figure 3.4. Illustration of the experimental setup for PES measurements.

of only a few meV dependent on the gas used [23, 45]. This makes them well suited for valence band measurements. The synchrotron radiation is the most versatile photon source with a continuous range of photon energies ranging from ultraviolet radiation to hard x-rays and a very high flux and brilliance compared to the other sources. All PES results presented in this Thesis have been obtained by using synchrotron radiation and a more detailed description of this type of radiation is therefore included.

Synchrotron radiation is based on the radiation created by acceleration of electrons. When an electron is accelerated it emits electromagnetic radiation in all directions, except for the direction of the accelerating force, as illustrated in the electrons frame of reference in Fig. 3.5(a). According to the special theory of relativity the radiation from an electron moving at relativistic velocity apperas different to a stationary observer. The resulting radiation from an accelerated electron as observed in the laboratory is illustrated in stationary frame of laboratory in Fig. 3.5(b). The resulting cone of electromagnetic radiation has an opening

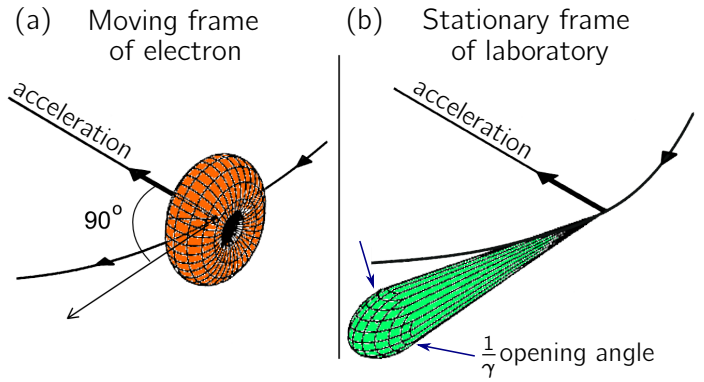

Figure 3.5. Radiation emitted from an accelerated electron, as seen from (a) the moving frame of the electron and (b) the stationary frame of the laboratory [46].

angle, $1/\gamma$, given by

$$\frac{1}{\gamma} = \sqrt{1 - \left(\frac{v}{c}\right)^2} \tag{3.11}$$

where v is the electron velocity and c is the speed of light.

So, in order to get an intense and narrow cone of electromagnetic radiation it is necessary to accelerate electrons at a velocity very close to c. In Fig. 3.6 a general setup of a synchrotron is illustrated. The electrons are created in the electron gun, and then accelerated by a linear accelerator, the next step is a booster ring where they are further accelerated up to about 99% of c [47] before entering the storage ring. In the storage ring the energy of the electrons is maintained by a RF cavity The storage ring consists of combination of straight and bent segments, which are both used to create electromagnetic radiation.

As indicated in Fig. 3.5, acceleration of electrons which are already moving at constant relativistic speed can be obtained by applying a magnetic field perpendicular to the

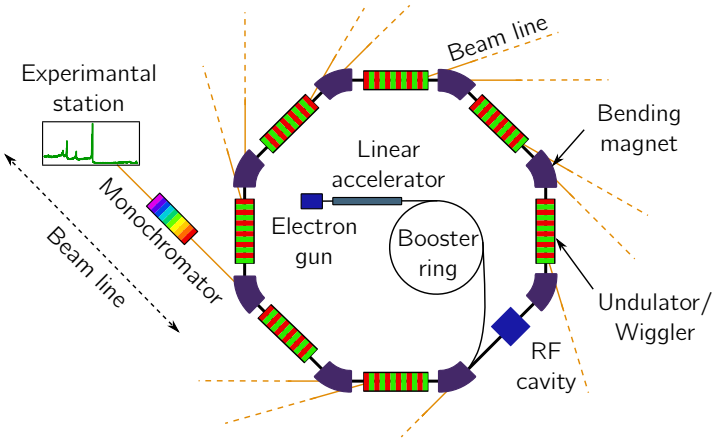

Figure 3.6. Schematic illustration of the main components in a synchrotron.

electron trajectory. There are two different approaches to achieve this, either by using a bending magnet or an insertion device, that is an undulator or a wiggler. Both approaches rely on the principle that charged particles moving in a magnetic field will experience a force normal to the direction of movement [48]. Schematics of the three different devices and the resulting photon spectrum is displayed in Fig. 3.7.

The bending magnets consists of one pair of magnets creating a magnetic filed which then changes the direction of the electrons and thereby electromagnetic radiation is emitted. A higher flux is achieved by insertion devices where the magnets are arranged in a way that makes the electrons follow an oscillating trajectory, emitting radiation at every turn. Out of the two devices the wiggler has the strongest magnetic fields and thereby are also the electron path deflected more strongly resulting in a relatively large maximum angle between the actual electron path and a straight line.

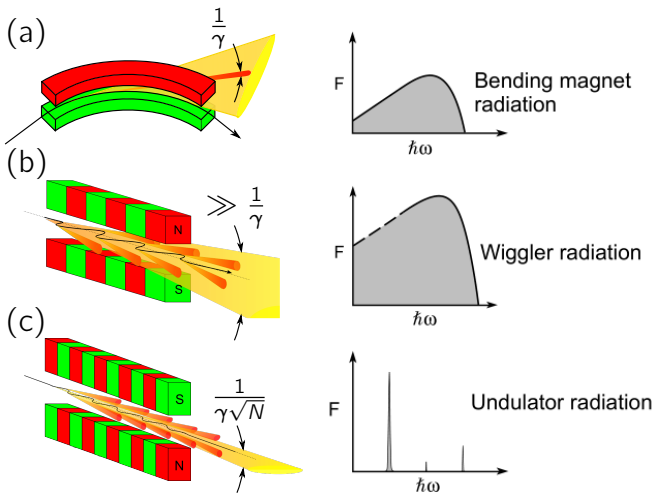

Figure 3.7. Electromagnetic radiation created by (a) a bending magnet, (b) a wiggler and (c) an undulator. N is the number of periods in the magnetic field. Adapted from [46, 49]

In the undulator the oscillations are of smaller amplitude, the maximum divergence from a straight line is kept much smaller than $1/\gamma$, meaning that the emitted radiation points in the same direction at all times. This results in a much higher flux, and with the right magnetic field strength a coherent beam with a narrow frequency distribution is obtained. For both undulators and wigglers the magnetic filed can be tuned and thereby also the wavelength of the emitted radiation. This is not possible for the bending magnets as their magnetic field is determined by the curvature of the ring.

The beamlines

The function of the beamlines is to select the desired photon wavelength and focus and guide the radiation gener-

ated by the bending magnets and insertion devices to the experimental station. The wavelength selection is done by a monochromator. The monochromatic radiation is the focused and directed by a series of mirrors, gratings and slits into the sample in the experimental chamber.

The electron analyzer

The often vital components in the experimental setup of PES is the energy analyzer, illustrated in Fig. 3.1 and the detector. Before the electrons can be detected their kinetic energy has to be determined. This is done by a combination of a electrostatic lenses and a hemispherical analyzer. The hemispherical analyzer consists of two concentric metal hemispheres as illustrated in Fig. 3.4. The hemispheres are biased, at two different voltages, V_1 for the outer and V_2 for the inner hemisphere with $V_2 > V_1$. This gives the electrons a circular trajectory and the electrons with the right E_k, the pass energy, will be focused onto the detector. The resolution of the analyzer is dependent on the pass energy [23]. This means that if the pass energy is ramped in order to measure electrons with a different E_k the energy resolution of the PES spectra would vary with the energy, which is not desirable. Constant energy resolution is obtained by keeping the pass energy constant throughout the scan and then rather adjust the E_k of the incoming electrons by a retardation field which is the main purpose of the electrostatic lenses in addition to focusing the electrons onto the entrance slit of the analyzer. For example if electrons with E_k from 100 eV to 150 eV are to be measured with a pass energy of 20 eV, then the retardation voltage will be scanned from 80 V to 130 V. For each step of the retardation voltage scan the electrons with the correct E_K is transmitted through the analyzer and counted by an electron detector

detector. Normally the detector is a Micro-Channel Plate (MCP).

3.2 Scanning Tunneling Microscopy

STM was developed in the early 1980s by Gerald Binnig and Heinrich Rohrer [50]. It is a powerful technique capable of imaging, probing and handling atoms with high precision. The STM is based on the principle of quantum mechanical tunneling of electrons between a sharp tip and the sample.

3.2.1 Basic experimental elements

In short, STM consists of taking a very sharp tip and positioning it very close to the sample, but not in contact, and then scanning it over the surface while recording the current of tunneling electrons between the tip and the sample, as illustrated in Fig. 3.8. The short distance between the tip and the sample will allow a small current of tunneling electrons, I_T, between the tip and the sample when a bias is applied. I_T is strongly dependent on the distance, d, between the tip and the sample, making it very sensitive to changes in the surface topography. If the tip is sharp enough, atomic resolution is achievable.

A STM image is created by making a raster scan of the surface area of interest while recording I_T and the tip movements in the z-direction. There are two modes of scanning, one where the feedback loop controls the z-movement of the tip in order to hold I_T and thereby d constant, this is called *constant current mode*. The other mode is the *constant height mode* where the z position is held constant and I_T is recorded. While scanning the tip is moved by piezoelectric elements, and the distance between tip and surface is controlled by a feedback loop.

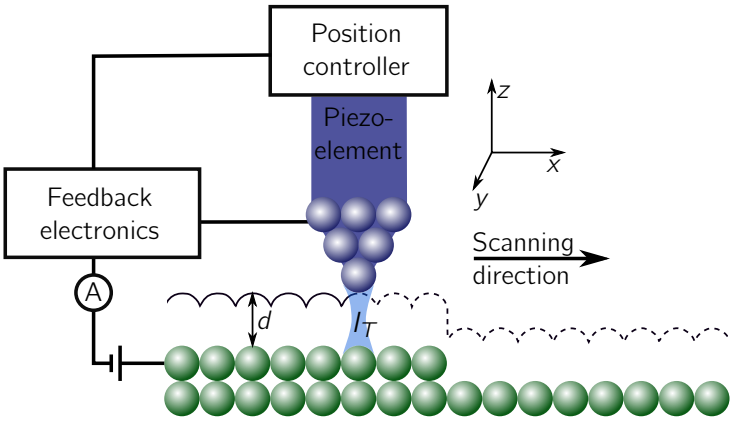

Figure 3.8. Schematic illustration of STM.

3.2.2 Theoretical considerations

Tunneling electrons is a concept which is predicted by the delocalized electron wave function in quantum theory. The transmission probability for a free electron to cross a finite square potential barrier, ϕ_{eff}, larger than the electron energy, ϵ, is given by

$$T(d,E) = \frac{16\epsilon\,(\phi_{eff}-\epsilon)}{\phi_{eff}^2} e^{-2\kappa d}, \qquad \text{where } \kappa = \sqrt{\frac{2m}{\hbar^2}\,(\phi_{eff}-\epsilon)}. \tag{3.12}$$

where m is the electron mass, d is the distance between tip and sample and $\hbar$ is the reduced Planck constant. This holds as long as $\kappa d \gg 1$ [37]. This gives the electrons a small finite probability to tunnel through the potential barrier.

The energy diagram of the tip-sample system is illustrated in Fig. 3.9. A potential barrier is created by the work functions of the sample, ϕ_S, and the tip, ϕ_T. During

operation a potential difference, eV, between the tip and the sample is applied, creating a net current from the tip to the sample, as in the illustrated case, with the tip at a negative potential relative to the sample. This way the empty states of the sample is probed. By reversing the bias the current will flow from the sample to the tip and thereby the occupied states of the sample will be probed. This means that the topography imaged by STM is a combination of both physical and electrical topography of both the sample and the tip.

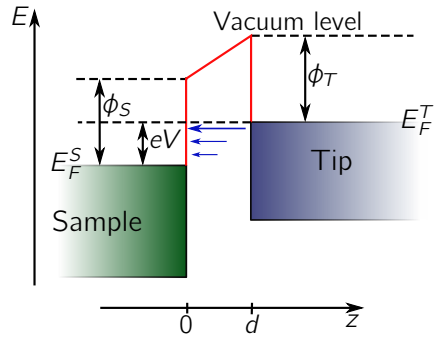

Figure 3.9. Energy diagram of the tunneling contact between the tip and the sample. The z-direction is normal to the surface, and d is the distance between tip and sample. $E_F^{S,T}$ and $\phi_{S,T}$ are the Fermi levels and work functions of the sample and tip, respectively. The tip is given a positve bias V relative to the sample. The potential barrier is indicated in red and the probability of tunneling electrons are indicated by blue arrows.

In order to judge the sensitivity of the STM a closer look at Eq. (3.12) is required. The inverse decay constant of 2κ gives the sensitivity of the tunneling probability for changes in d. Typical work functions of solids, typically in the range of 4-5 eV, gives $2\kappa \approx 20$ nm^{-1}, which means that a change of 0.1 nm in d results in a change of one order of magnitude

in T and thereby also the measured tunneling current. As a result the STM has a resolution in the z-direction down to a few picometers.

The resolution in the x, y-plane is not quite as good, as it strongly depends on the shape of the tip. Estimations based on a tip with a radius of 1 nm gives a resolution below 0.3 nm [51].

3.3 Low Energy Electron Diffraction

LEED is a technique used to determine the surface structure of a sample. It is based on the diffraction of electrons by the periodic lattice of the sample surface. This is achieved by sending electrons with energy typically in the range of 20 - 200 eV onto the sample. The electrons are then scattered by the atoms in the sample and some end up being reflected back from the sample. These electrons are recorded by a fluorescent screen, as illustrated in Fig. 3.10. Diffraction spots will appear if the atoms in the sample are arranged periodically, which will be explained in more detail below.

LEED is a technique which relies on both incoming and outgoing electrons, this means that the surface sensitivity is determined by the EMFP as discussed in Section 3.1.2. Thus, only atoms from the outermost layers of the sample are contributing to the recorded diffracted electrons.

3.3.1 Electron diffraction

The particle-wave duality of quantum mechanics says that electrons have both particle and wave properties [52]. This was first postulated by Louis de Broglie in 1923 [53]. He defined the wavelength of any elementary particle, the de

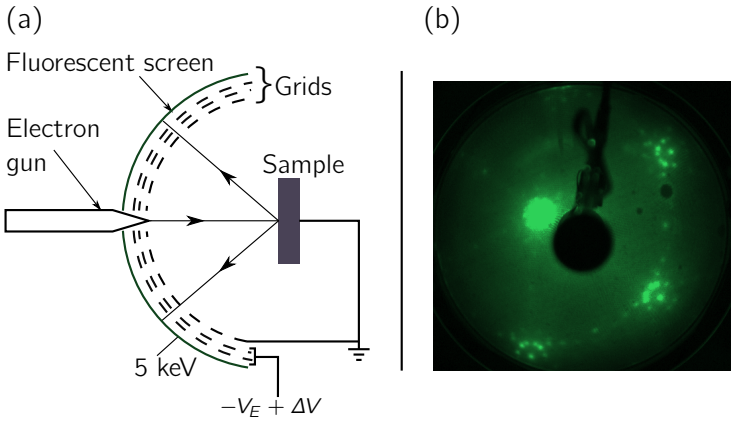

Figure 3.10. (a) Schematic illustration of a LEED setup.The electrons paths are indicated. (b) Image taken of the fluorescent screen. The sample is a Au crystal prepared with the herringbone surface reconstruction. The back of the electron gun can be seen in the center of the image. The big bright circle next to the electron gun is the centerspot of the LEED pattern.

Broglie wavelength, to be

$$\lambda = \frac{h}{p}, \tag{3.13}$$

where h is the Planck constant and p the particle momentum. The requirement for diffraction is that the incoming wavelength is of the order of or smaller than the lattice spacing. For LEED this means that the electron wavelength, λ_e has to be smaller than the interatomic spacing in the sample surface. The momentum $p = \sqrt{2mE}$, where E is the electron kinetic energy, gives $\lambda_e \approx 1 - 2$ Å for the electron energies applied in LEED. This is slightly less than the interatomic spacing in matter which is of the order of a few Å, and thereby the requirement for diffraction is fulfilled.

In order to relate the resulting diffraction spots to the sample it is necessary to visit the reciprocal space. A crystal structure which can be described by $\mathbf{R}_{pqr} = p\mathbf{a}_1 + q\mathbf{a}_2 + r\mathbf{a}_3$ will in the reciprocal space be described by $\mathbf{G}_{hkl} = h\mathbf{b}_1 + k\mathbf{b}_2 + l\mathbf{b}_3$ where $\mathbf{a}_i \cdot \mathbf{b}_j = 2\pi\delta_{i,j}$.

It is only elastically scattered electrons which are of interest. This means that both momentum and energy are conserved. An incoming electron is described by the wavevector $\mathbf{k}$ and the scattered electron is described by the wavevector $\mathbf{k'}$. Conservation of momentum and energy then gives

$$\mathbf{k} - \mathbf{k'} = \mathbf{G}_{hkl} \text{ and } |\mathbf{k}| = |\mathbf{k'}|, \tag{3.14}$$

respectively. This is the general case for scattering of a 3-dimensional (3D) object. In the case of LEED where it is mainly the 2-dimensional (2D) surface which contributes to the diffraction pattern the periodicity in the direction normal to the surface is broken. By separating the wavevectors into components normal,$\mathbf{k}_\perp$, and parallel, $\mathbf{k}_\parallel$ to the surface the momentum conservation in Eq. (3.14) can be written as

$$\mathbf{k}_\parallel - \mathbf{k'}_\parallel = \mathbf{G}_{hk}, \tag{3.15}$$

the broken symmetry results in diffraction rods perpendicular to the surface rather than diffraction spots.

In order to determine the resulting diffraction pattern it is very instructive to use the Ewald sphere developed by Paul Peter Ewald [54] to find the **k'** which gives constructive interference and thereby a spot the diffraction pattern. In Fig. 3.11 the Ewald sphere is used to illustrate where the spots will appear on the fluorescent screen of the LEED apparatus. The Evald sphere is defined by the **k** vector, with $|\mathbf{k}|$ being the radius of the sphere. **k** is chosen to point to a spot which is part of the reciprocal lattice pattern, the beginning of **k** is then the center of the Ewald sphere. For every lattice element, *i.e.* rods, which intersects with the Ewald sphere there will be a **k'** leading to a diffraction spot.

3.3.2 Experimental principles

An experimental setup for LEED is illustrated in Fig. 3.10. In the electron gun the electrons are accelerated by a potential of $-V_E$. The inner grid and the sample are grounded ensuring that there is no electrical potential in the region between the grid and the sample,comprising the traveling region of the incoming and backscattered electrons. The next two grids are set to $-V_E + \Delta V$. These grids will slow down the electrons and only those that have lost less energy than $e\Delta V$ during the scattering process at the sample are able to pass these two grids. The last grid, which is the fluorescent screen, is set to a high potential usually about 5 keV. This high voltage accelerates the electrons towards the fluorescent screen. Whenever an electron hits the fluorescent screen a bright spot will appear, resulting in an image as shown on the right side of Fig. 3.10. In this particular case the sample was an Au(111) crystal prepared with the herringbone surface reconstruction.

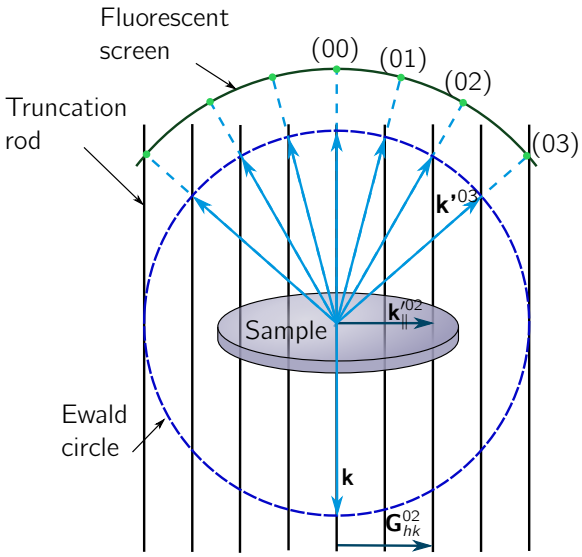

Figure 3.11. The broken symmetry at the surface results in truncation rods in the reciprocal space. The Ewald circle created by the incoming wavevector **k**, and the resulting **k'**. The bright spots on the Fluorescent screen correspond to diffraction spots observed by LEED.

If several structures coexist on the sample surface the respective LEED patterns will be superimposed. One example can be seen in Fig. 3.12 where the 1x1 of the Pd(100) is superimposed with the 3x5 and 4x5 structures of the TiO_x thin film overlayer. The symmetry of the Pd(100) surface allows two equivalent domains for each of the overlayer structures, which LEED patterns are also superimposed. When the unit cells of the individual patterns are identified, the absolute size of the overlayer unit cell can be determined by comparison to the known single crystal unit cell.

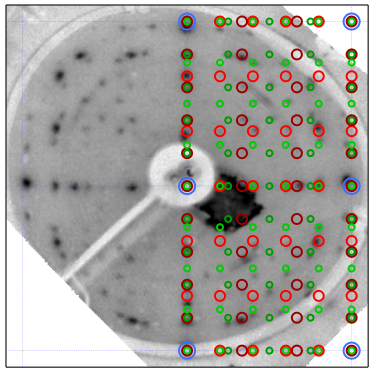

Figure 3.12. LEED image of a partially oxidized TiO_x thin film on Pd(100). The interpretation of the LEED pattern is displayed on the right half. The blue circles correspond to the 1x1 spots of Pd(100). The thin film is made up of structures with two different periodicities, 3x5 and 4x5, indicated by red and green circles, respectively. Due to substrate symmetries there are two different orientational domains for both overlayer structures indicated by lighter and darker shades of the respective color.

3.4 Sample preparation

The single crystal substrates are cleaned by standard ion-sputtering, annealing and oxygen treatment procedures prior to thin film deposition.

3.4.1 Thin film growth

The TiO_x thin films are grown by Chemical Vapor Deposition (CVD). CVD is a deposition method which relies on a chemical reaction occurring when the precursor comes in contact with the heated sample [22]. CVD is particularly suited for deposition of homogeneous thin films over large areas, irregular surfaces with trenches, tunnels or backsides may easily be covered. An example of this is TiO_2 grown by CVD on nanoporous-Au [55].

In this thesis Titanium (IV)isopropoxide (TTIP) was used as precursor in order to grow TiO_x thin films on Au(111), Pd(100) and Pd(111) by CVD. The chemical structure of TTIP is shown in Fig. 3.13. The Ti atom is in the center of the molecule and directly bound to four oxygen atoms.

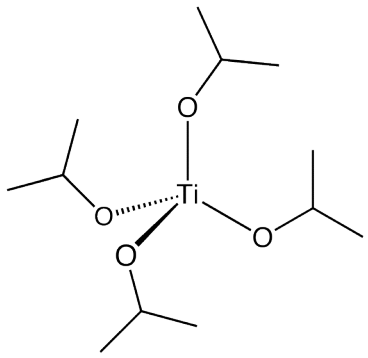

Figure 3.13. Chemical drawing of the TTIP molecule.

Full decomposition of TTIP is achieved for substrate temperatures above 300°C. TTIP generally decompose into TiO_2 and small organic molecules, however both substrate as well as temperature may influence the decomposition process [56, 57]. For small amounts and monolayers TiO_x with $x<2$ may be observed, whereas thicker films tend to primarily consist of fully oxidized TiO_2 [58–62].

4 Summary of papers

Growth of TiO_x have been studied at three different surfaces, Au(111) in paper **I** - **III**, Pd(100) in paper **V** and Pd(111) in paper **VI**. The TiO_x thin films on Pd(111) and Pd(100) was tested with respect to oxidation and reduction properties. In paper **IV** the thin films on Au(111) was studied in terms of their interaction with water.

4.1 TiO_x thin films

Both fully oxidized TiO_2 phases and partially oxidized phases consisting of TiO_x, x<2, have been characterized on all substrates. The partially oxidized phases are wetting layers of variable oxidation degree and structure, whereas the fully oxidized TiO_2 phases are thicker form both extended layers and islands.

4.1.1 TiOx phases on Au(111)

On Au(111) four different ordered TiO_x phases have been identified. Two of these phases, Honeycomb (HC) and Star, can be grown directly by CVD , whereas the other two, Pinwheel (PW) and TiO_2(B), are formed by annealing after deposition.

The HC phase is a Ti_2O_3 wetting layer forming a honeycomb pattern with a 2x2 periodicity relative to the Au(111) substrate. When this phase is annealed to 500°C the PW phase is formed. This phase consists of TiO_x, with $1 < x < 1.2$. The name of the phase is derived from the structure observed with STM which resembles pinwheels.

There are two phases on Au(111) which consist of fully oxidized TiO_2, the Star phase and the TiO_2(B) phase. The Star phase is formed directly by CVD deposition. This phase consists of islands randomly distributed over the Au(111) surface. The islands are likely to consist of rutile TiO_2(100) with a surface reconstruction consisting of rutile(110) microfacets, the exact structure is not conclusively determined. The TiO_2(B) phase consists of domains of TiO_2(B) (001) which are separated by clear boundary lines. There are six possible orientations of the domains. This phase is prepared by a TTIP deposition at low temperature, 280-300°C, resulting in a several layers of unordered TiO_2 covering the entire Au(111) surface. When this unordered TiO_2 is annealed at 500°C the TiO_2(B) phase is formed.

On Au(111) the as grown phases, HC and Star, grow simultaneously resulting in a mixed preparation consisting of both phases. The ratio between the two phases are tuned by the deposition temperature, the HC phase is dominating for preparations made at 300°C and the Star phase is dominating preparations made at 500°C. On Au(111) a deposition temperature of 300°C is necessary to obtain carbon free preparations.

4.1.2 TiO_x phases on Pd(100) and Pd(111)

Pd is a much more reactive material than Au and has a much higher sticking coefficient for small organic molecules. This means that the carbon containing species that are formed

during the decomposition of TTIP are likely to stick to Pd when the sample is cooled down after deposition. A post deposition flash to 500°C is therefore necessary after base pressure is reached in order to obtain a carbon free preparation.

TTIP mediated CVD growth of titania on Pd(100) and Pd(111) consists of three different growth stages; first a Pd-Ti alloy is formed, next a partially oxidized TiO_x wetting layer covers the surface, and last fully oxidized TiO_2 is formed on top of the wetting layer. Even though the general growth process are similar for the two surfaces the actual structures are somewhat different.

Oxidation of the partially oxidized wetting layer is possible and results in a different fully oxidized TiO_2 phase. This process also changes the interaction between the titania film and the Pd substrate. Is is possible to reversibly change back and forth between the partially oxidized phase and the oxidized version of this phase by oxidation and subsequent heating. This is a feature which is relevant for potential catalytic applications.

4.2 Water on TiO_x structures

The four TiO_x phases on Au(111) was investigated further in terms of their interaction with water. The results were also compared to rutile TiO_2(110). Three of the four phases was found to dissociate water. For the Star phase the amount of observed hydroxyls are comparable to that of rutile(110) and the dissociation mechanism appear to be related to the structure of the Star islands. On the TiO_2(B) phase less, but more strongly bound hydroxyls are observed, and the amount correlates well with the amount of boundary lines as judged by STM, the water dissociation on this phase is therefore believed to stem from defects along the

domain boundaries.

For the partially oxidized phases, HC and PW, only the PW phase appear to contribute to water dissociation. In this case the preparation itself is oxidized.

5 Future work

The TiO_x thin films grown on Au(111), Pd(111) and Pd(100) show that it is possible to make preparations with tailored properties in terms of oxidation/reduction sites or water dissociation possibilities combined with areas of exposed metal. These are properties that are beneficial for catalytic reactions which contain oxidation and/or reduction steps.

There are still some work remaining in order to fully characterize all of the phases observed on Pd(100) and Pd(111), in particular the fully oxidized TiO_2 phases. But also identification of active sites for water dissociation and the actual mechanism involved in dissociating water on the PW phase.

Future work for these systems may be to explore how they behave in atmospheres more relevant for catalysis and test to see if it is possible to get reactions such as CO oxidation, water gas shift or CO_2 hydrogenation to run with these systems as catalysts.

It would also be interesting to learn more about how these systems respond to UV light, both with respect to photocatalysis and hydrophilicity.

Bibliography

[1] A. Fujishima, K. Honda, *Nature* **238**, 37 (1972).

[2] R. Wang, K. Hashimoto, A. Fujishima, *Nature* **388**, 431 (1997).

[3] J. Mo, Y. Zhang, Q. Xu, J. J. Lamson, R. Zhao, *Atmos. Environ.* **43**, 2229 (2009).

[4] P. Maness, S. Smolinski, *Appl. Environ. Microbiol.* **65**, 4094 (1999).

[5] C. McCullagh, J. Robertson, *Res. Chem. Intermed.* **33**, 359 (2007).

[6] D. Blake, P. Maness, *Sep. Purif. Rev.* **28**, 1 (1999).

[7] I. X. I. Green, W. Tang, M. Neurock, J. T. J. Yates, J. T. Y. Jr, *Science* **333**, 736 (2011).

[8] M. A. Henderson, *Surf. Sci. Rep.* **66**, 185 (2011).

[9] J. Rodríguez, J. Hrbek, *Surf. Sci.* **604**, 241 (2010).

[10] M. Farnesi Camellone, D. Marx, *J. Phys. Chem. Lett.* **4**, 514 (2013).

[11] J. Oviedo, R. Sánchez-de Armas, M. A. San Miguel, J. F. Sanz, *J. Phys. Chem. C* **112**, 17737 (2008).

[12] L. Walle, A. Borg, P. Uvdal, A. Sandell, *Phys. Rev. B* **80**, 235436 (2009).

[13] K. Sebbari, C. Domain, J. Roques, H. Perron, E. Simoni, H. Catalette, *Surf. Sci.* **605**, 1275 (2011).

[14] D. A. Duncan, F. Allegretti, D. P. Woodruff, *Phys. Rev. B* **86**, 045411 (2012).

[15] M. Patel, G. Mallia, L. Liborio, N. M. Harrison, *Phys. Rev. B* **86**, 045302 (2012).

[16] M. Amft, L. E. L. Walle, D. Ragazzon, A. Borg, P. Uvdal, N. V. Skorodumova, A. Sandell, *J. Phys. Chem. C* **117**, 17078 (2013).

[17] C. L. Pang, R. Lindsay, G. Thornton, *Chem. Soc. Rev.* **37**, 2328 (2008).

[18] A. Atrei, A. M. Ferrari, D. Szieberth, B. Cortigiani, G. Rovida, *Phys. Chem. Chem. Phys.* **12**, 11587 (2010).

[19] A. Vittadini, F. Sedona, S. Agnoli, L. Artiglia, M. Casarin, G. A. Rizzi, M. Sambi, G. Granozzi, *Chemphyschem* **11**, 1550 (2010).

[20] R. Marchand, L. Brohan, M. Tournoux, *Mater. Res. Bull.* **15**, 1129 (1980).

[21] U. Diebold, *Surf. Sci. Rep.* **48**, 53 (2003).

[22] Y. Xu, X.-T. Yan, *Chemical Vapour Deposition*, Engineering Materials and Processes (Springer London, London, 2010).

[23] S. Hüfner, *Photoelectron Spectroscopy: Principles and Applications* (Springer, Berlin Heidelberg New York, 2003).

[24] H. Hertz, *Ann. der Phys. und Chemie* **267**, 983 (1887).

[25] A. Einstein, *Ann. Phys.* **17**, 132 (1905).

[26] T. Koopmans, *Physica* **1**, 104 (1934).

[27] P. Hemmer, *Kvantemekanikk* (Tapir akademisk forlag, 2005).

[28] R. Cole, P. Weightman, J. Matthew, *J. Electron Spectros. Relat. Phenomena* **133**, 47 (2003).

[29] B. Timmermans, F. Reniers, P. Weightman, N. Vaeck, *J. Electron Spectros. Relat. Phenomena* **159**, 1 (2007).

[30] P. Hohenberg, *Phys. Rev.* **136**, B864 (1964).

[31] W. Kohn, L. J. Sham, *Phys. Rev.* **140**, A1133 (1965).

[32] J. N. Andersen, C.-O. Almbladh, *J. Phys. Condens. Matter* **13**, 11267 (2001).

[33] R. M. Martin, *Electronic structure:Basic theory and practical Methods* (Cambridge University Press, 2008).

[34] B. Johansson, N. Må rtensson, *Phys. Rev. B* **21**, 4427 (1980).

[35] D. Penn, *Phys. Rev. B* **13**, 5248 (1976).

[36] A. Zangwill, *Physics at Surfaces* (Cambridge University Press, Cambridge, 1988).

[37] B. Bransden, C. Joachain, *Quantum Mechanics* (Pearson, 2000).

[38] B. E. A. Saleh, M. Teich, *Photonics* (Wiley, 1991).

[39] S. Doniach, M. Sunjic, *J. Phys. C Solid State Phys.* **3**, 285 (1970).

[40] D. Shirley, *Phys. Rev. B* **5**, 4709 (1972).

[41] A. Proctor, P. M. A. Sherwood, *Anal. Chem.* **54**, 13 (1982).

[42] S. Tougaard, *Surf. Interface Anal.* **11**, 453 (1988).

[43] S. Tougaard, C. Jansson, *Surf. Interface Anal.* **20**, 1013 (1993).

[44] J. Riviere, S. Myhra, eds., *Handbook of Surface and Interface Analysis: methods for problem solving* (Marcel Dekker, Inc., New York, 1998).

[45] M. Cardona, L. Ley, *Photoemission in solids I - general principles* (Springer, Berlin, Heidelberg, New York, 1978).

[46] HASYLAB, What is SR, how is it generated and what are its properties?, http://photon-science.desy.de/research/studentsteaching/primers/synchrotron_radiation/index_eng.html.

[47] Max IV laboratory - Max II, https://www.maxlab.lu.se/node/277.

[48] D. J. Griffiths, *Introduction to electrodynamics* (Prentice Hall, 1999), third edn.

[49] D. Attwood, Synchrotron Radiation for Materials Science Applications, http://ast.coe.berkeley.edu/srms/ (2007).

[50] G. Binnig, H. Rohrer, C. Gerber, E. Weibel, *Phys. Rev. Lett.* **49**, 57 (1982).

[51] G. Bracco, B. Holst, eds., *Surface Science Techniques* (Springer, Berlin Heidelberg, 2013).

[52] L. de Broglie, *Found. Phys.* **1**, 5 (1970).

[53] L. de Broglie, *Nature* p. 540 (1923).

[54] P. P. Ewald, *Acta Crystallogr. Sect. A Cryst. Physics, Diffraction, Theor. Gen. Crystallogr.* **25**, 103 (1969).

[55] A. Schaefer, D. Ragazzon, L. Walle, M. Farstad, A. Wichmann, M. Bäumer, A. Borg, A. Sandell, *Appl. Surf. Sci.* **282**, 439 (2013).

[56] C. P. Fictorie, *J. Vac. Sci. Technol. A Vacuum, Surfaces, Film.* **12**, 1108 (1994).

[57] P. Karlsson, J. Richter, M. Andersson, J. Blomquist, H. Siegbahn, P. Uvdal, A. Sandell, *Surf. Sci.* **580**, 207 (2005).

[58] D. Ragazzon, A. Schaefer, M. Farstad, L. Walle, P. Palmgren, A. Borg, P. Uvdal, A. Sandell, *Surf. Sci.* **617**, 211 (2013).

[59] D. Ragazzon, M. H. Farstad, A. Schaefer, L. E. Walle, P. Uvdal, P. Palmgren, A. Borg, A. Sandell, *In manuscript* (2014).

[60] D. Ragazzon, M. H. Farstad, A. Schaefer, L. E. Walle, P. Uvdal, A. Borg, A. Sandell, *Submitted to Surf. Sci.* (2014).

[61] M. H. Farstad, D. Ragazzon, Grönbeck, M. D. Strømsheim, A. Borg, A. Sandell, *In manuscript* (2014).

[62] M. H. Farstad, D. Ragazzon, M. D. Strømsheim, A. Borg, A. Sandell, *In manuscript* (2014).

Part II

Papers

Paper I

Chemical vapor deposition of ordered TiO_x nanostructures on Au(111)

D. Ragazzon, A. Schaefer, M.H. Farstad, L.E. Walle, P. Palmgren,
A. Borg, P. Uvdal, A. Sandell

Surface Science, **617** (2013) 211-217

Surface Science 617 (2013) 211–217

Contents lists available at ScienceDirect

Surface Science

journal homepage: www.elsevier.com/locate/susc

Chemical vapor deposition of ordered TiO_x nanostructures on Au(111)

D. Ragazzon [a], A. Schaefer [b], M.H. Farstad [c], L.E. Walle [c], P. Palmgren [d], A. Borg [c], P. Uvdal [e,f], A. Sandell [a,*]

[a] Dept. of Physics and Astronomy, Uppsala University, P. O. Box 516, SE-75120 Uppsala, Sweden
[b] Institute of Applied and Physical Chemistry, University of Bremen, Box 33 04 40, D-28359 Bremen, Germany
[c] Dept. of Physics, Norwegian University of Science and Technology (NTNU), NO-7491 Trondheim, Norway
[d] VG Scienta, Uppsala, SE-752 28, Sweden
[e] Chemical Physics, Dept. of Chemistry, Lund University, P.O. Box 124, SE-221 00 Lund, Sweden
[f] MAX-IV Laboratory, Lund University, P.O. Box 118, SE-221 00 Lund, Sweden

ARTICLE INFO

Article history:
Received 3 June 2013
Accepted 19 July 2013
Available online 25 July 2013

Keywords:
Titanium dioxide
Gold
Chemical vapor deposition
Synchrotron radiation photoelectron spectroscopy
Low-energy electron diffraction
Scanning tunneling microscopy

ABSTRACT

The deposition of TiO_x ($x \leq 2$) structures on Au(111) by chemical vapor deposition (CVD) in ultrahigh vacuum (UHV) has been investigated with high-resolution core level photoelectron spectroscopy (PES), low-energy electron diffraction (LEED) and scanning tunneling microscopy (STM). Using titanium tetra-isopropoxide as single source precursor it is possible to form different TiO_x phases on the surface after deposition: at low coverages, we observe large two-dimensional (2D) honeycomb-lattice Ti_2O_3 islands with a (2×2) registry with the substrate. Higher coverages are dominated by the formation of three-dimensional (3D) TiO_2 structures. The TiO_2 structures are atomically well ordered provided that the deposition temperature is high enough (500 °C). The ordered structure exhibits a LEED pattern characteristic for a rectangular surface unit cell. By performing the deposition at different temperatures it is possible to tune the balance between the 2D and 3D phases: Growth at 500 °C significantly favors the formation of 3D TiO_2 islands as compared to growth at 200 °C and 300 °C.
© 2013 Elsevier B.V. All rights reserved.

1. Introduction

Catalytic reactions promoted by Au nanoparticles deposited on the surface of a variety of different TiO_2 structures and surfaces have been explored extensively during the last decade [1–5]. The oxidation of CO on small, TiO_2 supported gold particles has been found to take place at remarkably low temperatures, down to 200 K [6]. Compelling evidence for a cooperative effect within the Au–TiO_2 system was put forward in a recent publication by the Yates group, in which they specifically point out Ti–Au dual sites at the particle perimeter as responsible for the catalytic activity [7]. The "inverse system", TiO_2/Au(111), was also found to promote the water-gas shift reaction (WGS) ($H_2O + CO \rightarrow H_2 + CO_2$) [8]. Neither bulk gold nor titania is able to catalyze the WGS, while TiO_2 particles covering 20–30% of the Au surface showed an activity comparable to the one of Cu(110), a reference WGS catalyst.

The important properties of the TiO_2–Au boundary region have triggered several fundamental studies, aimed at controlling the synthesis and growth of titania particles on gold. In the majority of these, physical vapor deposition (PVD) of Ti metal and oxidation in O_2 atmosphere was used to produce titania structures on Au(111) [9–11]. Titania islands with hexagonal, triangular or needle-like shape were observed. Deposition and oxidation of defined-size Ti clusters were also employed [12], producing clusters with hexagonal facets after annealing. Recently, Wu et al. conducted a thorough study of the development of ordered TiO_x structures on Au(111). The titania films were grown by post-oxidation of Ti at 600 °C [9]. For increasing Ti doses, they could obtain a wetting film with honeycomb (HC) structure, a pinwheel-like phase and eventually triangular islands. The oxidation of a Ti–Au alloy allowed for the production of rather well-defined TiO_2 crystallites exhibiting a line structure on the surface [13]. In an alternative approach denoted reactive layer deposition (RLAD), Ti was deposited on a layer of H_2O or N_2O and subsequent heating generated TiO_x structures [14,15]. Several coexisting structures were observed on the surface: hexagonal rutile-TiO_2 islands, octagonal lepidocrocite crystallites, ridge-like formations and a porous structure. The porous structure produced by RLAD bears a remarkable resemblance with the HC phase reported by Wu et al., although that paper claims that the pores had random diameters [11].

The previous studies thus reveal a complex behavior of the TiO_x/Au(111) system: two or more different structures often coexist on the surface and the preparation procedure influences significantly the structure and morphology of the TiO_x film [9–16]. A common trait among most of these works, however, is the finding of hexagonal titania islands. The latter were suggested to have the rutile structure, since the topmost layer exhibited a periodicity and step height compatible with rutile-TiO_2(100) [11,12].

A method that has not been used so far to grow TiO_x on Au(111) is chemical vapor deposition (CVD). In CVD a gaseous precursor reacts on a substrate, depositing a solid material. The deposition reaction is usually

* Corresponding author. Tel.: +46 18 4713606; fax: +46 18 4713524.
E-mail address: anders.sandell@physics.uu.se (A. Sandell).

0039-6028/$ – see front matter © 2013 Elsevier B.V. All rights reserved.
http://dx.doi.org/10.1016/j.susc.2013.07.019

thermally activated, although other means to induce the precursor reaction exist. This technique offers the potential of coating finely structured and porous substrates by virtue of the effective penetration of the precursor molecules [17,18]. With respect to the TiO_x/Au system a particularly intriguing prospect is to use CVD to coat nanoporous gold, a nanostructured form of gold that exhibits considerable catalytic activity [19–22].

In the current work, we present results on the growth of titania nanostructures on Au(111) by decomposition of titanium tetraisopropoxide (TTIP), $Ti(OC_3H_7)_4$, a commonly used metal–organic precursor for CVD of TiO_2. Two atomically ordered phases are found and characterized by high-resolution core level photoelectron spectroscopy (PES), low-energy electron diffraction (LEED) and scanning tunneling microscopy (STM). This is followed by an extensive growth study exploiting PES and LEED fingerprints of the phases. The growth series reveal that the balance between the phases changes with the deposition temperature. The study thus gives the first insight into the structural and morphological control attainable when using CVD for growth of ultrathin TiO_x films on Au(111).

2. Materials and methods

The experiments were conducted in ultra-high vacuum (UHV). The base pressure was always in the low 10^{-10} mbar range. The UHV chambers were equipped with LEED, ion gun and offered the possibility of heating the sample. PES measurements were carried out using synchrotron radiation at beamline I311 at the MAXII ring of the MAX IV Laboratory, Sweden [23]. The PES data presented in this paper were acquired in normal emission. Ti 2p spectra were measured using a photon energy of 590 eV, O 1 s spectra at a photon energy of 650 eV and Au 4f spectra at 220 eV. The kinetic energies of the photoelectrons were thus comparable, ranging from about 120 eV for O 1 s photoelectrons to about 135 eV for Au 4f photoelectrons. That is, their inelastic mean free paths (IMFPs) are also similar when travelling through the same material. PES was also used to check possible contamination originating from the decomposition of the precursor. No carbon impurities were observed upon growth at 300 °C and 500 °C, in accordance with previous growth experiments using TTIP [24], while they were noted upon growth at 200 °C. The binding energy (BE) scale of each spectrum was measured with respect to the Fermi level.

STM experiments were conducted at room temperature in the home laboratories at Uppsala University and at the Norwegian University of Science and Technology (NTNU) in Trondheim. In both cases an Omicron Variable-Temperature STM system and tungsten tips were used. A Au(111) crystal (Surface Preparation Laboratory) was used as a substrate. The clean Au(111) surface was prepared by means of sputtering and annealing (sputtering with Ar^+ ions at 1 keV for 20 min; annealing at 530 °C for 20 min; lowering the temperature from 530 °C to 430 °C in 5 min; annealing at 430 °C for 10 min), modifying slightly the procedure described by Biener et al. [16]. Sputtering and annealing cycles were repeated until only Au was detected by PES and the LEED showed a well-defined pattern of the herringbone (HB) reconstruction, which is characteristic of clean Au(111). The observation of large terraces presenting the HB reconstruction was also used to confirm that the surface was clean when STM was available. TTIP (Sigma–Aldrich, purity 99.999%) was stored in a glass tube connected to the vacuum chamber through a leak-valve. TTIP was dosed onto the sample in UHV using a stainless-steel tube positioned a few centimeters from the sample. The TTIP purification was carried out by freeze–pump–thaw cycles and the gas line was baked in order to remove water. For this purpose a sorption pump was also used. The TTIP pressures applied during deposition were between $1 \cdot 10^{-9}$ mbar and $5 \cdot 10^{-8}$ mbar.

3. Results and discussion

The influence of the substrate temperature and of the TTIP dose on the titania film structure grown by CVD was investigated by dosing increasing amounts of TTIP on the substrate at different temperatures. Two ordered titania structures could be found on the sample after deposition, depending on the deposition conditions. The titania films can be modified by post-deposition treatment and more structures can be produced. The latter will be described in a different paper, while the current work is focused on the as-deposited phases. We start with a presentation of the geometric structures of these phases on the basis of LEED and STM data in sec. 3.1. In the subsequent sections, PES results are used to characterize the chemical state of the two phases (sec. 3.2) and to analyze the morphological evolution of the film when performing CVD at different temperatures (sec. 3.3).

Growth series were conducted at three different substrate temperatures: the lowest temperature (200 °C) is close to the minimum temperature at which the TTIP precursor decomposes. At the next temperature (300 °C) decomposition is more facile but the growth is still expected to be reaction-limited [25]. At the highest temperature chosen (500 °C), the decomposition reaction is very fast making the growth flux-limited [25]. The formation of ordered structures during the growth was monitored with LEED. The focus is put on sub-monolayer coverages and ultrathin films (typically between 2 Å and 20 Å) partly covering the Au(111) surface; that is, situations where the synergy effects of the catalyst system are likely to be of importance.

3.1. Geometric structure of the ordered TiO_x phases

The first ordered structure obtained by CVD is the HC Ti_2O_3 phase. It is observed at low coverages at all three deposition temperatures. This structure has recently been observed upon Ti deposition at submonolayer coverage followed by post-oxidation at 600 °C [9]. According to the suggested model, Ti atoms sit directly on the gold surface, occupying alternatively a hexagonal close packed (HCP) or cubic close packed site (CCP) and the second nearest CCP or HCP sites, as depicted in Fig. 1A. This arrangement results in a layer of Ti atoms that form a structure of interconnected hexagons resembling an HC. The sides of the hexagons are aligned along the Au(111) <112> directions and measure 3.34 Å. Oxygen atoms are located in the middle of each side of the hexagons, presumably slightly above the Ti atoms. The unit cell of the HC structure has a (2×2) relationship with the one of the Au(111) surface.

STM images of the HC phase produced by CVD are shown in Fig. 2. At positive bias empty states are imaged. Since these are localized mostly on the Ti atoms (of formal charge 3+) the bright features observable in Fig. 2B give the location of the Ti atoms. This imaging contrast is analogous to what has been reported for the rutile-TiO_2(110) surface [26]. Images of larger sample areas (Fig. 2A) show that the HC phase forms large islands on the sample, reaching sizes of the order of 50 nm. The Au(111) HB reconstruction changes its orientation next to the HC islands, so that the soliton walls follow the perimeter of the latter. The apparent height of the HC islands was observed to change depending on the imaging conditions, consistent with the description provided by Wu et al. [9]. Simultaneous observation of a (2×2) LEED pattern (Fig. 1B) gives solid support for the proposed atomic structure model. The (2×2) superstructure spots were usually very sharp, confirming that the HC phase forms large ordered islands.

The second ordered titania structure is referred to as the Star phase, based on the LEED pattern shown in Fig. 3 A. The pattern is comprised of three equivalent patterns rotated by 120°. The rectangular unit cell generating this pattern measures 23.8 ± 2.3 Å $\times$ 5.0 ± 0.2 Å.

Fig. 3B shows the LEED pattern generated by a phase with the lattice constants obtained as the average of these and of the one obtained by STM (see later in the text), showing that there is a very good agreement with the experimental LEED pattern.

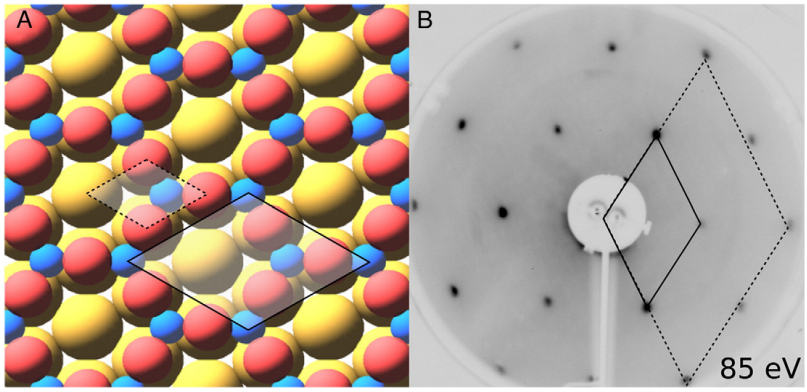

Fig. 1. HC-Ti_2O_3 on Au(111). (A) Model of the HC phase as suggested by Wu et al. [9]. Ti atoms are shown in blue, O atoms in red and Au atoms in gold color. (B) The unit cell of Au(111) and the (2 × 2) unit cell of the HC are indicated with a dashed and a solid line, respectively.

STM images (Fig. 4A) of a surface exhibiting the Star LEED pattern show titania islands surrounded by clean Au(111) areas (manifested by the HB reconstruction). Their sides are preferentially oriented along the < 110 > directions and form angles of about 120°. We will refer to these islands as "hexagonal" islands, although their actual shape can be more irregular due to the merging of several islands or because of different lengths of the sides. On the island surface several parallel lines can be distinguished. High-resolution pictures (Fig. 4B) show atomic-sized features on these lines. Although they do not provide enough information to conclusively identify the atomic structure of the Star phase, they show that two kinds of lines are alternating on the surface: One kind presents a zigzag motive, while the other is broader and appears slightly lower. A rectangular unit cell of 25.5 ± 2 Å × 4.8 ± 0.2 Å was measured, in good agreement with the dimensions derived from the LEED pattern. The average unit cell determined from LEED and STM (24.5 ± 1.5 Å × 4.9 ± 0.14 Å) (containing two lines) is rather close to the line distance of 11 Å measured on the surface of the particles produced by oxidation of a Ti–Au alloy [13,14].

Following the common interpretation in literature, these islands are suggested to have the same rutile structure and exhibit the (100) surface, as was suggested for previously reported hexagonal TiO_2 islands on Au(111) [11,13]. Occasionally one or more steps are present on the Star islands. Their measured height is 2.1 ± 0.2 Å, compatible with the distance of 2.292 Å between titanium layers in rutile-TiO_2(100) [26]. The surface reconstruction of rutile that would give the closest agreement with the measured unit cell would be an (8 × 1) reconstruction of rutile-TiO_2(100)[001]//Au(111)[110], whose unit cell would measure 4.6 Å × 23.6 Å. However, such a reconstruction has to our knowledge not been observed on the surface of rutile-TiO_2(100) single crystals. We also considered the possibility that the islands are related to the (2 × 1) and (4 × 1) reconstructions of rutile (011) [27], since they appear similar to the zigzag and the broad lines respectively in the STM images. The interpretation that the hexagonal titania islands observed on Au(111) are rutile-TiO_2(100) seems to be the most plausible because the lattice constants of the rutile (011) reconstruction are different (slightly outside the error bars) from the ones obtained in the experiments. We finally note a remarkable resemblance between the Star reconstruction and a quasi-(2 × 1) rutile-TiO_2 phase observed on Pt(111), of which the exact structure is not known yet [28].

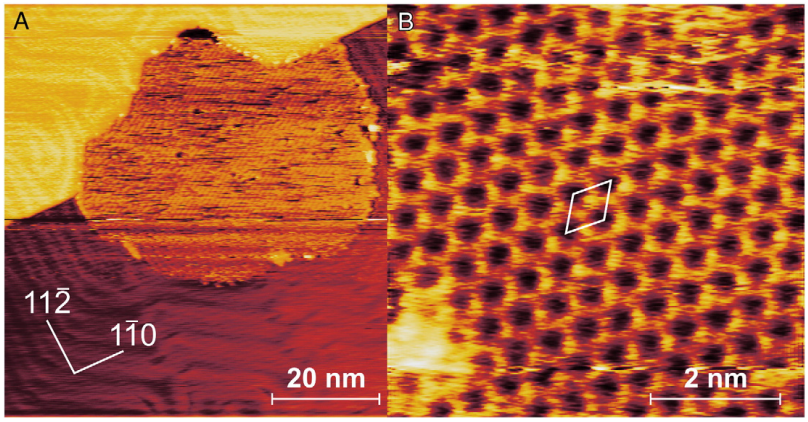

Fig. 2. STM images of the HC phase. (A) STM image of a HC island. The domains of the herringbone reconstruction rearrange to follow the sides of the island. Imaged using V = 0.5 V and I = 0.43 nA. (B) High-resolution image of the HC phase. The hexagonal honeycomb structure is evident in this image and bright protrusions are also observed at the vertices of the hexagons. The unit cell (5.7 Å × 5.7 Å) is evidenced. Imaged using V = 0.70 V and I = 0.23 nA. A mild Fourier transform filtering has been applied to minimize the noise in the picture.

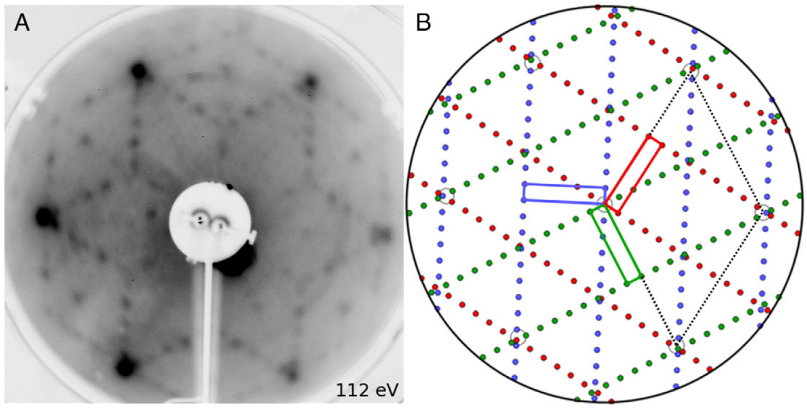

Fig. 3. LEED pattern of the Star-TiO_2 on Au(111). (A) Experimental LEED pattern. (B) Drawing illustrating the observed pattern in terms of three domains (red, green and blue) of a rectangular titania phase with the average lattice constants determined by LEED and STM. The position of the spots of the Au(111) surface is also indicated (black empty circles). The unit cells of each lattice are also shown.

3.2. Chemical states of the TiO_x structures

Fig. 5A shows Ti $2p_{3/2}$ PES spectra for selected preparations where titania overlayers were grown by TTIP CVD at 200 °C, 300 °C and 500 °C. The Ti $2p_{3/2}$ spectra were fitted using three components (see Supplementary Material for details). In order of decreasing BE, the first state (blue curve, labeled "1") is found at 459.0 eV, in good agreement with the reported position for stoichiometric TiO_2 [24,26]. The second state (green curve, labeled "2") appears at 457.7 eV and a third state (red curve, labeled "3") is located at 456.5 eV. States 2 and 3 both fall within the BE range reported for Ti^{3+}, 455.6–458.1 eV [29] and can therefore be associated with reduced or substoichiometric titania. Peak 1, associated with TiO_2, progressively gains relative intensity compared to the other two components as the coverage increases, until becoming largely predominant. Upon growth at 500 °C the LEED pattern evolves into the Star pattern, which supports that the Star is an ordered, stoichiometric TiO_2 phase. At 200 °C and 300 °C the Star pattern is not observed, showing that oxidized TiO_2 with no evidence of translational order grows at lower temperature. Peak 2 is attributed to defects within the TiO_2 structure [30] since its intensity stays constant relative to peak 1. It can be excluded that peak 2 stems only from interfacial Ti^{3+} species because it was detected even when the TiO_2 islands were thicker than the IMFP of the photoelectrons, that is, when the contribution by species at the interface was negligible. Consequently, the spectra for the thick TiO_2 islands contain a significant contribution from defects and/or sub-stoichiometric parts, e.g. steps and edges.

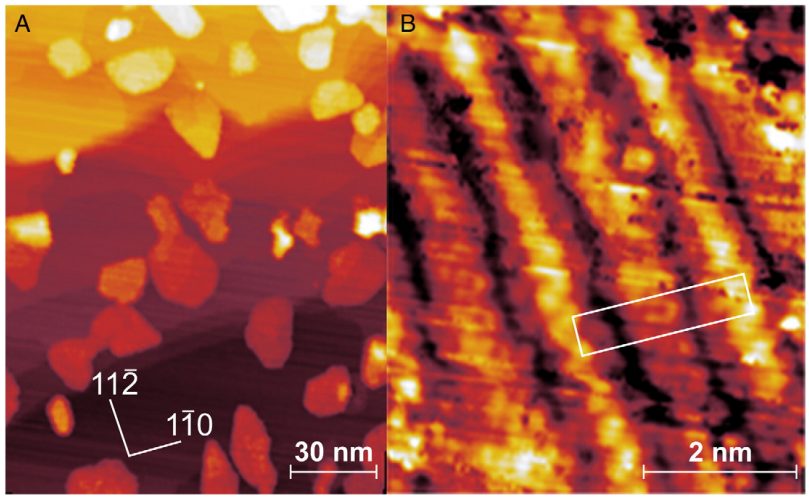

Fig. 4. STM images of the Star phase. (A) STM image of titania crystallites on Au(111). This surface exhibits the Star LEED pattern. The sides of the islands present preferential orientations along the Au <110> directions. Most of the islands appear as irregular hexagons or triangles or as a coalescence of these two shapes. Imaged using V = 0.75 V and i = 1.0 nA. (B) High-resolution image of the Star crystallites, showing hints of the atomic structure. The surface structure appears as alternating bright zigzag lines and broader lines with a shorter apparent height.

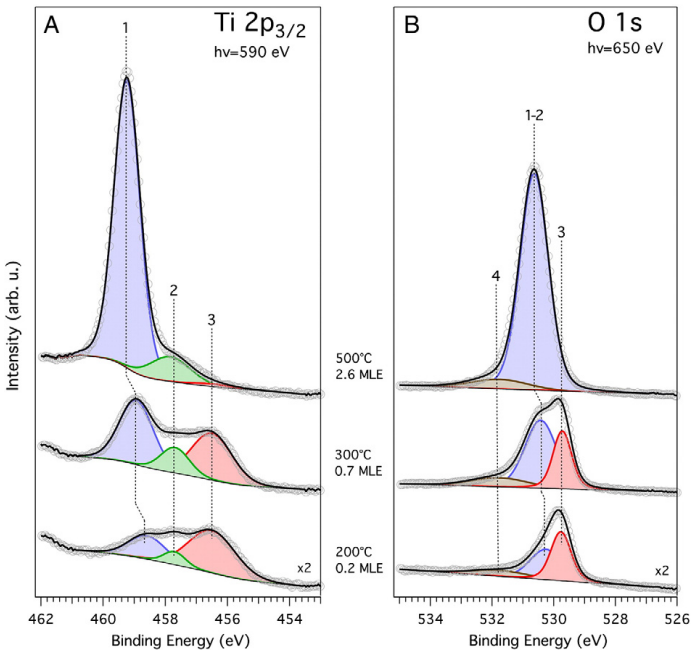

Fig. 5. PES spectra of Ti $2p_{3/2}$ and O 1 s core levels of TiOx/Au(111). (A) The Ti $2p_{3/2}$ spectra were deconvoluted into three components. "1" and "2" are related to TiO_2 islands, "3" to the HC phase. (B) The O 1 s spectra were deconvoluted into three components, which showed a correlation with the contributions in the Ti $2p_{3/2}$ spectra. "1-2" is associated with TiO_2 islands and "3" is the signature of the HC phase. The broad feature labeled "4" was needed to reproduce the shape of the O1 s spectrum but its origin is not clear.

Peak 3 represents the spectroscopic signature of the HC phase because it is prevalent in the PES spectrum in the low coverage regime when the (2×2) LEED pattern is brightest. The BE of Ti $2p_{3/2}$ state 3 is similar to that found for reduced (Ti_2O_3) films grown on metallic substrates [31]. This is in agreement with the stoichiometry suggested for the HC. However, it should be kept in mind that the BE can be influenced by initial state effects (band bending) as well as final state effects (screening) due to the interaction with the Au(111) substrate.

Fig. 5B shows the corresponding O 1 s spectra. The spectra were fitted using three components. The blue curve in Fig. 5B represents a state with a BE of 530.5 eV, which is a typical value for the O 1 s peak in TiO_2. Accordingly, an analysis of the peak intensities using the Pearson's correlation coefficient yields that this O 1 s peak is strongly linearly correlated (above 90%) with both Ti $2p_{3/2}$ peak 1 and Ti $2p_{3/2}$ peak 2, the peaks of TiO_2. To emphasize this correlation to the Ti species, this O 1 s component is labeled "1-2". The O 1 s component marked by a red curve in Fig. 5 represents another oxygen species, with an O 1 s BE of 529.6 eV. This state is labeled "3" because it exhibits a rather strong correlation (55%) with Ti $2p_{3/2}$ peak 3, i.e. the HC phase. It is interesting to note that the O 1 s peak of the HC phase has a lower BE than that of TiO_2, although both have a formal charge of 2-. This could be due to band banding or screening, but it could also be an effect of the oxygen coordination: the O atoms of the HC phase are two-fold coordinated while the O atoms of (bulk) TiO_2 are three-fold coordinated. Previous calculations showed that the BE of O 1 s in magnesium oxide decreases with decreasing oxygen coordination number [32]. In the case of PdO/Pd(100) oxygen atoms with higher coordination to the metal presented also a higher O 1 s BE [33,34]. Finally, a broad component, shown in green (labeled "4"), is needed to satisfactorily reproduce the O 1 s spectra. This peak is probably related to the TiO_2 phase. A similar feature has indeed been noted before for TiO_2 but its exact origin is unknown [14–16].

3.3. Temperature dependence of the film morphology

The intensity ratios between the Au 4f surface component of each preparation and the one of clean Au(111) were used as an estimate of uncovered gold area remaining on the sample after each TiO_x deposition. The Au 4f spectra were fitted with the Au $4f_{7/2}$ surface component at a BE of 83.7 eV and the bulk component at a BE of 84.0 eV. The intensities of the PES signals of TiO_2, the HC (Ti_2O_3) phase and the bulk component of the Au 4f signal were used to determine the area of the surface covered by TiO_2 and HC, respectively, as well as the height of the TiO_2 islands. The calculation assumed exponential attenuation of the photoemission signal with film thickness. The HC phase was assumed to have constant height in all the preparations and the TiO_2 crystals were assumed to be rutile. This analysis provided also a measurement of the total Ti dose present on the sample. A more detailed description of the procedure is given in the supplementary material.

Fig. 6 summarizes the results of the morphological analysis of the growth series. The graphs show the fractional occupation of the sample surface by the different phases, as a function of the number of Ti atoms per unit area. This is expressed in monolayer-equivalent (MLE), corresponding to 0.14 $Å^{-2}$, a value equal to the atomic density of the Au(111) surface. This definition means that at a coverage of 1 MLE the deposited material contains one Ti atom per Au atom on the Au(111) surface. In Fig. 6, the contribution from TiO_2 is added to that from the HC phase, so that the relative height of the three parts corresponds to the relative areas of HC, TiO_2 and free Au(111).

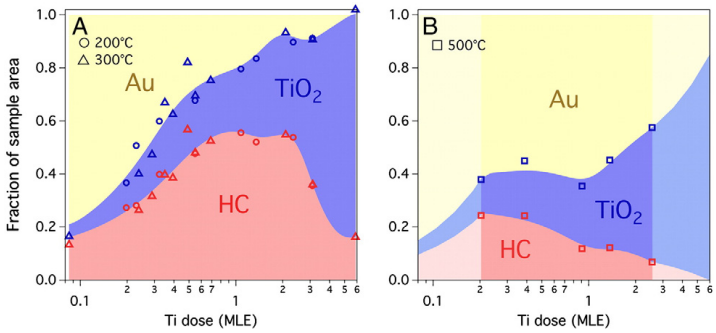

Fig. 6. The surface areas covered by the HC phase (red) and by TiO_2 islands (blue) shown as a function of the amount of Ti deposited on the sample. The relative heights of the red, blue and yellow parts represent the relative amounts of HC, TiO_2 and free Au(111) surface, respectively. (A) Growth at 200 °C (circles) and 300 °C (triangles). (B) Growth at 500 °C (squares). The lighter areas on the sides of graph B indicate the behavior outside the data range. The smooth, colored areas are guides for the eye.

Fig. 6A shows the growth series performed at 200 °C (circles) and 300 °C (triangles). These results are presented together to emphasize that the growth behavior is essentially identical at these deposition temperatures, although a higher degree of order (narrower PES peaks and sharper LEED patterns) and an absence of carbon contaminants were observed when the deposition was performed at 300 °C. At low coverages the HC phase clearly dominates over the TiO_2 phase. At about 0.8 MLE, the amount of HC does not increase further, while the formation of the TiO_2 phase proceeds. At this critical coverage, about 75% of the Au(111) surface is covered: 50% by the HC phase and 25% by the TiO_2 phase. In terms of atomic fraction, about half of the Ti belongs to the HC phase and half to the TiO_2 phase. Above 2 MLE, the signal of the HC phase decreases rapidly with increasing coverage.

The same qualitative behavior is found at 500 °C, as shown with squares in Fig. 6B: both phases form from the start and above a critical coverage the fraction of HC decreases while the TiO_2 phase grows. As mentioned before, at this deposition temperature the TiO_2 phase is ordered, giving rise to the Star LEED pattern. Considering the partitioning into TiO_2 and HC phase, the formation of TiO_2 is favored at 500 °C in comparison to the low-temperature series. The maximum area covered by the HC phase at 500 °C is only about 25%, i.e. half the maximum area formed at 200 °C and 300 °C. The signal from the HC phase disappears at lower coverages compared to the lower-temperature series: a substantial decrease in the amount of HC is noticed already at about 1 MLE.

The observed temperature dependence of the growth can be rationalized in simple thermodynamic terms. At sufficiently high temperatures, the kinetic barriers are overcome and the most stable products are formed. This suggests that the Star phase is the thermodynamically stable titania phase on Au(111). From this follows that the HC phase must be metastable. However, the kinetic barriers preventing conversion of the HC phase into the Star phase are sufficient to allow its formation at low coverages even at 500 °C. Several details indicate that the metastability of the HC phase is related to the interaction with the substrate. The first one is the tendency of the HC phase to wet large substrate areas, meaning that the interaction with the underlying gold is more prominent than in the case of the Star. Secondly, the (2×2) relation between the lattice constant of the HC and the Au(111) indicates that the HC is strongly influenced by the substrate. Finally, the orientation of the domains of the HB reconstruction changes around the perimeter of the islands, hinting that the HB is destroyed underneath the HC phase. This means that the energy gained by the titania–gold interface formation is at least equal to the energy gained by forming the HB reconstruction. Lifting the HB reconstruction causes the release of Au atoms, since the reconstructed layer has a 4.5% higher atomic density than the unreconstructed one. These atoms are most likely pushed aside as the Ti_2O_3 islands grow, since no evidence of the presence of Au atoms within or on the HC islands could be found.

In general, nucleation and subsequent growth can be influenced by the presence of special sites on the surfaces (step edges, domain boundaries, other defects, etc.). However, for the TiO_x/Au(111) system such effects do not appear to be significant according to the STM images. Both the Star and HC phases grow at step edges, but with no clear preference for either phase. The domain boundaries of the surface reconstruction are also reactive points, and in the case of Au(111) the elbows of the HB reconstruction are particularly reactive. Their high reactivity promotes the nucleation of metallic Ti, but this preferential location is not preserved upon oxidation [16]. Accordingly, we find no preferential nucleation of either phase at the elbow sites but it is clear that further studies are required in order to fully understand the nucleation process.

Finally, a comparison with the structures obtained by other growth techniques is not straightforward. The results above underline the importance of kinetics in the growth and stabilization of TiO_x films on Au(111). Changing the preparation method therefore has a strong impact on the resulting film morphology. This explains also why several growth products have been reported in literature. The CVD growth performed at 500 °C is expected to resemble the reactive PVD of Ti in O atmosphere. In both cases the growth is governed by the diffusion and interaction of Ti_mO_n clusters on the surface, generated by a fast TTIP decomposition in the case of CVD and by interaction between Ti and O_2 in the gas phase in case of reactive PVD. However, to our knowledge growth of TiO_2 on Au(111) by reactive PVD has not been reported yet. Amongst the PVD experiments present in the literature, the one that is closest to reactive deposition is the deposition of metallic Ti on Au(111) followed by room-temperature oxidation and subsequent annealing. In that case, metallic Ti was shown to have a very low mobility compared to TiO_2 and therefore the active species leading to the formation of TiO_2 islands were Ti_mO_n clusters, formed upon oxidation. Hexagonal and triangular islands were found [10,16], similar to the CVD growth at 500 °C. Furthermore, the TiO_2 islands grown by oxidation of a Ti–Au alloy [13] have most likely the same atomic structure as the islands grown by CVD in the present work. Finally, a comparison with the RLAD approach is even harder. It can be nevertheless pointed out that hexagonal rutile clusters with line spacing compatible with the one of the Star are also observed among the

RLAD products. The presence on Au(111) of TiO_2 islands with the same structure, independent of the growth technique used (i.e. of the kinetic barriers), corroborates the statement that this is the most stable titania phase on Au(111).

4. Conclusions

The CVD of titania nanostructures on Au(111) using titanium tetraisopropoxide as precursor has been investigated. Two ordered phases were found and characterized by means of LEED, STM and PES. The first phase is a wetting Ti_2O_3 layer with a HC structure in a 2×2 relationship to the Au substrate. The second phase, denoted the Star phase based on the LEED pattern, consists of three-dimensional (3D) islands of TiO_2, presenting a rectangular surface unit cell compatible with a rutile TiO_2(100) (8×1) surface reconstruction. The HC phase forms at low coverages. It is interface-stabilized with a thickness limited to only one layer. At higher coverages the growth of 3D TiO_2 structures dominates. The TiO_2 structures become well ordered, exhibiting the Star LEED pattern, only if the deposition temperature is high enough to overcome the kinetic barriers. This is the most stable structure of TiO_2/Au(111). Growth at different temperatures reveals that it is possible to tune the balance between the two-dimensional HC phase and the 3D TiO_2 phase. Such a prospect is highly relevant for studies of surface reactions where TiO_2–Au synergy effects and a well defined surface composition are of importance.

Acknowledgements

We thank the staff at MAX-lab for their support. Financial support was received from the Swedish Energy Agency (STEM), the Trygger foundation, the Crafoord foundation, NordForsk and the Göran Gustafsson foundation. L.E.W. has been supported through the Strategic Area Materials at NTNU and D.R. has been supported by the Anna Maria Lundins scholarship from Smålands Nation in Uppsala.

Appendix A. Supplementary data

Supplementary data to this article can be found online at http://dx.doi.org/10.1016/j.susc.2013.07.019.

References

[1] M. Haruta, Catal. Today 36 (1997) 153.
[2] R. Meyer, C. Lemire, S.K. Shaikhutdinov, H. Freund, Gold Bull. 37 (2004) 72.
[3] A.S.K. Hashmi, G.J. Hutchings, Angew. Chem. Int. Ed. 45 (2006) 7896.
[4] A. Corma, H. Garcia, Chem. Soc. Rev. 37 (2008) 2096.
[5] M. Valden, X. Lai, D.W. Goodman, Science 281 (1998) 1647.
[6] H. Huber, D. McIntosh, G.A. Ozin, Inorg. Chem. 16 (1977) 975.
[7] I.X. Green, W. Tang, M. Neurock, J.T. Yates, Science 333 (2011) 736.
[8] J.A. Rodriguez, S. Ma, P. Liu, J. Hrbek, J. Evans, M. Pérez, Science 318 (2007) 1757.
[9] C. Wu, M.S.J. Marshall, M.R. Castell, J. Phys. Chem. C 115 (2011) 8643.
[10] E. Farfan-Arribas, J. Biener, C.M. Friend, R.J. Madix, Surf. Sci. 591 (2005) 1.
[11] D.V. Potapenko, R.M. Osgood, Nano Lett. 9 (2009) 2378.
[12] K. Lauwaet, K. Schouteden, E. Janssens, C. Van Haesendonck, P. Lievens, Phys. Rev. B 83 (2011) 155433.
[13] D.V. Potapenko, Z. Li, Y. Lou, Y. Guo, R.M. Osgood, J. Catal. 297 (2013) 281.
[14] D.V. Potapenko, J. Hrbek, R.M. Osgood, ACS Nano 2 (2008) 1353.
[15] Z. Song, J. Hrbek, R. Osgood, Nano Lett. 5 (2005) 1327.
[16] J. Biener, E. Farfan-Arribas, M. Biener, C.M. Friend, R.J. Madix, J. Chem. Phys. 123 (2005) 94705.
[17] M. Ritala, M. Leskelä, L. Niinistö, P. Haussalo, Chem. Mater. 5 (1993) 1174.
[18] M. Ritala, K. Kukli, A. Rahte, P.I. Räisänen, M. Leskelä, T. Sajavaara, J. Keinonen, Science 288 (2000) 319.
[19] A. Wittstock, J. Biener, M. Bäumer, Phys. Chem. Chem. Phys. 12 (2010) 12919.
[20] M.M. Biener, J. Biener, A. Wichmann, A. Wittstock, T.F. Baumann, M. Bäumer, A.V. Hamza, Nano Lett. 11 (2011) 3085.
[21] In: A. Wittstock, J. Biener, J. Erlebacher, M. Bäumer (Eds.), Nanoporous Gold, Royal Society of Chemistry, Cambridge, 2012.
[22] A. Schaefer, D. Ragazzon, L.E. Walle, M.H. Farstad, A. Wichmann, M. Bäumer, A. Borg, A. Sandell, Appl. Surf. Sci. 282 (2013) 439.
[23] R. Nyholm, J.N. Andersen, U. Johansson, B.N. Jensen, I. Lindau, Nucl. Instrum. Methods A 467–468 (2001) 520.
[24] P.G. Karlsson, J.H. Richter, M.P. Andersson, M.K.-J. Johansson, J. Blomquist, P. Uvdal, A. Sandell, Surf. Sci. 605 (2011) 1147.
[25] C.J. Taylor, D.C. Gilmer, D.G. Colombo, G.D. Wilk, S.A. Campbell, J. Roberts, W.L. Gladfelter, J. Am. Chem. Soc. 121 (1999) 5220.
[26] U. Diebold, Surf. Sci. Rep. 48 (2003) 53.
[27] T. Kubo, H. Orita, H. Nozoye, J. Am. Chem. Soc. 129 (2007) 10474.
[28] E. Cavaliere, L. Artiglia, G.A. Rizzi, L. Gavioli, G. Granozzi, Surf. Sci. 608 (2013) 173.
[29] F. Sedona, G.A. Rizzi, S. Agnoli, F.X. Llabrés i Xamena, K. Schierbaum, G. Granozzi, J. Phys. Chem. B 109 (2005) 24411.
[30] Y. Mizuno, F.K. King, Y. Yamauchi, T. Homma, A. Tanaka, Y. Takakuwa, T. Momose, J. Vac. Sci. Technol. A 20 (2002) 1716.
[31] T. Matsumoto, M. Batzill, S. Hsieh, B.E. Koel, Surf. Sci. 572 (2004) 127.
[32] E.P. Mikheeva, S.F. Ruzankin, G.M. Zhidomirov, Z. Struktumoi, J. Struct. Chem. 36 (1995) 13.
[33] L.E. Walle, H. Grönbeck, V.R. Fernandes, S. Blomberg, M.H. Farstad, K. Schulte, J. Gustafson, J.N. Andersen, E. Lundgren, A. Borg, Surf. Sci. 606 (2012) 1777.
[34] M. Todorova, E. Lundgren, V. Blum, A. Mikkelsen, S. Gray, J. Gustafson, M. Borg, J. Rogal, K. Reuter, J.N. Andersen, M. Scheffler, Surf. Sci. 541 (2003) 101.

Paper II

Growth of TiO_2(B)(001) on Au(111) by Chemical Vapor Deposition

D. Ragazzon, A. Schaefer, M.H. Farstad, L.E. Walle, P. Uvdal, A. Borg, A. Sandell

Accepted by Surface Science
DOI: 10.1016/j.susc.2014.10.011

Growth of TiO_2(B)(001) on Au(111) by Chemical Vapor Deposition

D. Ragazzon[1], M. H. Farstad[2], A. Schaefer[3], L. E. Walle[2], P. Uvdal[4,5], A. Borg[2] and A. Sandell[1,*]

[1] *Dept. of Physics and Astronomy, Uppsala University, P. O. Box 516, SE-75120 Uppsala, Sweden*
[2] *Dept. of Physics, Norwegian University of Science and Technology (NTNU), NO-7491 Trondheim, Norway*
[3] *Institute of Applied and Physical Chemistry, University of Bremen, Box 33 04 40, D-28359 Bremen, Germany*
[4] *Chemical Physics, Dept. of Chemistry, P.O. Box 124*
[5] *MAX-IV Laboratory, P.O. Box 118, Lund University, SE-221 00 Lund, Sweden*

It is presented how a TiO_2(B) film exposing the (001) face can be grown on Au(111) by chemical vapor deposition. Identification and characterization of the TiO_2(B)(001) layer is carried out with low-energy electron diffraction (LEED), synchrotron radiation photoelectron spectroscopy (PES), scanning tunneling microscopy (STM) and x-ray absorption spectroscopy (XAS). Formation of the TiO_2(B) film requires a two-step preparation procedure: deposition at 280°C followed by annealing to 500°C. This suggests that the interaction between substrate and overlayer stabilizes the TiO_2(B) film, preventing the formation of thermodynamically more stable rutile islands. The study thus gives insight into how the morphology and the atomic structure of the titania overlayer can be controlled.

1. Introduction

TiO_2(B) is considered as the fourth natural titania polymorph, next to the rutile, anatase, and brookite phases. The first successful synthesis of TiO_2(B) was achieved in 1980 by Marchand et al.. The structure of TiO_2(B) presents continuous channels and lower density than the other natural titania polymorphs. The open structure of TiO_2(B) makes it attractive for energy storage applications, particularly as electrode material for rechargeable Li ion batteries[1–3]. With such applications as the main driving force, different TiO_2(B) nanostructural morphologies as nanoparticles[4], nanowires[5–7], nanoribbons[8] and nanotubes[9] have been synthesized with chemical methods. Another important question is whether TiO_2(B) possess a higher photocatalytic activity than anatase and rutile. Yamamoto et al. have addressed the photocatlaytic properties of TiO_2(B) prepared using a hydrothermal method[10]. However, the preparation of metastable TiO_2 phases is difficult and lack of control over cleanliness, phase purity and morphology has so far prevented a direct comparison with the activities of the rutile and anatase phases.

A different route to produce unusual titania polymorphs is offered by thin film deposition in ultrahigh vacuum (UHV). Such an approach offers optimal purity and by the use of single crystal substrates, geometrical order can be imposed and imaged with scanning probe techniques. Unusual forms of titania, such as lepidocrocite sheets and TiO_2(B), have been observed upon deposition of ultrathin films by Ti evaporation in an O_2 atmosphere (reactive Physical Vapor Deposition, PVD). The most clear-cut example of TiO_2(B) formation is the growth of TiO_2(B)(001) reported to occur on Pt(111) and Pt(110) surfaces[11]. The identification of TiO_2(B)(001) was made on the basis of LEED, PES, STM[12] and XAS[13] measurements supported by theoretical simulations of the STM images[11].

In the present work, we demonstrate that TiO_2(B)(001) can be produced on the surface of Au(111) by way of metal-organic chemical vapor deposition (CVD) in a UHV chamber. Au(111) makes for an interesting comparison to Pt(111) as it also is an hexagonal surface but a more inert one, which may impact the film morphology. With respect to potential applications, the Au-TiO_2 combination has attracted considerable attention as a viable catalyst. Since several studies indicate that the catalytic activity can be ascribed to a cooperative effect occurring at Au-TiO_2 boundaries it follows that Au/TiO_2 as well as TiO_2/Au are potentially active as catalysts. For example, the oxidation of CO on small, TiO_2 supported gold particles has been found to take place at temperatures down to 200 K while TiO_2/Au(111) shows a high performance for the water-gas shift (WGS) reaction ($H_2O+CO \rightarrow H_2+CO_2$). Moreover, gold in nanostructured, unsupported form has shown a remarkable surface reactivity, for instance towards CO oxidation[14]. In a recent work[15], we were able to enhance the CO oxidation activity by decoration of the gold ligaments by titania. To achieve efficient loading of the gold pores we employed CVD with titanium(IV) isopropoxide (TTIP) as precursor.

Recently, we have also demonstrated that TTIP mediated CVD can be utilized to form ordered TiO_x ultrathin films on Au(111)[16]. A wetting single layer of Ti_2O_3 with honeycomb (HC) structure develops from the very lowest coverages. This structure is metastable and it is stabilized by the interaction with the substrate. At the same time stoichiometric TiO_2 clusters are also formed. These become predominant when higher amounts of Ti are present on the sample. The investigation of the growth process at different temperatures showed that the TiO_2 clusters have the highest thermodynamic stability, as cluster formation becomes predominant when the

deposition is performed at high temperatures. If deposition is performed at 500°C, the clusters exhibit an ordered surface with a periodicity of about 24.5 Å × 4.9 Å. This structure was interpreted as a surface reconstructed rutile-TiO_2(100) and denoted as the Star phase on the basis of the LEED pattern.

In this paper, we present low energy electron diffraction (LEED) patterns, scanning tunneling microscopy (STM) images, x-ray absorption (XAS) spectra and photoemission (PES) spectra to explore TiO_2(B)(001) formed on the Au(111) surface. The underlying idea for the formation of TiO_2(B) on Au(111) is to exploit substrate-overlayer interactions to create metastable structures. In order to do so, the deposition was performed at low temperature (about 300 °C). This has two effects[16]: a) the formation of the stable TiO_2 clusters is limited, and b) the overlayer wets better the surface, that is, a higher fraction of the titania film can interact with the substrate. Once a large part of the overlayer is interacting with the gold, the sample is annealed and extended layers of fully oxidized TiO_2(B)(001) are formed, presumably as a result of kinetic constraints that hinder the formation of separate TiO_2 clusters.

2. Methods

The experiments were conducted in different ultrahigh vacuum (UHV) chambers. The STM measurements were done at the Norwegian University of Science and Technology (NTNU) in Trondheim, Norway. This chamber also allowed for low energy electron diffraction (LEED) and photoelectron spectroscopy characterization. In this chamber, PES data were obtained using non-monochromatized Al Kα radiation and a SPECS electron energy analyzer. The PES spectra were used to relate the situations to those attained at the synchrotron.

The high-resolution photoelectron spectroscopy (PES) measurements were conducted at the MAX II ring of the MAX IV Laboratory, Sweden, using beamlines D1011[17] and I311[18]. Photon energies of 590 eV, 650 eV and 130 eV were used to acquire Ti 2p, O 1s and valence band spectra, respectively. In addition, overview spectra were acquired at 1487 eV in order to relate the results to the samples investigated by STM. The PES spectra presented in this work were acquired in normal emission and the binding energy (BE) scales referenced to the Fermi level of the Au(111) substrate. Total yield x-ray absorption (XAS) measurements were conducted at beamline D1011, using linearly polarized light with the polarization vector parallel to the surface. The photon energy was calibrated by the change in kinetic energy of a specific photoemission peak measured using first and second order radiation.

The clean Au(111) surface was prepared by several cycles of sputtering and annealing, following the recipe in reference[16]. The sample was deemed clean when LEED showed the pattern of the herringbone reconstruction and surface sensitive PES measurements showed the absence of contaminants.

Titanium(IV) isopropoxide (TTIP, Sigma–Aldrich, purity 99.999%) was dosed onto the sample in UHV using a doser, positioned a few centimeters from the sample. A leak-valve was used to control the TTIP pressure in the chamber during the deposition. The typical pressures used during exposure were between $1 \cdot 10^{-9}$ mbar and $5 \cdot 10^{-8}$ mbar. The TTIP was initially purified by several freeze–pump–thaw cycles; for this purpose a sorption pump was used in addition. The gas line was baked to remove water.

3. Results

3.1. Atomic structure of TiO_2(B)(001)

The identification of the TiO_2(B) phase relies on previous structural characterization. TiO_2(B) is conventionally presented using a non-primitive monoclinic unit cell. The experimental lattice parameters[19] are a=12.20 Å, b=3.75 Å, c=6.54 Å and β=107.16°. The atoms are arranged as shown in Figure 1. The stable termination of the TiO_2(B)(001) surface exhibits two inequivalent 5-fold coordinated Ti atoms, two inequivalent 3-fold coordinated O atoms and one 2-fold coordinated O atom. It was described in detail elsewhere (denoted as type-I)[20], and it can be obtained by terminating the crystal with a (002) plane, i.e. a horizontal plane passing through the center of the unit cell shown in Figure 1. This surface can be described either by using a rectangular centered lattice with constants a and b, or by a primitive oblique unit cell with an angle γ=107.1° and sides b_1=b=3.75 Å and b_2=6.38 Å.

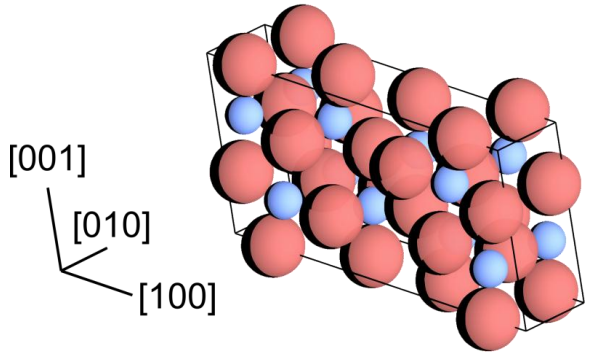

Figure 1. Conventional unit cell of the TiO_2(B). O atoms are shown in red and Ti in blue.

3.2. Formation of the TiO_2(B)(001) layer on Au(111)

Whether TiO_2(B) will form or not is critically dependent on the preparation route, in terms of both coverage and substrate temperature. The TiO_2(B) layer is formed in a two-step procedure: deposition of TTIP at low temperature (280-300 °C) followed by subsequent annealing to 500-550 °C. Initial deposition down to 200 °C is also likely to lead to TiO_2(B) formation upon annealing but at such low temperatures decomposition and desorption of the TTIP ligands is limited, resulting in a film with carbon contamination.

The formation of TiO_2(B) on Au(111) also requires that a critical minimum coverage of TiO_2 is deposited prior to annealing to 500 °C. In the present work, the coverage is expressed in monolayer-equivalent (MLE), defined as 1 MLE = 0.138 $Å^{-2}$. This value refers to the surface atomic density of Au(111), that is, a layer containing one Ti atom per Au atom on the surface corresponds to a coverage of 1 MLE. We would like to stress that the MLE unit does not contain any information on the morphology of the film. For instance, a double layer of Ti atoms, where each layer has 0.138 Ti per $Å^2$, but covering only half of the sample, also contains 1 MLE of Ti. The lowest Ti dose at which the formation of TiO_2(B) was observed, was about 1.4 ± 0.4 MLE as judged by XPS, at which the film covered about 75% of the substrate according to STM. The TiO_2(B) films of the highest quality are obtained with a Ti dose of about 2-3 MLE at which basically the whole sample surface is covered (95%).

The thinnest films tend to present more defects in their electronic structure (as judged by PES), while the thickest ones tend to exhibit less sharp LEED patterns, assumedly because there are bigger variation of the film height over the sample, making the surface more rough.

3.3. Geometric structure of TiO_2(B)(001) on Au(111)

The initial step in the preparation of the TiO_2(B) phase on Au(111) is, as previously mentioned, growth of a layer by TTIP deposition at about 300°C that covers the Au(111) surface. This film shows no LEED spots, that is, it is disordered. The diffraction spots of the substrate, if they are present at all, appear weak and blurry. The next step is heating of the disordered film to 500°C. This procedure leads to the emergence of new, well-defined LEED spots. The LEED image obtained after the annealing is shown in Figure 2(a). This pattern results from the presence of six equivalent domain of a structure with an oblique surface unit cell, with constants b_1= 3.8 ± 0.3 Å , b_2= 6.1 ± 0.5 Å , and an angle γ= 108° ± 4° between them. The domains of the overlayer are oriented with the longer side of the unit cell rotated by 2° relative to the <11,$\bar{}$0> directions of the Au(111) surface. The measured unit cell is in good agreement with the surface unit cell of the TiO_2(B)(001) surface (γ=107.1° and sides b_1=3.75 Å and b_2=6.38 Å). Figure 2(b) shows a TiO_2(B)(001) layer on Au(111) with orientation as measured by LEED. The unit cells of the substrate and overlayer have been highlighted.

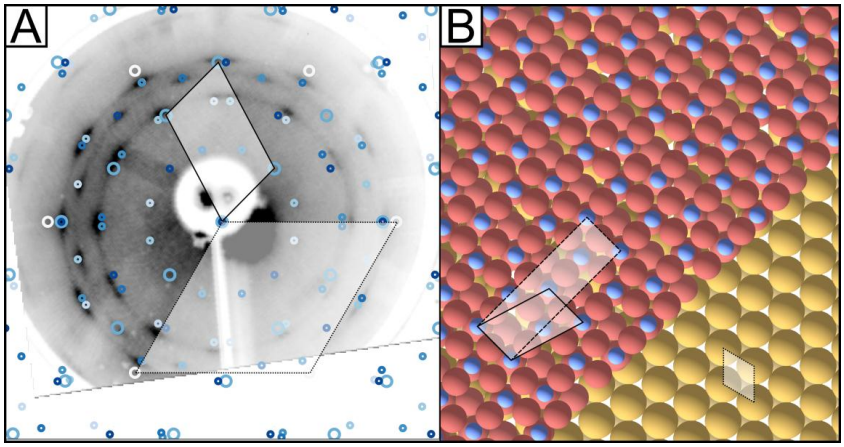

Figure 2. (a) LEED pattern of the TiO_2(B). White circles mark the position of the substrate spots. The substrate hexagonal unit cell is shown with a dotted line. The diffraction patterns of the domains of TiO_2(B) is shown by circles with different shades of blue. The oblique unit cell of one domain is shown with a solid line. The lower intensity of the pattern on the right-hand side is due to experimental conditions (lens settings and angle) and it is not inherent to the diffraction pattern. (b) One domain of TiO_2(B)(001) on Au(111) oriented as suggested by LEED data. Blue and red spheres represent Ti and O atoms, respectively. The picture shows the stable "Type-I termination" of the TiO_2(B). The surface can equivalently be described by using a centered rectangular unit cell (dashed line) or by using a primitive unit cell (solid line). The substrate unit cell is also shown with a dotted line. The translational position was arbitrarily chosen.

STM images of the annealed, ordered titania films associated with the LEED pattern are presented in Figure 3. Figure 3(a) displays a large-scale image of the sample. Parts of the surface (about 25%) appear smooth and have been attributed to clean, unreconstructed Au(111) areas. A grey-scale color map has been used to highlight these areas. The remaining part of the sample is covered by several domains of TiO_2(B) (001) with different orientations. The borders between the islands appear as the brightest lines in the image. The titania film displays a uniform apparent height, as no significant height differences are detected between neighboring domains. The film is measured at a height of 4.2 ± 0.3 Å relative to the lowest Au terrace. The Ti coverage for this preparation was estimated to be 1.4 ± 0.4 MLE.

A TiO_2(B) film containing 1.4 ± 0.4 MLE of Ti atoms and covering 75% of the sample would have a thickness of 9.3 Å (as the density of TiO_2(B) is 0.028 $Å^{-3}$, or 0.202 MLE/Å), which is significantly different from the apparent height measured by STM. Thus, we must therefore assume that differences in the electronic structures between the titania film and the gold substrate contribute significantly to the observed height value; relevant dependence of the film apparent height on electronic effects was already observed on TiOx films on Au(111)[21]. The surface of the islands presents two different periodicities: a long one and one at the atomic scale. The long periodicity is defined by a pattern of brighter and darker lines, separated by 20-25 Å. These lines can be a Moiré effect due to the underlying substrate and/or a corrugation of the surface. The shorter periodicity is presented in Figure 3(b), which displays the image of the surface of an island after the slowly varying components have been filtered, as illustrated in Figure 3(c-f). The filtering highlights the periodic structure at the atomic scale, which is comprised of a regular arrangement of bright round spots, bridged by areas with medium intensity. In between there are slightly larger dark areas. The (oblique) unit cell of this structure measures b_1= 4.11 Å , b_2= 5.45 Å , and the two sides form an angle γ= 101.6°. These values differ from the ones measured by LEED by up to 12% and the angle is different by about 6°. For reliable structure determination, measurements, LEED is the method of choice; STM constants can differ from the actual ones because of the drift of the tip while scanning, while in LEED the substrate spots provide an internal standard for the calibration of the image. On the left-hand side of Figure 3 (b), the structure of the Type-I termination of TiO_2(B)(001) was drawn onto the uncorrected STM image; the TiO_2(B) unit cell was linearly transformed to adapt to the image. In the case of other TiO_2 surfaces[22], it was shown that Ti atoms appear as the brightest feature. Assuming the same behavior for the TiO_2(B) (001), the Ti atoms in Figure 3 (b) have been aligned with the bright features. This alignment establishes a biunivocal correspondence also between O atoms and areas with medium intensity, as well as between dark areas and positions where no atoms are expected on the topmost layer of the TiO_2(B)(001). The oblique (solid line) and the center rectangular (dashed line) unit cells have been drawn onto the STM image and on the TiO_2(B)(001) structure in Figure 3(b).

X-ray absorption spectroscopy (XAS) was used to further characterize the titania films and to confirm their TiO_2(B) nature. Previous studies have used XAS spectra of the Ti L-edge in a fingerprinting fashion to identify the TiO_2 polymorph[23,24]. Figure 4 presents the XAS spectrum of the TiO_2(B) film on Au(111) at the Ti L-edge along with the spectra of other titania polymorphs.

The adsorption peaks have been labeled according to previous work[25]. The adsorption spectrum is comprised of two main sets of peaks caused by spin-orbit and multiplet splitting, corresponding to absorption processes at the L_3 ($2p_{3/2}$) and L_2 ($2p_{1/2}$) edges, respectively. Additional fine structure is commonly assigned to crystal-

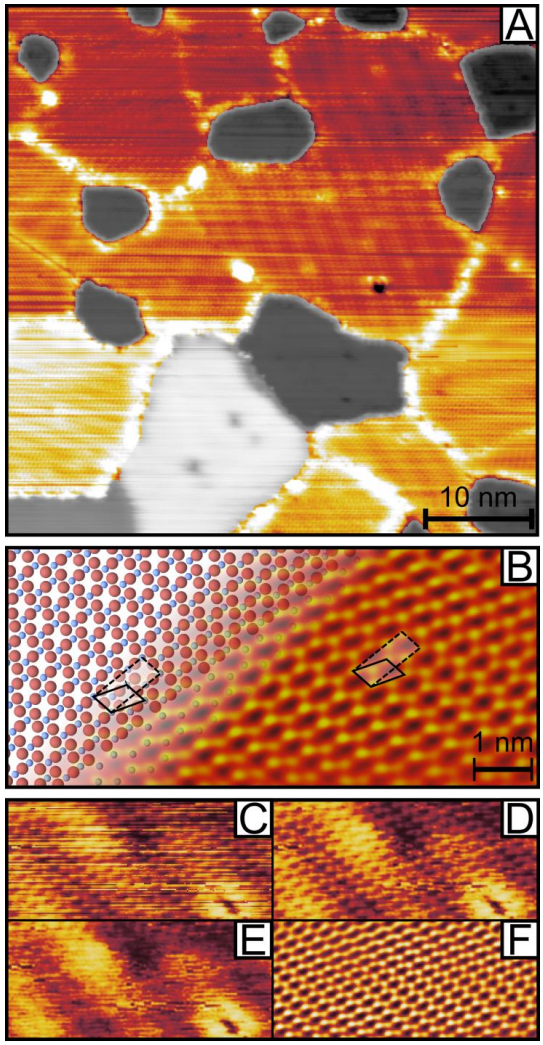

Figure 3. STM of TiO_2(B)/Au(111). (a) Overview image of the sample after TTIP-CVD at 280 °C and subsequent annealing to 500 °C. A grey color scale is used for the substrate and a red-yellow one to emphasize the TiO_2(B) film. (b) TiO_2(B) atomic structure compared to STM images of the TiO_2(B). Fourier-transform filtering was applied to highlight the atomic-scale periodicity. The primitive (solid line) and the center rectangular (dashed line) unit cells are shown. The processing of the STM image leading to the atomic-scale periodicity shown in (b) is illustrated in (c-f): (c) raw image; (d) is the result of the removal of the noise in the form of stripes. Fourier transform analysis was used to decompose this image into (e) its slowly varying components and (f) the atomic-scale features used in (b).

field splitting. The two states labeled A_3 originate from L_3 and L_2 transitions to orbitals with t_{2g} symmetry. Transitions to e_g orbitals generate the B_1 and B_2 contributions (and B, which is composed of their spin-orbit split unresolved counterparts). The relative intensity of these two peaks is changed between different TiO_2 polymorphs. The B_1 component is stronger than B_2 in the case of anatase, weaker for rutile and intermediate for TiO_2(B). The absorption spectrum of the TiO_2(B) reference sample presents remarkable similarities with the one of the TiO_2 film grown on Au(111) described in the present work, corroborating the hypothesis that the film has TiO_2(B) structure.

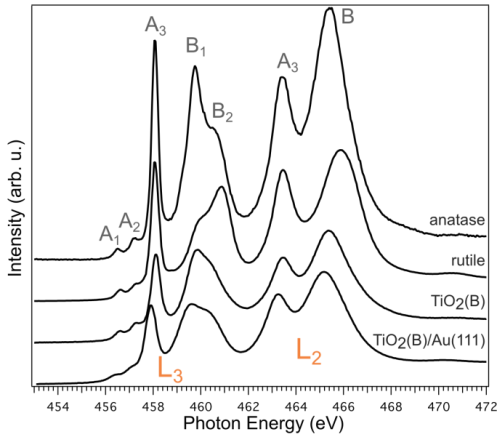

Figure 4. The XAS spectrum of TiO_2(B)(001) grown by CVD on Au(111) is compared to the ones rutile and anatase, as well as to a reference spectrum obtain from TiO_2(B) powder. The XAS spectrum, and particularly the intensity ratio between peaks B_1 and B_2, is used as a fingerprint to identify the structure of the TiO_2 film on Au(111). Peaks labeled according to reference 25.

3.4. Electronic structure of TiO_2(B)-(001) on Au(111)

The PES spectra of the Ti $2p_{3/2}$ and O 1s core levels for different sample preparations are shown in Figure 5 (a) and (b), respectively. The corresponding valence band spectra are presented in (c), where the valence band of the Au(111) substrate is also included. Starting with the core levels, the two situations at the bottom refer to TiO_x and TiO_2 films on Au(111) that we have previously discussed in detail[16]. The first situation is the honeycomb-Ti_2O_3 (HC) structure. It exhibits a (2x2) LEED pattern and is the main structure after TTIP CVD deposition at low temperature. This phase is observed at coverages below the critical one required to obtain the TiO_2(B) layer upon subsequent annealing. The next situation is the so-called Star phase, a phase with TiO_2 stoichiometry. If the sample is kept at 500°C during the CVD deposition, this becomes the dominant ordered phase for amounts of Ti on the sample comparable to the ones used in the present study. The third set of spectra was measured on the amorphous TiO_2 precursor layer, that is, the situation that upon annealing transforms into TiO_2(B). The deposition was carried out at 290 °C and the amount of Ti on the sample was 3.3 ± 0.3 MLE. The topmost PES spectra were measured after heating this amorphous layer to 540°C. The sample showed the LEED pattern of TiO_2(B)-(001) described in the previous section.

The features of the Ti $2p_{3/2}$ spectra were assigned to three different components, following a procedure similar to the one described in reference[16]. Component "1" is associated with stoichiometric TiO_2, "2" with defects (i.e. Ti^{3+}) in TiO_2 and "3" with substoichiometric TiO_x. Three components were also used to fit the O 1s spectra. The component labeled "1-2" is related to components "1" and "2" in the Ti $2p_{3/2}$ spectra and component "3" in the O 1s appears in concomitance with "3" in the Ti $2p_{3/2}$. Component "4" is needed to obtain a satisfactory fit of the O 1s spectra and its origin is uncertain[26–28].

The contribution of component "3" to the core-level spectra of both the amorphous and the subsequently formed TiO_2(B) film is negligible. Component "3" was indeed expected to be small in the as-deposited film according to previous studies[16]. The spectra show that even after annealing this peak is still negligible. The film is therefore mostly made of TiO_2, as indicated by peak "1", with a few defects, responsible for the presence of peak "2". This contribution accounts for about 5% of the total Ti $2p_{3/2}$ intensity. From the STM images it is difficult to judge whether the Ti^{3+} defects stems from point defects on the TiO_2(B)-(001) domains or from defects associated with domain boundaries. However, judging from the STM images, the domain boundaries can easily account for about 5% of the TiO_2(B) .

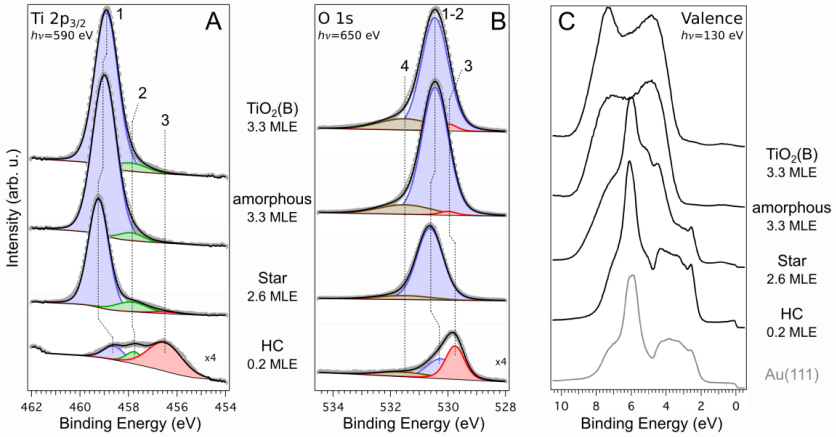

Figure 5. PES of the Ring-TiO_2/Au(111). (a) Ti $2p_{3/2}$, (b) O 1s core levels and of the (c) valence band for different TiO_x films on Au(111).
The topmost spectra belong to a sample presenting the TiO_2(B)(001) LEED pattern, obtained by low-temperature deposition and annealing; the second set of spectra belongs to the same sample before the annealing. The spectra of two other TiO_x structures, the HC and the Star obtained as described in Reference 16 are also presented for comparison. In (a) and (b), the deconvolution of the core-level spectra into different components is presented. Further details are discussed in the text.

The TiO_2(B) phase and the Star-TiO_2 phase present similar O 1s and Ti $2p_{3/2}$ spectra. However, the Au 4f core level spectra (not shown) reveal that the morphology of these two films is quite different. The relative intensity of the Au 4f surface component compared to the clean Au(111) was previously used as a measure of the fraction of uncovered surface on the sample. It was shown[16] that when equal amounts of Ti are present on the sample, a larger portion of the sample is covered if

the deposition is performed at lower temperature. The analysis of the Au 4f spectra in the present study is consistent with these results, the as-deposited, disordered TiO_2 film covers about 95% of the sample after deposition at 290 °C. Interestingly, annealing to 540 °C does not change this significantly and the ordered TiO_2(B) layer covers 93% of the substrate. In comparison, if the same amount of TiO_2 was deposited directly by CVD at 500 °C, only 60% of the sample is expected to be covered.

The different morphologies of the films are also apparent in the valence band spectra, Figure 5 (c). Both the spectra of the HC and of the Star phases exhibit a much more prominent contribution by the substrate compared to the TiO_2(B) film and to the amorphous TiO_2 film. The HC structure is a single-layer film, covering only a part of the surface. Hence, a strong contribution from the valence band of the Au(111) substrate is observed. The islands of Star-TiO_2, on the other hand, are thicker and the signal originating from the Au(111) substrate below is attenuated. In this case the large contribution of the Au to the valence spectra comes from the extended uncovered gold areas.

Finally, the valence band spectrum of the TiO_2(B) exhibits a strong peak at BE 7.3 eV, which develops after annealing of the amorphous film. According to theoretical electronic structure calculations, this binding energy regime is predominantly associated with Ti-O hybridized states[29]. Thus, the formation of Ti-O bonds within the TiO_2(B) can be monitored by the growth of the 7.3 eV peak in the valence photoemission spectrum. Moreover, the location of the valence band edge is estimated to be 3.27 ± 0.05 eV below the Fermi level. This would correspond to the band gap energy under the assumption that the Fermi level is located close to the conduction band edge. Since a certain degree of defects are indeed present this is very likely. In the literature a band gap value of 3-3.22 eV is reported[1]. Our result is in good correspondence with this value.

4. Discussion

The characterization of the TiO_2 film deposited at low temperature by TTIP CVD and subsequently annealed provide concordant evidences that the film has TiO_2(B) structure, exposing the (001) surface. Furthermore, the STM images of the film obtained for a Ti dose of 1.4 MLE show that the film is rather homogeneous, covering 75% of the Au(111) surface. Assuming formation of TiO_2(B), this coverage and Ti amount correspond to a film thickness of about 9.3 Å. This value is close to 1.5 times the distance between the (001) planes in TiO_2(B), which would be 9.4 Å (=1.5 x sin(107.16°) x 6.54 Å). Since each TiO_2(B) unit cell contains two layers of Ti atoms (see Figure 1), this thickness would correspond to three Ti layers.

Evidently, at a thickness of three Ti layers the central Ti layer forms the "bulk" of the film and the other two layers are one at the surface and another at the interface with Au. Thinner films would not comprise a bulk-like layer of Ti atoms. The fact that the height of the film in the STM image in Figure 3 is close to the minimum height required to have a bulk layer rationalizes the fact that the TiO_2(B) phase is not observed at lower Ti doses: if the local concentration of Ti is not sufficient to create a bulk layer, the TiO_2(B) phase cannot acquire the necessary stability. In other words, the results illustrate the importance of the metastabilizing role of the substrate-overlayer interactions, as well as the need to deposit an extended layer before increasing the temperature. The formation of the TiO_2(B) phase requires

heating to 500 °C, but it has to start from a wetting TiO_2 precursor layer formed at low temperature: this kinetically quenches the formation of thermodynamically more stable TiO_2 clusters. If deposition is carried out at 500 °C, TTIP decomposition and Ti-O diffusion is more facile and TiO_2 clusters will form. The clusters will act as reaction centers for further TTIP decomposition and continue to grow in an autocatalytic fashion, thereby preventing the formation of the TiO_2(B) layer, as illustrated schematically in Figure 6.

A comparison with growth on Pt(111) is motivated, since both Pt and Au are noble metals and to some extent the behavior can be expected to be similar. On Pt(111) a lepidocrocite TiO_2 structure is reported at 1-2 MLE[11], while TiO_2(B) grows between 2 MLE and 10 MLE[30]. Below approximately 5 MLE TiO_2(B) appears as islands on a wetting layer of reduced titania (TiO_x; $x<2$), while a more extended TiO_2(B) layer is observed ≥5MLE. Above 10 MLE, rutile TiO_2 is formed[30]. The rutile phase has a surface reconstruction very similar (the differences in the lattice constants between reference[16] and reference[30] are within error bars) to the Star phase - the other fully oxidized TiO_2 phase on Au(111).

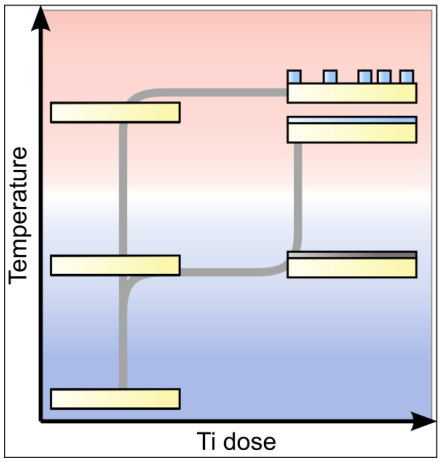

Figure 6. Scheme illustrating how different preparation routes can be chosen in order to control the structure and morphology of the TiO_2 overlayer. If the sample temperature is raised to above 500 °C (red region in the figure) before TTIP is dosed, the growth occurs in a high-temperature regime, where separate rutile-TiO_2 islands are formed. If more than 1 MLE of titania is deposited at a temperature between 200 °C and 300 °C (blue region), the formation of islands is prevented and an amorphous wetting film is obtained. The amorphous wetting layer can be ordered by a subsequent annealing to 500°C, generating an extended TiO_2(B) layer.

The TTIP-mediated growth on Au(111) show differences as compared to PVD growth on Pt(111). Firstly, we observe no sign of lepidocrocite formation on Au(111). Secondly, the nucleation of TiO_2(B) on Pt(111) involves transformation of the lepicocrocite double layer into TiO_2(B) islands on top of (or interspaced by) a single layer of reduced titania, i.e. a Stransky-Krastanov-like behavior[30]. In contrast, on Au(111) we are able to form an extended TiO_2(B) layer without the reduced wetting layer at coverages significantly lower than those needed to form extended TiO_2(B) on Pt(111). It is very likely that the difference in growth mode is caused by differences

on the TiO_2-substrate interactions. The TiO_2-Pt interactions are weak[11], but the TiO_2-Au interactions can be expected to be even weaker due to the more noble character of Au. Consequently, the TiO_2-Au interactions could be too weak to stabilize the lepidocrocite film. However, the kinetic barriers are still sufficient to prevent the formation of the thermodynamically more stable islands TiO_2 clusters upon heating.

Still, even though there are differences it is important also to stress the similarities observed despite different substrates (Au(111) vs Pt(111)) and preparation methods (CVD vs PVD). TiO_2(B) is observed in the low coverage regime on both Pt(111) (at 2 MLE) and on Au(111) (at about 1.4 MLE), where the influence of the substrate is greater. Furthermore, surface-reconstructed rutile island have been observed on Au(111) after preparation with several techniques[16,26,31]. This is considered to be the thermodynamically favored TiO_2 structure on Au. The same structure is found at high coverages on Pt(111)[30], when the interactions with the substrate are less relevant. Thus, the stability of this phase might be intrinsic, which is also compatible with the rutile structure being the most stable TiO_2 polymorph. These analogies support the idea that the results of these studies might be related to a common, more general behavior of the nanosized titania films on metal substrates.

5. Conclusions

On the basis of results obtained by LEED, STM, XAS and PES we have shown that TiO_2(B)(100) thin films can be grown on Au(111) by CVD using titanium(IV) isopropoxide as precursor. Specifically, it was shown that a two-step preparation procedure leads to a flat TiO_2(B) film, while a one-step procedure leads to separated islands, presumably of the rutile phase. Kinetic control is widely employed to obtain a desired reaction product and it was shown here that this strategy is a prerequisite for the formation of TiO_2(B) on Au(111). The finding of a route to obtain the TiO_2(B) structure in well ordered and ultra-clean form is important since the properties of TiO_2(B) can now be disclosed with minimal influence from uncertainties associated with cleanliness, phase impurities and structural defects. This enables a drastically improved comparison to the properties of anatase and rutile phases. The present study together with our previous work[16] form a picture of how both the atomic structure and the morphology of a titania film on Au(111) can be tailored. This insight could prove to be useful in future studies which either look after ways to produce a uniform coating titania layer, or explore strategies to maximize the Au-TiO_2 perimeter for catalytic purposes. Finally, the results show that there are common traits as well as slight differences between the growth of titania on Au(111) and Pt(111). In the future, the analogies between the growth of TiO_2 on Au and Pt could form a basis for a general model describing the growth of titania on a broader range of substrates.

Acknowledgements

Financial support was received from the Swedish Energy Agency (STEM), the Swedish Science Council (VR), the Trygger foundation, the Crafoord foundation, NordForsk and the Göran Gustafsson foundation. D.R. has been supported by the Anna Maria Lundins scholarship from Smålands Nation in Uppsala and L.E.W. has been supported through the Strategic Area Materials at NTNU. We thank the staff at MAX-lab for their support.

References

[1] M. Zukalová, M. Kalba, L. Kavan, I. Exnar, M. Graetzel, Chem. Mater. 17 (2005) 1248.

[2] R. Giannuzzi, M. Manca, L. De Marco, M.R. Belviso, A. Cannavale, T. Sibillano, C. Giannini, P.D. Cozzoli, G. Gigli, ACS applied materials & interfaces 6 (2014) 1933.

[3] T. Okumura, T. Fukutsuka, A. Yanagihara, Y. Orikasa, H. Arai, Z. Ogumic, Y. Uchimoto, J. Mater. Chem. 21 (2011) 15369.

[4] L. Qi, Y. Liu, C. Li, Appl. Surf. Sci. 257 (2010) 1660.

[5] A.R. Armstrong, G. Armstrong, J. Canales, R. García, P.G. Bruce, Advanced Materials 17 (2005) 862.

[6] G. Armstrong, A.R. Armstrong, P.G. Bruce, P. Reale, B. Scrosati, Advanced Materials 18 (2006) 2597.

[7] Q. Wang, Z.H. Wen, J.H. Li, Adv. Funct. Mater. 16 (2006) 2141.

[8] C.-C. Tsai, Y.-Y. Chu, H. Teng, Thin Solid Films 519 (2010) 662.

[9] J. Qu, X.P. Gao, G.R. Li, Q.W. Jiang, T.Y. Yan, J. Phys. Chem. C 113 (2009) 3359.

[10] K. Yamamoto, H. Shimoita, K. Tomita, K. Fujita, M. Kobayashi, V. Petrykin, M. Kakihana, J. Ceram. Soc. Jpn. 117 (2009) 347.

[11] A. Vittadini, F. Sedona, S. Agnoli, L. Artiglia, M. Casarin, G.A. Rizzi, M. Sambi, G. Granozzi, Chemphyschem : a European journal of chemical physics and physical chemistry 11 (2010) 1550.

[12] F. Sedona, G.A. Rizzi, S. Agnoli, F.X. Llabrés i Xamena, K. Schierbaum, G. Granozzi, J. Phys. Chem. B 109 (2005) 24411.

[13] P. Finetti, F. Sedona, G. a. Rizzi, U. Mick, K. Schierbaum, G. Granozzi, Surf. Sci. 604 (2010) 366.

[14] A. Schaefer, D. Ragazzon, A. Wittstock, L.E. Walle, A. Borg, M. Bäumer, A. Sandell, J. Phys. Chem. C 116 (2012) 4564.

[15] A. Schaefer, D. Ragazzon, L.E. Walle, M.H. Farstad, A. Wichmann, M. Bäumer, A. Borg, A. Sandell, Appl. Surf. Sci. (2013) .

[16] D. Ragazzon, a. Schaefer, M.H. Farstad, L.E. Walle, P. Palmgren, a. Borg, P. Uvdal, a. Sandell, Surf. Sci. 617 (2013) 211.

[17] R. Nyholm, S. Svensson, J. Nordgren, A. Flodstr, Nuclear Instruments and Methods in Physics Research A 246 (1986) 267.

[18] R. Nyholm, J.N. Andersen, U. Johansson, B.N. Jensen, I. Lindau, Nucl. Instrum. Meth. A 467-468 (2001) 520.

[19] M. Ben Yahia, F. Lemoigno, T. Beuvier, J.-S. Filhol, M. Richard-Plouet, L. Brohan, M.-L. Doublet, The Journal of chemical physics 130 (2009) 204501.

[20] A. Vittadini, M. Casarin, A. Selloni, J. Phys. Chem. C 113 (2009) 18973.

[21] C. Wu, M.S.J. Marshall, M.R. Castell, J. Phys. Chem. C 115 (2011) 8643.

[22] U. Diebold, Surf. Sci. Rep. 48 (2003) 53.

[23] R. Ruus, A. Kikas, A. Saar, A. Ausmees, E. Nommiste, J. Aarik, A. Aidla, T. Uustare, I. Martinson, Solid State Commun. 104 (1997) 199.

[24] V.S. Lusvardi, M.A. Barteau, J.G. Chen, J. Eng Jr., B. Frühberger, A. Teplyakov, Surf. Sci. 397 (1998) 237.

[25] R. Brydson, H. Sauer, W. Engel, J.M. Thomas, E. Zeitler, N. Kosugill, Journal of physics. Condensed matter : an Institute of Physics journal 1 (1989) 797.

[26] D. V. Potapenko, J. Hrbek, R.M. Osgood, ACS Nano 2 (2008) 1353.

[27] Z. Song, J. Hrbek, R. Osgood, Nano Lett. 5 (2005) 1327.

[28] J. Biener, E. Farfan-Arribas, M. Biener, C.M. Friend, R.J. Madix, J. Chem. Phys. 123 (2005) 94705.

[29] G. Drera, L. Sangaletti, F. Bondino, M. Malvestuto, L. Malavasi, Y. Diaz-Fernandez, S. Dash, M.C. Mozzati, P. Galinetto, Journal of physics. Condensed matter : an Institute of Physics journal 25 (2013) 075502.

[30] E. Cavaliere, L. Artiglia, G.A. Rizzi, L. Gavioli, G. Granozzi, Surf. Sci. 608 (2013) 173.

[31] K. Lauwaet, K. Schouteden, E. Janssens, C. Van Haesendonck, P. Lievens, Phys. Rev. B 83 (2011) 155433.

Paper III

Structure of a pinwheel-like TiO_x single layer phase on Au(111)

D. Ragazzon, M.H. Farstad, A. Schaefer, L.E. Walle, P. Uvdal, P. Palmgren, A. Borg, A. Sandell

In manuscript

Structure of a pinwheel-like TiO_x single layer phase on Au(111)

D. Ragazzon[1], M. H. Farstad[2], A. Schaefer[3], L. E. Walle[2], P. Uvdal[4,5], Pål Palmgren[6], A. Borg[2] and A. Sandell[1,*]

[1] *Dept. of Physics and Astronomy, Uppsala University, P. O. Box 516, SE-75120 Uppsala, Sweden*
[2] *Dept. of Physics, Norwegian University of Science and Technology (NTNU), NO-7491 Trondheim, Norway*
[3] *Institute of Applied and Physical Chemistry, University of Bremen, Box 33 04 40, D-28359 Bremen, Germany*
[4] *Chemical Physics, Dept. of Chemistry, P.O. Box 124*
[5] *MAX-IV Laboratory, P.O. Box 118, Lund University, SE-221 00 Lund, Sweden*
[6] *VG Scienta, Uppsala, SE-752 28, Sweden*

An ordered TiO_x 2D phase has been grown on Au(111) by chemical vapor deposition and subsequent annealing. This phase was characterized by means of low-energy electron diffraction (LEED), synchrotron radiation photoelectron spectroscopy (PES) and scanning tunneling microscopy (STM). The contrast in STM images resembles a pinwheel (PW), comprising triangular units in a circular arrangement with hubs in the center. The phase has only been observed at Ti coverages between 0.1 and 0.5 monolayers. We also report that the PW phase can be formed by annealing of a honeycomb Ti_2O_3 phase. A Moiré-like model for the structure of the PW phase was constructed along guidelines found for similar TiO_x pinwheel-like phases on metal substrates. Within this model, the structure can be described in terms of pseudoepitaxial regions with dislocation lines and characteristic defects. Comparisons are made with other PW phases on metals, providing further insight into the importance of the interactions between the overlayer and the substrate.

1. INTRODUCTION

During the last decade, two-dimensional oxides have garnered a growing importance in chemistry, physics and materials science. This development largely owes to the field of surface science, where techniques have been developed that allow for controlled preparation followed by atomic-level spectroscopic and microscopic characterization. On numerous occasions, surface science methodology has been employed to prepare nanoscale oxide films with new and unexpected geometric and electronic properties[1–7]. It is anticipated that successful integration of two-dimensional oxides in various devices will open up completely new avenues to tailored functional materials for a wide range of applications and technologies.

Titania has a number of applications, such as catalysis, photocatalysis and photodegradation of carbon compounds and hybrid solar cells[8–16]. There are several studies of growth of ultrathin titania films on metals. The vast majority has been prepared by evaporation and oxidation of Ti. Most notable here is the extensive work on titania films on Pt single crystal surfaces undertaken by Granozzi et al., in which a multitude of atomically ordered phases have been discovered and characterized[17–25]. Ordered ultrathin phases of titanium oxide have also been observed as TiO_x films on encapsulated Pd(111) nanoparticles on TiO_2(110)[26,27] and on Au(111)[28,29] - the substrate employed in this work. On all these surfaces, a peculiar structure has been observed, which when imaged with STM gives rise to a contrast that comprises triangular units in a circular arrangement. The arrangement resembles pinwheels with spokes and hubs.

The pinwheel (PW) structures have been proposed to be single layer TiO_x ($x \leq 1.5$) with a "large" periodic unit cell[20]. Despite this, they have been often conveniently described in literature as a layer with "shorter" periodicity forming a Moiré-like structure. This choice is based on very good grounds, as can be seen by the emblematic case of the *w*-TiO_x on Pt(111). This structure was initially presented as a Moiré-like pattern[17], generated by the combined periodicities of the substrate and a hexagonal overlayer of Ti atoms (henceforth "Ti lattice"), generating a coincidence structure. The different contrast of the Ti atoms was at the origin of the wagon-wheel structure observed by STM while the O atoms were not observed. In a subsequent study calculations based on density-functional theory (DFT) were used to obtain a model for the *w*-TiO_x phase[20]. In this model, the Ti atoms in the hubs are missing and a large unit cell is needed to explain the arrangement of Ti and O atoms in the overlayer. It also proved the power of the Moiré-like description: there is a remarkable agreement between the position of the Ti atoms in the Moiré model and the ones predicted by DFT (cf. reference[17] with reference[20]). The Moiré-like model has also been adopted for the interpretation of the PW phases on Au(111)[28] and Pd(111)[27].

Recently, we presented results obtained after growth of titania on Au(111) using titanium(IV) isopropoxide (TTIP), a common precursor molecule for chemical vapor deposition (CVD) of TiO_2[30]. With this deposition technique, several ordered structures were grown: At low coverages a (2x2) Ti_2O_3 film with honeycomb structure (HC) wets the surface. An ordered form of TiO_2 grows as islands at higher deposition temperatures (500 °C). Deposition of en extended amorphous layer at low temperature and subsequent annealing to higher temperature (<500 °C) generates a TiO_2(B) (001) layer.

In the present work, we continue by addressing the formation of the TiO_x pinwheel (PW) phase on Au(111). We are able to show that the PW phase can be

formed by annealing of the HC phase, which implies that the coverage needs to be within a certain regime. On the basis of low-energy electron diffraction (LEED) and STM we derive a structure model within the framework of the Moiré model and discuss defects in the structure. Comparisons are also made with the PW structures reported on Au(111)[28], Pt(111)[18,20,21] and Pd(111)[26,27] encapsulated islands on TiO_2.

2. EXPERIMENTAL

The experiments were conducted in different ultrahigh vacuum (UHV) chambers, with base pressure in the low 10^{-10} mbar range. Low-energy electron diffraction (LEED) could be measured in all the chambers. The high-resolution photoelectron spectroscopy (PES) measurements were performed at the MAX II ring of the MAX IV Laboratory, Sweden, at beamlines D1011[31] and I311[32]. Ti 2p, and O 1s PES spectra were acquired in normal emission with photon energies 590 eV and 650 eV, respectively. The binding energy (BE) is reported with respect to the Fermi level of the Au(111) substrate. The STM measurements were done at Uppsala University with an Omicron VT-STM. This chamber also allowed for low energy electron diffraction (LEED), which was used to relate the preparations to the ones obtained at the synchrotron.

The Au(111) sample was cleaned and its surface ordered by performing several cycles of sputtering and annealing, following the recipe in reference[30]. The sample was considered clean when it exhibited a sharp LEED pattern of the Au(111) herringbone reconstruction and no contaminants were detected by PES.
The titania film was prepared by dosing titanium(IV) isopropoxide (TTIP, Sigma–Aldrich, purity 99.999%) on the sample, using a doser positioned a few centimeters from the sample. During deposition, a leak-valve was used to control the TTIP pressure in the chamber. The typical pressures were between $1 \cdot 10^{-9}$ mbar and $5 \cdot 10^{-8}$ mbar. The TTIP was purified by freeze–pump–thaw cycles and the TTIP pumping line was baked.

The Ti coverage on the sample is given in monolayer equivalents (MLE), where 1 MLE is defined as 0.138 $Å^{-2}$, i.e. a number of atoms equal to the surface density of Au(111). The unit MLE does not carry any information about the actual structure of the layer: and it is only a way to express the number of atoms on the sample.

3. STRUCTURE DEFINITION

It is convenient to define a special notation to describe the PW structures. A coincidence structure occurs when a lattice vector of the overlayer coincides with one of the substrate. This vector is named $\mathbf{c_1}$ and describes the overall periodicity of the substrate-overlayer coincidence structure. By denoting as $\mathbf{a_1}$ and $\mathbf{a_2}$ and $\mathbf{b_1}$ and $\mathbf{b_2}$ the base vectors of the substrate and the overlayer, respectively, this condition can be expressed as

$$h\,\mathbf{a_1} + k\,\mathbf{a_2} = m\,\mathbf{b_1} + n\,\mathbf{b_2} := \mathbf{c_1}$$

where *h*, *k*, *m* and *n* are integer numbers. Unless otherwise specified, the base vectors of the hexagonal lattices are chosen so that they form an acute angle; also *h* and *m* will be chosen to be greater than *k* and *n*, respectively.

For structures with six-fold symmetry (as is the case here), the description of the coincidence structure is complete when $\mathbf{c_1}$ is given, since the second vector $\mathbf{c_2}$ can be obtained by rotating $\mathbf{c_1}$ by 60°. Once *h*, *k*, *m* and *n* are fixed, the positions of the Ti atoms are unequivocally determined and other structural properties can be expressed in terms of these constants. We will henceforth use the notation (*h*,*k* – *m*,*n*) to identify this coincidence structure. This choice is beneficial since these constants can be directly related to the experimental measurements, both in real and reciprocal space (see later in the text).

In the present work, a PW structure on Au(111) upon TTIP-CVD and subsequent annealing is presented. The data will provide evidences that a (8,4 – 7,4) structure is compatible with the experimental results. Figure 1 illustrates the (8,4 – 7,4) coincidence structure to exemplify the notation used. In this context, it can be noted that the common Woods notation would in this case be redundant, as the length of both sides of the unit cell is the same, and less informative, since it would not provide any information about the periodicity of the Ti lattice. For instance, the Woods notation for the (8,4 – 7,4) presented in Figure 1 is (√112x√112)R19.1°.

4. RESULTS

The pinwheel structure was prepared in two steps. First, TTIP was deposited on the clean Au(111) surface while keeping the sample at 280 °C. This was followed by annealing to about 550°C. PW structures were observed when the initial amount of Ti on the sample was in the range between 0.1±0.05 MLE and 0.5±0.2 Monolayer-equivalent (MLE). The PW phase was not observed upon annealing a film with a coverage of 0.8±0.3 MLE, which gives an indication of the critical upper limit.

LEED: Upon deposition of a sub-critical coverage at 280°C, a (2x2) HC Ti_2O_3 film is formed as witnessed by LEED and PES (cf. below). This is in accordance with previous studies[30]. Annealing of the sample above 500 °C led to the appearance of the LEED pattern shown in Figure 2. The picture shown in the figure was calibrated by using the position of the diffraction spots of the Au(111) substrate; the reciprocal-space unit cell of the substrate is shown by a dotted line. The expected diffraction patterns of two symmetric domains of a (8,4 – *m*,*n*) PW structure have been superimposed on the picture and indicated with light and dark green circles. The unit cells of the two domains are also marked. It can be shown that by choosing an appropriate basis to describe the reciprocal lattice of an (*h*,*k* – *m*,*n*) structure, the reciprocal lattice vector of the substrate can be expressed as a combination of these vectors with coefficients *h* and *k*: i.e., in the present case, the position of the lattice spots can be reached from the center by moving by 8 lattice points in one direction and then by 4 points 60° to the side. This motivates the choice of describing the structure with the (*h*,*k* – *m*,*n*) notation, as these parameters can easily be related to measured quantities.

Next to each substrate spot, two spots, one for each PW domain, appear quite intense. This could be expected from a Moiré structure, where the whole pattern is generated by the combination of two dominant periodicities: the one of the substrate and the one of the overlayer. It is therefore reasonable that the position of these bright

spots is related to the periodicity of the overlayer. These spots are found at the position indicated by a combination of the base vectors of the Moiré pattern with coefficients *m* and *n*. By counting the number of spots from the center, one obtains 7 and 4. The fact that the intense Au and Ti spots are next to each other, indicates that *k*=*h*-1(or *n*=*m*-1). This means that (8,4 – 7,4) is a valid suggestion for the structure generating the LEED pattern. Other possibilities could however be taken into account, given the experimental uncertainty. Figure 3 presents a detail of the pattern, showing the region around one of the Au(111) spots. The pattern associated with the (8,4 – 7,4) is marked in green and fits quite well the experimental one. The illustration shows that the (9,4 – 8,4), also marked in green, is also in very good agreement with the observed pattern. It is also shown that the pattern, marked in red, expected from the (7,2 – 6,2) structure reported upon PVD growth[28] is not compatible with the LEED pattern observed after the CVD preparation (and the LEED patter of the PVD-grown PW was not mentioned). This discrepancy is beyond experimental uncertainty, although minor radial deformation could occur when mapping the picture onto the reciprocal space, angular distortions causing the appearance of the pattern to change radically are not expected given the symmetry of the substrate.

STM: STM images of a sample presenting the PW LEED pattern are presented in Figure 4. Figure 4(a) shows a PW island formed next to a step of the Au(111); the clean Au(111) terrace can be identified by the presence of the characteristic herringbone reconstruction. The PW island appears on average 1.7 Å higher than the underlying gold and its surface is covered by a pinwheel motif. The latter arises from the arrangement of triangular units, delimited by three brighter "spokes" and arranged around a "hub", creating the PW contrast. It is noteworthy that the spokes define the rim of the island. This suggests that the PW is made with the triangular features as the fundamental building blocks.

High-resolution images, as the one in Figure 4(b), resolve the triangles and the spokes into round features. The appearance of the PW arises from the higher apparent height of the features defining the spokes and the hubs. According to previous works[13,28,30], we interpret these features as Ti atoms, while O atoms are not visible under these imaging conditions. The changes in the apparent height are ascribed to different chemical environments and/or occupations of different sites on the Au(111) surface (see below). The hubs of the wheels appear as dark spots in the image; this was previously attributed to the absence of a Ti atom for the PVD-grown PW on Au(111)[28] and Pd(111)[27], and in the case of the *w*-TiOx on Pt(111) this assumption was also supported by DFT calculations[20].

The lattice constant of the PW structure shown in Figure 4(b) corresponds to the distance between the hubs, which varies from 25 Å to 30 Å between different STM images and also within the same images if measured in different directions. The changes are likely due to drift in the images, making the measurement of the lattice constants through these STM images less reliable than the one done by LEED, which uses the spots of the substrate as an internal calibration standard. The PW structure image also presents irregularities such as "double hubs", different number of Ti atoms between the hubs and spokes interrupted in different positions. The presence of these defects suggests that the energy required to form these defects might not be much higher than the one to form the ideal PW. The discussion below will try to give a deeper insight into the reasons why such defects can be present. A consequence of the defects is that they add to the uncertainty in measuring the PW structure parameters *m* and *n* by counting the number of Ti atoms between two hubs. To reduce this problem,

a larger atomically-resolved image was used, and *m* and *n* were measured from the Fourier transform of the image. This is a way to obtain the averaged values of *m* and *n*. It is known that the Fourier transform of an STM image corresponds to its LEED pattern. Values of *m* and *n* can be obtained from the Fourier transform of the STM image with a method analogous to the one used to obtain *h* and *k* from the LEED pattern.

Figure 5 presents (a) an atomically resolved STM image of the PW phase on a larger scale and (b) its Fourier transform. The most intense components of the latter correspond to the (averaged) dominant periodicities on the surfaces. The Fourier transform is mapped onto the reciprocal space in Figure 5(c), imposing a hexagonal symmetry in order to correct for distortions in the STM image. Six intense spots correspond to the ones describing the periodicity of the Ti lattice. Regular, less intense spots are seen between them and the center of the image. These are related to the smaller (in the reciprocal space) unit cell of the PW. The intensity closer to the center comes from non-periodic components in the image. Strong additional contributions in the horizontal and vertical directions in the STM image are artifacts (e.g. due to the alignment of the scanning lines) and their Fourier components were removed in order to enhance the ones related to the PW. The expected position of the reciprocal-lattice spots for the (*h*,*k* – 7,4) and (*h*,*k* – 7,3) structures are superimposed, using blue and red circles, respectively. Both possibilities are acceptable within the experimental uncertainty. Within the discussed experimental uncertainty, the (8,4 – 7,4) structure seems to be the one that agrees best with the both LEED and STM data. For the sake of clarity, this structure will be used henceforth when describing the PW.

This analysis could have been performed in terms of lattice constants and angles, along the guidelines described by Wu et al.[28], and would have led to completely equivalent results, in principle. Under the assumption that the PW is a coincidence structure, measuring *h*, *k*, *m* and *n* has the advantage that these quantities are integer numbers, and thus not affected by drift or other distortions of the images: the fact that the number of spots counted on the images does not change makes the method more robust.

PES: The Ti $2p_{3/2}$ and O 1s PES spectra of the PW phase are presented at the bottom of Figure 6(a) and (b) respectively, along with spectra measured for the other ordered structures on Au(111). In accordance with previous work[30], the Ti $2p_{3/2}$ component labeled "3" is characteristic of the HC phase, while "1" and "2" are related to oxidized TiO_2 structures that grow besides the HC. Specifically, the state labeled "1" is assigned to Ti^{4+} in stoichiometric TiO_2 and state "2" to defects generating reduced Ti, i.e. Ti^{3+}. Consequently, component "1" is the dominating one for the ordered TiO_2 islands grown at 500°C (third spectrum from bottom) while a minor contribution from defects is found. At sample coverages higher than the ones investigated in the present paper, low-temperature CVD and subsequent annealing of the sample generates a TiO_2(B)(001) layer[33], whose spectra are presented at the top of Figure 6. As expected for a TiO_2 phase, the spectrum comprises components "1" and, to a minor extent, component "2". Importantly, an additional Ti $2p_{3/2}$ component, labeled "0", is needed to fit the spectra of the PW (bottom), accounting for the appearance of this new phase. The Ti $2p_{3/2}$ binding energy of the component associated with the PW phase is 455.5 eV. Peaks at this BE have previously been associated with Ti^{2+} [17].

The O 1s spectra in Figure 6(b) can be described in terms of two main components[30] and a broad structure (labeled "4") that might be related to defects or hydroxyl groups. The peak labeled "0-1-2" appears in connection to the TiO_2 and PW

phases on Au(111). The HC phase is associated with peak "3" at a BE of 529.7 eV and is related to peak "3" in the Ti $2p_{3/2}$ spectra. That the O 1s BE of the HC phase differs from the other phases, can be due to a difference in O coordination; in the HC phase the O atoms have a two-fold coordination instead of three-fold[30]. However, the O 1s peak "0-1-2" is also observed together with the HC related state "3" because TiO_2 clusters are also growing at the conditions where the HC phase is formed.

As noted above, annealing of a situation where the HC phase dominates to 500°C generates the PW phase. This is confirmed by the core level spectra shown in Figure 6, which do in fact illustrate that "0" is absent in the spectra of the HC, recorded prior the annealing, and appears after annealing the sample lead to the formation of the PW. The comparison of the spectra of the HC and the PW shows that during the annealing feature "3" disappears completely from the O 1s spectrum, meaning that the HC phase is no longer present. This finding is in accordance with the disappearance of the bright (0,1/2) LEED spots of the HC phase. From this follows that component "3", used to fit the Ti $2p_{3/2}$ spectrum, cannot be related to the presence of the HC phase. The reason why this component is still needed to fit the spectra correctly can be that different Ti species are present in the PW structure (as discussed below) and/or that the Ti peak "0" is asymmetric. In this case, "3" should be considered as an effective way to model the asymmetry. The latter can be expected for sub-stoichiometric Ti films, which can exhibit metallic behavior.

A final consideration involves the intensities of PES peaks. After annealing, the intensity of the PES spectra decreased: part of the film left the surface of the sample. Oxygen can leave the sample at 500 °C, while the lack of titanium is possibly due to diffusion of metallic Ti into the bulk. Interestingly, while "3" disappeared completely from the O 1s spectrum, the intensity of "0-1-2" increased: part of the O species remained on the surface, but changed their chemical nature during annealing. Following the suggestion that component "3" was due to two-fold coordinated oxygen, we tentatively interpret this result as a change in the coordination of the O, from two in the HC phase before annealing to three in the PW phase after annealing.

5. DISCUSSION

The results demonstrate that a pinwheel (PW) titania structure can be prepared by exposure to TTIP at 280°C followed by annealing to 500°C. The prerequisite is that the amount of Ti is below a critical coverage; the upper limit was estimated to lie between 0.5 MLE and 0.8 MLE. In this coverage regime, deposition at 280°C yields a single layer HC phase with (2x2) periodicity with respect to the Au(111) substrate. The results convincingly show that the HC can be transformed into the PW upon annealing. The Ti atoms of the PW form a coincidence-like structure with the atoms of the hexagonal substrate, which can be described using the $(h,k-m,n)$ notation. A (8,4 – 7,4) PW showed a good agreement with all the measured data. However, in order to complete the description, the position of the O atoms needs to be determined.

In the previous studies of similar structures formed on Pt(111) building principles determining the structure of ultrathin films have been proposed[3,21]. The underlying idea presented in reference[21] is that a TiO_x ultrathin film would tend to form a hypothetical TiO layer with hexagonal structure, where Ti atoms form a monolayer, occupying half of the hollow sites (fcc or hcp) of the substrate, and O atoms form a second layer occupying half of the hollow sites of the Ti layer. In such a structure, each Ti atom is surrounded by three O atoms (three-fold coordinated, Ti_3).

However, this does not happen if (i) the stoichiometry of the film is higher than 1:1 and (ii) there is a mismatch between the optimal lattice constant of the film and the one of the substrate. Instead, smaller triangular islands with quasi-hexagonal structure similar to the hypothetical TiO layer are formed, separated by dislocation lines separated by domain boundaries. Ti_3 atoms occupy fcc sites on one side of the boundary and hcp sites on the other. The boundary is made of four-fold coordinated Ti_4 atoms, located on (or close to) bridge sites of the substrate. This arrangement allows both releasing stress and accommodating more O atoms in the structure to match the required stoichiometry.

The rules outlined above have been applied to the PW phase on Au(111). The result is shown in Figure 7. Firstly, the Ti lattice (shown using light and dark blue spheres in the Figure) was drawn as specified by the (8,4 – 7,4) model. Secondly, it was placed onto the Au(111) surface with one Ti atom occupying an fcc position. This automatically caused the surrounding Ti atoms occupy near-fcc positions, other atoms to be on hcp or near-hcp sites and between these a line of atoms in bridge or near-bridge positions. On either side of the line a Ti atom is located on top of a Au atom. Thirdly, following the suggested building principle, three O atoms (red spheres in the figure) were placed around the Ti atoms on or near the fcc and hcp positions: this procedure forms triangular islands, comprised by either Ti_3 on (or near) fcc or on hcp sites. The Ti on bridge sites, located at the border between the islands, were added O atoms until they reached a coordination of four. A darker shade of blue has been used to indicate the Ti_3 and a lighter one for the Ti_4. The resulting picture resembles the qualitative features of the PW structure imaged by STM.

A further analysis of the structure shows that O atoms are rather close to each other along the spokes, as in position I in Figure 7. The distance between two O atoms occupying neighboring hcp and fcc sites in the (8,4 – 7,4) lattice PW is 1.83 Å. This distance is about two thirds of the atomic diameter of the ion O^{2-}. Repulsion between the two O^{2-} ions is then expected, a separation which can in turn compress the neighboring parts of the TiO_x overlayer. This kind of site might be responsible for relieving stress in the film. Other parts of this structure present O atoms that are even closer to each other. The region labeled II in the figure shows O atoms on three consecutive hollow sites. It is possible that a local rearrangement of the atoms occurs in order to avoid this arrangement and lower the local energy. This solution was indeed adopted in the DFT-derived model of the *w*-TiO_x[20]. A second possibility would be to remove the Ti_3 atom at the hubs and its three surrounding oxygens. In fact, all of the suggested PW models[18,20,21,27,28] lack of an atom in the hub. Finally, region III shows four O atoms in consecutive hollow sites. For the same reason as for regions I and II, it is very likely that a rearrangement or removal of some O atoms occurs in this position.

Nevertheless, the model outlined above seems to capture the essence of the structure of the phase. The stress-relief mechanism along the spokes could be due to regions of type I. The model might not describe correctly areas II and III, but points out that they show the highest deviation from the ideal quasi-hexagonal lattice. Therefore they are expected to be less stable than the rest of the film. Region III is found at the position where there is a discontinuity in the spoke. The position of this discontinuity was observed to vary in the STM images (see Figure 4(b)), indicating that these sites are more prone than others to presenting defects. Region II is located near the hub, which also tend to present irregularities.

The final considerations regard the comparison with the (7,2 – 6,2) PW phase produced on Au(111) by PVD and subsequent annealing to 600 °C in 10^{-8} mbar O_2[28].

As already discussed, this structure is not compatible with the LEED pattern presented here, where a (8,4 – 7,4) PW structure is the most plausible one. However, we find it possible that two (or more) different PW-like phases can be formed on Au(111). Two PW phases have been observed on Pt(111), denoted *w´* and *w*. The *w'*-TiO_x phase is converted into the *w*-TiO_x phase upon annealing at 550 °C in 10^{-7} mbar O_2. This transformation entails a change of the Ti lattice constant from 3.26 Å to 3.18 Å. The process is reversed if the sample is heated in UHV at 450 °C. From this follows that the *w'* is less oxidized than the *w* phase. On Au(111), the PW phase reported here (formed by CVD and heating) has a Ti lattice constant of 3.27 Å, while that formed by PVD has a Ti lattice constant of 3.17 Å. These values are very similar to those for the *w'* and *w* phases, making an analogy with Pt(111) quite plausible. That is, it is possible that the two different PW phases reported on Au(111) differ in the degree of oxidation. Future experiments addressing oxidation and reduction of the PW phases on Au(111) are therefore highly motivated.

Despite many similarities, the behavior of TiO_x films on Pt(111) and Au(111) presents also differences. In this paper we reported that the HC-TiO_x becomes the (8,4 – 7,4) PW upon annealing in UHV. The *k*-TiO_x on Pt(111) has the same atomic arrangement as the HC on Au(111). Annealing of this phase produces a different phase, the *z'*-TiO_x[17]. The latter is made of set of triangular building blocks similar to the ones making the PW, but arranged in lines where every other triangle is upside-down, rather than in wheels. Thus, the brighter borders of the triangles gives the *z'*-TiO_x a characteristic zigzag motif. The reason that no *z'*-TiO_x phase has been observed on Au(111) could simply be that the preparation procedure has to be refined. Another possibility is that the formation of the *z'*-TiO_x phase is made possible by a stabilizing mechanism on Pt(111) that is not present on Au(111). In this context, it is important to note that a lepidocrocite film has been observed on Pt(111) but not on Au(111)[17]. The lepidocrocite film is formed when the *z'*-TiO_x phase is annealed in O_2[17]. Since neither the lepidocrocite nor the *z'*-TiO_x phase are observed on Au(111) this supports the presence of a certain stabilization mechanism for TiO_x/Pt(111) that is absent for TiO_x/Au(111) and that this leads to a richer phase diagram on Pt(111). However, it cannot be excluded that a more extended exploration of preparation routes may lead to the discovery of additional phases on Au(111).

6. CONCLUSIONS

We demonstrated the formation of an ordered 2D TiO_x pinwheel-like phase on Au(111) upon chemical vapor deposition and subsequent annealing. The pinwheel-like appearance is apparent in STM images and additional characterization was carried out with low-energy electron diffraction (LEED), synchrotron radiation photoelectron spectroscopy (PES) and scanning tunneling microscopy (STM). The PW phase was only observed at Ti coverages between 0.1 and 0.5 monolayers. LEED and PES results show unambiguously that the phase can be formed by annealing of a honeycomb Ti_2O_3 phase. The PW phase fits into a general frame of such structures adopted by TiO_x ultrathin films grown on metallic (111) surfaces. A Moiré-like model for the atomic structure was constructed, showing triangular regions with dislocation lines and characteristic defects. A comparison with previous results obtained for TiO_x/Pt(111) and TiO_x/Au(111) yields the possibility for having two (or more) PW phases on Au(111) with different degrees of oxidation. It is also suggested that

Pt(111) is capable of stabilizing a wider range of different titania phases than Au(111).

7. ACKNOWLEDGEMENTS

Financial support was received from the Swedish Energy Agency (STEM), the Swedish Science Council (VR), the Trygger foundation, the Crafoord foundation, NordForsk and the Göran Gustafsson foundation. D.R. has been supported by the Anna Maria Lundins scholarship from Smålands Nation in Uppsala and L.E.W. has been supported through the Strategic Area Materials at NTNU. We thank the staff at MAX-lab for their support.

REFERENCES

[1] H. Kuhlenbeck, S. Shaikhutdinov, H.-J. Freund, Chemical Reviews 113 (2013) 3986.

[2] G. Pacchioni, Chemistry (Weinheim an der Bergstrasse, Germany) 18 (2012) 10144.

[3] S. Surnev, A. Fortunelli, F.P. Netzer, Chemical Reviews 113 (2013) 4314.

[4] F.P. Netzer, F. Allegretti, S. Surnev, Journal of Vacuum Science & Technology B: Microelectronics and Nanometer Structures 28 (2010) 1.

[5] N. Nilius, Surf. Sci. Rep. 64 (2009) 595.

[6] H.-J. Freund, G. Pacchioni, Chemical Society Reviews 37 (2008) 2224.

[7] L. Giordano, G. Pacchioni, Acc. Chem. Res. 44 (2011) 1244 .

[8] C. Lun Pang, R. Lindsay, G. Thornton, Chemical Society Reviews 37 (2008) 2328.

[9] Z. Dohnálek, I. Lyubinetsky, R. Rousseau, Prog. Surf. Sci. 85 (2010) 161.

[10] A. Fujishima, K. Honda, Nature 238 (1972) 37.

[11] M. Grätzel, Nature 414 (2001) 338.

[12] M.A. Henderson, Surf. Sci. Rep. 46 (2002) 1.

[13] U. Diebold, Surf. Sci. Rep. 48 (2003) 53.

[14] C.L. Pang, R. Lindsay, G. Thornton, Chemical Reviews 113 (2013) 3887.

[15] O. Carp, C.L. Huisman, A. Reller, Prog. Solid State Chem. 32 (2004) 33.

[16] M. A. Henderson, Surf. Sci. Rep. 66 (2011) 185.

[17] F. Sedona, G.A. Rizzi, S. Agnoli, F.X. Llabrés i Xamena, K. Schierbaum, G. Granozzi, J. Phys. Chem. B 109 (2005) 24411.

[18] F. Sedona, S. Agnoli, G. Granozzi, The Journal of Physical Chemistry. B 110 (2006) 15359.

[19] E. Cavaliere, L. Artiglia, G.A. Rizzi, L. Gavioli, G. Granozzi, Surf. Sci. 608 (2013) 173.

[20] G. Barcaro, S. Agnoli, F. Sedona, G.A. Rizzi, A. Fortunelli, G. Granozzi, J. Phys. Chem. C 113 (2009) 5721.

[21] G. Barcaro, E. Cavaliere, L. Artiglia, L. Sementa, L. Gavioli, G. Granozzi, A. Fortunelli, J. Phys. Chem. C 116 (2012) 13302.

[22] A. Vittadini, F. Sedona, S. Agnoli, L. Artiglia, M. Casarin, G.A. Rizzi, M. Sambi, G. Granozzi, Chemphyschem 11 (2010) 1550.

[23] L. Artiglia, T. Diemant, H. Hartmann, J. Bansmann, R.J. Behm, L. Gavioli, E. Cavaliere, G. Granozzi, Physical Chemistry Chemical Physics : PCCP 12 (2010) 6864.

[24] P. Finetti, F. Sedona, G.A. Rizzi, U. Mick, F. Sutara, M. Svec, V. Matolin, K. Schierbaum, G. Granozzi, J. Phys. Chem. C 111 (2007) 869.

[25] L.E. Walle, S. Agnoli, I.-H. Svenum, a Borg, L. Artiglia, P. Krüger, a Sandell, G. Granozzi, The Journal of Chemical Physics 135 (2011) 054706.

[26] M. Bowker, P. Stone, P. Morrall, R. Smith, R. Bennett, N. Perkins, R. Kvon, C. Pang, E. Fourre, M. Hall, J. Catal. 234 (2005) 172.

[27] R.A. Bennett, C.L. Pang, N. Perkins, R.D. Smith, P. Morrall, R.I. Kvon, M. Bowker, J. Phys. Chem. B 106 (2002) 4688.

[28] C. Wu, M.S.J. Marshall, M.R. Castell, J. Phys. Chem. C 115 (2011) 8643.

[29] J. Biener, E. Farfan-Arribas, M. Biener, C.M. Friend, R.J. Madix, J. Chem. Phys. 123 (2005) 94705.

[30] D. Ragazzon, A. Schaefer, M.H. Farstad, L.E. Walle, P. Palmgren, A. Borg, P. Uvdal, A. Sandell, Surf. Sci. 617 (2013) 211.

[31] R. Nyholm, S. Svensson, J. Nordgren, A. Flodström, Nuclear Instruments and Methods in Physics Research A 246 (1986) 267.

[32] R. Nyholm, J.N. Andersen, U. Johansson, B.N. Jensen, I. Lindau, Nucl. Instrum. Meth. A 467 (2001) 520.

[33] D. Ragazzon, M.H. Farstad, A. Schaefer, L.E. Walle, P. Uvdal, A. Borg, A. Sandell, In manuscript (2014) .

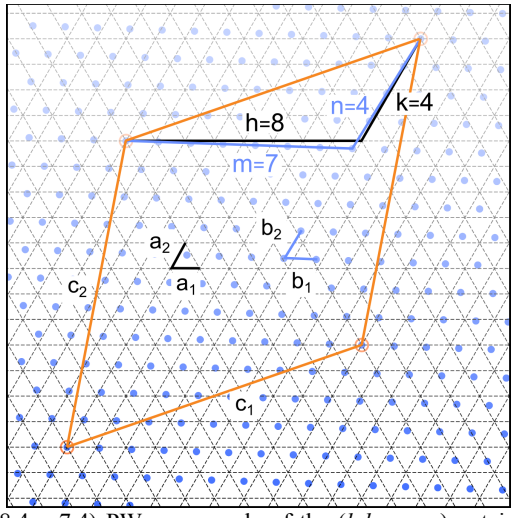

Figure 1. The (8,4 – 7,4) PW as example of the (*h*,*k* – *m*,*n*) notaion. The substrate lattice is shown with black dashed lines, the Ti lattice using blue dots. The base vectors of the substrate lattice ($\mathbf{a_1}$ and $\mathbf{a_2}$) are shown in black and the ones of the Ti lattice ($\mathbf{b_1}$ and $\mathbf{b_2}$) in blue. The coincidence between the lattice generates a Moiré superlattice ($\mathbf{c_1}$ and $\mathbf{c_2}$). The Moiré supercell is marked in orange. The figure illustrates how, in the case of the (8,4 – 7,4) PW, $\mathbf{c_1} = 8\ \mathbf{a_1} + 4\ \mathbf{a_2} = 7\ \mathbf{b_1} + 4\ \mathbf{b_2}$.

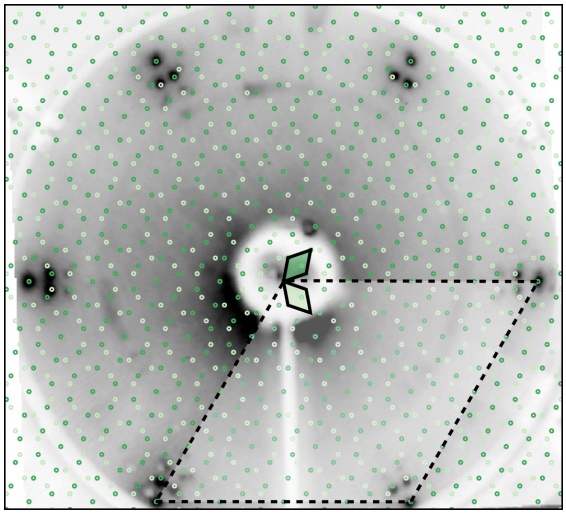

Figure 2. Image of the LEED pattern of the PW projected onto the reciprocal space. The reciprocal lattices of two symmetric domains of the (8,4 – 7,4) PW are shown with light and dark green circles. Their unit cells have also been mark in light and dark green, respectively. The reciprocal-space unit cell of the Au(111) is shown with a dashed line.

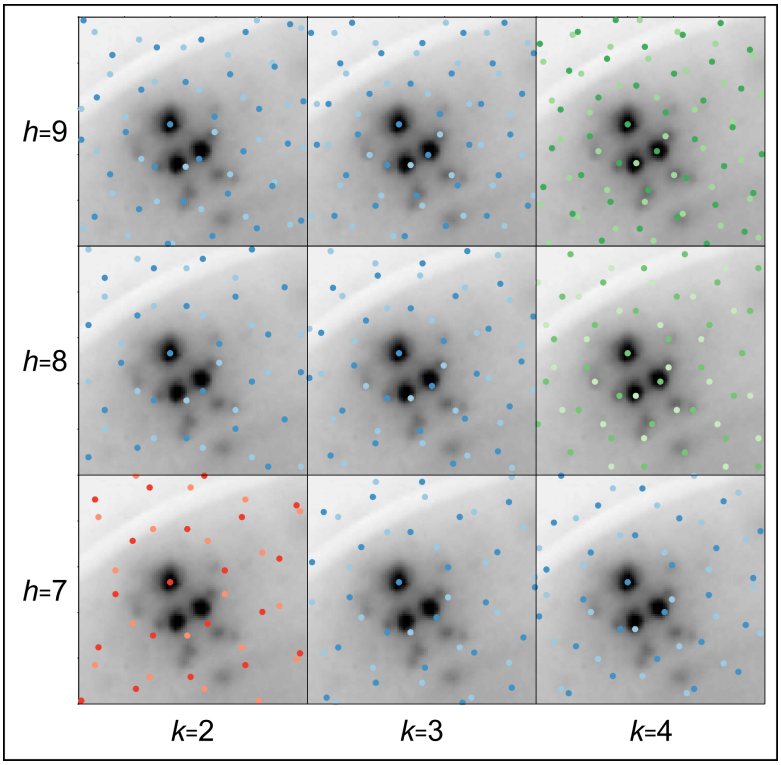

Figure 3. Detail of the experimental PW LEED pattern compared with the ones expected by several (*h*,*k* – *m*,*n*) structures. There is a good agreement with the ones of the (8,3 – *m*,*n*) and (9,4 – *m*,*n*) structures (green). The (7,2 – 6,2) PW reported in a previous work, would produce a LEED pattern (red) not compatible with the one presented here.

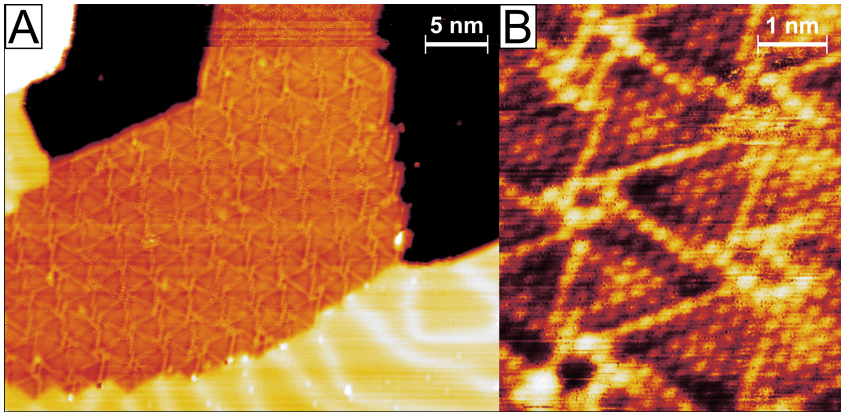

Figure 4. STM images of the PW. (a) PW island growing next to a Au(111) step. The surface of the island exhibits the characteristic pinwheel pattern. The island terminates with the "spokes" of the "wheel", suggesting that triangular unit are the stable building block constituting the PW. The herringbone reconstruction is visible on the Au terrace. (b) High-resolution image of the PW. The motif on the surface is the result of the different apparent height of atomic-sized round features. They were associated with Ti atoms. They look brighter along the spokes and around the hubs of the wheel.

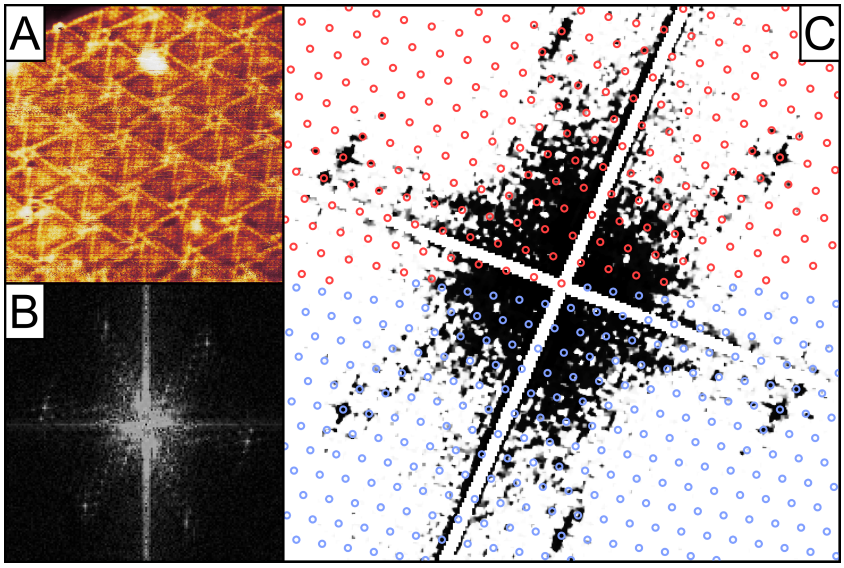

Figure 5. (a) 15 nm x 15 nm atomically-resolved image of the PW and (b) its Fourier transform. (c) The Fourier transform is compared to the pattern expected from a single domain of the (h,k – 7,4) (blue) and the (h,k – 7,3) (red) PW structures.

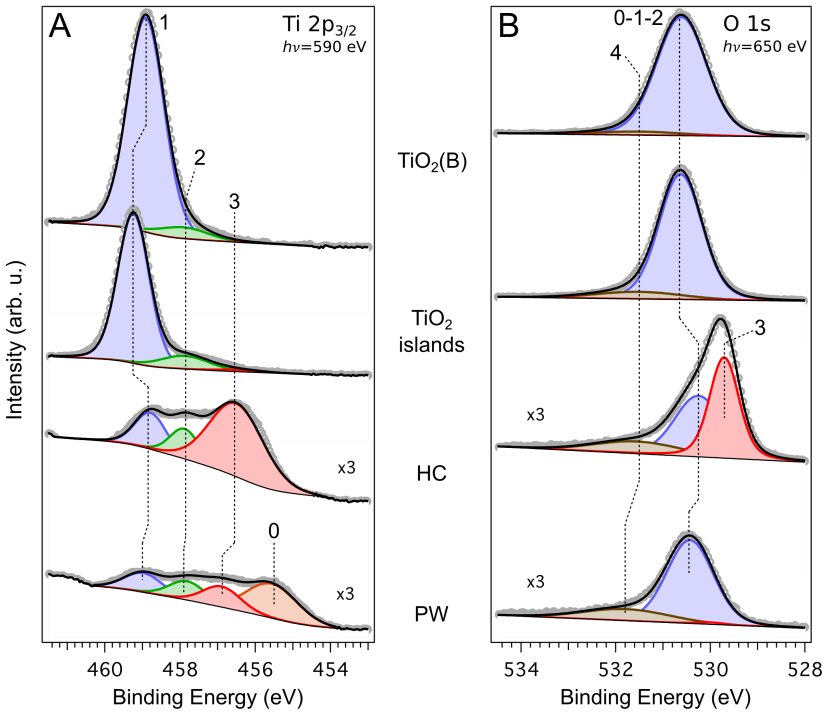

Figure 6. PES of the PW/Au(111). (a) Ti $2p_{3/2}$ and (b) O 1 s PES spectra and their components are shown for different TiO_x structures on Au(111). The PW spectra at the bottom of the figure were obtained by annealing the HC structure. Components "1" and "2" are associated with stoichiometric TiO_2 and its defects. Reduced titania presents components "0" and "1". Peak "3" disappears completely form the O 1s spectrum when the HC is converted into the PW upon annealing.

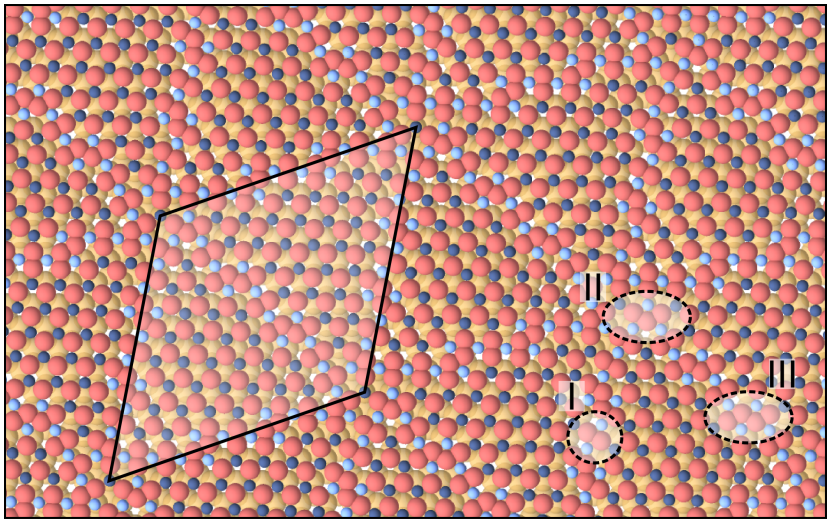

Figure 7. Model of the (8,4 – 7,4) PW on Au(111). O atoms have been included following the building principle in reference 21. The Moiré unit cell is indicated. Region I might be involved in the stress-releasing mechanism. Regions II and III present a high density of O atoms and presumably do not correspond to the actual structure of the PW. Areas in positions II and III are also the ones which appear more often irregular in the STM images.

Paper IV

Water adsorption on TiO_x thin films grown on Au(111)

M.H. Farstad, D. Ragazzon, L.E. Walle, A. Schaefer, A. Sandell, A. Borg

Submitted to The Journal of Physical Chemistry C

Water adsorption on TiO_x thin films grown on Au(111)

M. H. Farstad,[†] D. Ragazzon,[‡] L.E. Walle,[†] A. Schaefer,[¶] A. Sandell,[‡] and A. Borg[*,†]

Department of Physics, Norwegian University of Science and Technology, NO-7491 Trondheim, Norway, Department of Physics and Astronomy, Uppsala University, P. O. Box 530, SE-75121 Uppsala, Sweden, and Institute for Applied and Physical Chemistry & Center for Environmental Research and Sustainable Technology, University of Bremen, Leobener Str. UFT, D-28359 Bremen, Germany

E-mail: anne.borg@ntnu.no

Abstract

High resolution photoelectron spectroscopy has been used to investigate water adsorption on four different TiO_x thin film structures, grown on Au(111) by chemical vapor deposition. Two of the structures are reduced TiO_x single layer phases, forming a honeycomb and a pinwheel structure, respectively. The other two phases have TiO_2 stoichiometry, one in the form of islands and one in the form of a TiO_2 (B)(001) extended layer. Partial water dissociation is observed for all phases but the HC phase, and the dissociation propensity and adsorbate thermal stability strongly depend on the TiO_x structure. The dissociation on the PW and TiO_2 (B) structures is mainly related to different types of defect sites. Water dissociation on the PW layer stands out by leading to oxidation of Ti species. The TiO_2 islands, which closest resemble the rutile TiO_2 (110) surface in terms of hydroxyl thermal stability, generate the highest amount of hydroxyls and presents a structure dependent water dissociation mechanism.

Introduction

TiO_2 is a material with a wide range of applications, most of which rely on the special properties of the titania surfaces.[1] Examples are waste water remediation,[2–4] catalytic CO oxidation,[5] H_2 production[6] and as disinfectant agent.[7–9] For this reason, substantial efforts have been directed to the development of TiO_2 materials that expose as much surface area as possible. This has led to synthesis of various nanodimensional forms of TiO_2 and investigations of the novel properties that appear when reducing the size. Also mixed systems comprising TiO_2 exhibit useful surface chemical processes. For example, the border between TiO_2 and Au nanoclusters has been found to be catalytically active for CO oxidation[5,10] and for H_2 production from ethanol-water mixtures.[6] Underscoring the importance of having a TiO_2-Au boundary, activity towards the water-gas shift reaction is also found when Au is the substrate and nanostructures of TiO_2 are formed on top.[11] Thus, comparing the surface chemical properties of Au/TiO_2 with TiO_2/Au is expected to provide complementary understanding of the reaction mechanisms involved[12] and enable further tuning of the catalyst.

Commonly, the surface processes exploited for technological applications involve water, either as one of the main components, as solvent or as mediator.[13] A critical issue is the capability of the TiO_2 surface to dissociate water. Even when water dissociation is not a vital part in the reaction, H^+ and OH^- species may serve as charge carriers or oxidation agents improving the reaction rate.[2,10,13,14] Consequently, the interaction of water with the TiO_2 surfaces has been intensively studied and debated over the years. On the benchmark surface, rutile TiO_2 (110), it is by now well established that water dissociates on defect sites due to missing oxygen atoms.[15] The most recent experimental and theoretical efforts also show that partial water dissociation occurs on the stoichiometric TiO_2(110) surface.[16–21] In the process of characterizing new titania nanostructures, the ability to dissociate water is therefore an important feature to investigate and relate to results for TiO_2 single crystal surfaces.

In this work we address water adsorption on TiO_x nanostructures grown on Au(111) by Chemical Vapor Deposition (CVD). CVD is a very efficient and cost effective thin film deposition method. By changing the deposition parameters the resulting thin film or particle structure and thereby properties can be tailored. Previously we have reported on CVD using titanium(IV) isopropoxide (TTIP) as precursor for growing TiO_x thin film structures on Au(111).[22,23] By means of low energy electron diffraction (LEED), scanning tunneling microscopy (STM) and high resolution photoelectron spectroscopy (HRPES) the structure of four different TiO_x thin film phases on Au(111) were identified: Two phases consist of reduced wetting layers, which on the basis of STM images, form a honeycomb (HC) and a pinwheel (PW) structure, respectively.[22,24] The two other phases are fully oxidized, that is, with TiO_2 stoichiometry. One of these, labeled Star based on its LEED pattern, consists of islands which possibly exposes a reconstructed rutile TiO_2 (100) surface.[22] The other one is referred to as TiO_2(B) as it has been shown to consist of a TiO_2 (B)(001) structure.[23]

Here, we first present the most important characteristics of the four different TiO_x thin film phases on Au(111) grown by TTIP mediated CVD. Next, the adsorption and subsequent heating of water layers on the four phases are discussed on the basis of HRPES results. We observe water splitting on all phases except for the HC structure. Each of the other three phases displays different water dissociation mechanisms. The mechanism involved in the water dissociation are different for the three different phases.

Experimental

HRPES and STM experiments were conducted in separate chambers under ultra-high vacuum (UHV) conditions, at pressures in the low 10^{-10} mbar range. All chambers were equipped with LEED, ion gun and sample heating capabilities. The HRPES measurements were performed at the MAX IV Laboratory in Sweden, at beamline D1011 of the MAX II ring. This beam line is equipped with a modified Zeiss SX-700 monochromator and a Scienta SES200 electron analyzer.[25]The energy resolution at this beamline

is given by $E/dE = 1.5 \cdot 10^3 - 1.3 \cdot 10^3$.[26] HRPES data for both normal and grazing emission were recorded. Ti 2p spectra were measured using a photon energy of 590 eV, O 1s spectra were recorded at 650 eV and Au 4f spectra at 220 eV.

STM experiments were performed at room temperature in home laboratories at Uppsala University and the Norwegian University of Science and Technology. In both cases an Omicron Variable Temperature STM system was used and STM images recorded using tungsten tips.

As substrate for the TiO_x film growth an Au(111) crystal (Surface Preparation Laboratory) was used. The Au(111) surface was prepared by cycles of Ar-sputtering and annealing until no impurities were detected by HRPES, and LEED showed the herringbone reconstruction, indicating a clean and well ordered surface.

CVD was used for TiO_x film growth with TTIP (Sigma Aldrich, purity 99.999%) as precursor. The TTIP was kept in a glass tube connected to the vacuum chamber by a leak valve, and was dosed onto the sample through a stainless-steel tube which opening was positioned a few centimeters from the Au(111) surface. Dosing pressures ranged from $1 \cdot 10^{-9}$ mbar to $5 \cdot 10^{-8}$ mbar. Prior to deposition, the TTIP was thoroughly pumped and care was taken to avoid contamination by water.

The HC and Star TiO_x thin films were prepared by depositing TTIP at 300°C and 500°C, respectively. For depositions at 500°C the growth of the Star phase is predominant, but still a small initial growth of HC is observed. Similarly, HC is the predominant phase upon growth at 300°C, but disordered TiO_2 clusters are also formed. A detailed description of the growth as well as structural and chemical properties of these phases can be found in.[22] The PW wetting layer phase was formed by annealing the HC phase to 500°C.[24] The TiO_2(B) phase was prepared in two consecutive steps. First a thick layer of TiO_x was grown at 290°C, displaying only a faint 1x1 LEED pattern, then the disordered film was annealed to 500°C resulting in a film consisting of TiO_2(B)(001) domains with different orientations.[23]

The water experiments were performed by dosing 5 L D_2O through a leak valve, keeping the sample at about 90 K, followed by heating at the selected annealing temperature for 1 min, then cooling down again before measurements. This annealing procedure was performed in steps of increasing annealing temperature until no traces of water related species were detected on the surface. This sequence is referred to as a water annealing series. Although no difference in the water dissociation behavior for H_2O and D_2O was observed on Rutile (110) nor any beam induced dissociation,[21] D_2O has been used in these experiments in order to minimize the possibility of any beam induced water dissociation on the thin films studied.

Data Analysis

In the following, the procedure for analyzing the HRPES data is briefly described. The binding energy (BE) calibration of the HRPES spectra was performed by recording either the Fermi edge or the Au $4f_{7/2}$ peak when the Fermi edge was indiscernible, immediately after the core level region. A linear sum of Voigt or Doniach-Sunjic profiles was used for fitting the spectra. A Lorentzian FWHM of 0.15 eV was applied to all peaks. Unless otherwise stated, the spectra have been normalized on the low BE side.

Background subtraction for the O 1s spectrum was done by subtracting a modeled background obtained from the clean preparations. Above BE 533 eV a spectrum of the clean preparation was used to model the region below the water peak, below 532.5 eV the Shirley background of the O 1s peaks of the preparation was used. A Voigt lineshape was used for all O 1s peaks. The TiO_x film contributions have an asymmetry, which has been modeled by an extra peak at 1 eV higher BE than the main film contribution. The width of this peak was kept constant and the amplitude kept fixed at the same fraction of the main peak, as found from the clean preparation, throughout the water annealing series. Figure 1 shows an example of how the O 1s spectra recorded for the Star phase were fitted. The spectrum was recorded after a dose of 5 L D_2O at 90 K followed by heating to 200 K. The peaks around 531 eV originates from the TiO_2 phase and the peaks at 532 eV and 534 eV correspond to hydroxyls and molecular water, respectively.

For the Ti $2p_{3/2}$ spectra a normal Shirley back-

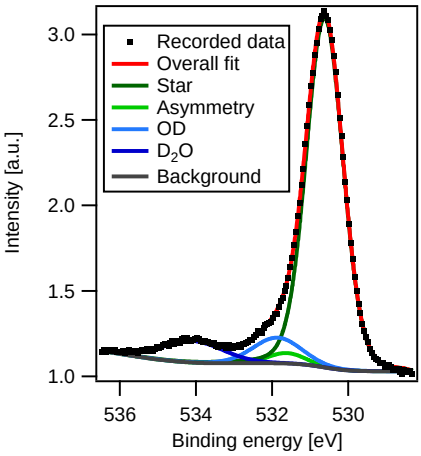

Figure 1: Fitted O 1s spectrum for the Star preparation using a modeled background, and four Voigt lineshape peaks, two peaks from the as prepared phase, Star and asymmetry, and two water related peaks, OD and D_2O. This spectrum was recorded after the 200 K annealing step.

ground subtraction has been applied. Voigt lineshapes were used for all peaks except for the peak at 455.5 eV originating from the PW phase where a convolution of an asymmetric Doniach-Sunjic and Gaussian lineshape was used.

The Au 4f surface contribution has been used to determine the total coverage of the preparations, and Ti $2p_{3/2}$ peaks have been used to obtain the partial coverages of the mixed phases. In order to determine the monolayer (ML) coverages of water and hydroxyls both O 1s and valence band spectra have been used.

Results

The clean TiO_xpreparations

Representative STM images of the four different thin film TiO_x phases grown on Au(111) are displayed in Figure 2. The TiO_2(B) phase, seen in Figure 2a, consists of domains which have merged to form a sheet covering the Au(111) surface almost completely. The domains are separated by clear domain boundaries and occasional holes or openings. The interior of the domains exhibit only a few defects. STM and LEED results reveal an atomic structure of the domains consistent with TiO_2 (B)(001).[23] There are two possible terminations for this surface, one that exposes two types of 5-fold coordinated Ti ions (type I) and one in which half of the Ti ions in the topmost layer are bonded to oxygen atoms, forming titanyl groups (type II). The STM images suggest that the termination is of type I, in accordance with theoretical predictions that this is the favored termination in vacuum.[27] Moreover, on the basis of the attenuation of the Au 4f photoemission signal, we estimate that the film needs to be at least three layers thick for the TiO_2(B) phase to form.[23]

Figure 2b shows a STM image recorded of the Star phase similar to the preparation used for the water annealing series. The Star phase consists of TiO_2 islands evenly distributed on the Au(111) surface. Images with higher resolution[22] are in close resemblance to images obtained for a phase grown on Pt(111) identified as a quasi (2x1) rutile TiO_2(100) surface featuring an additional (7x1) reconstruction.[28] However, the STM and LEED results for the Star phase on Au(111) indicate an (8x1) reconstruction.[22] A possible reconstruction of the rutile TiO_2(100) surface has been found to consist of micro-facets of the rutile (110) surface.[29] Even if the exact atomic structure of the Star phase is not known it appears clear that the surface has a certain corrugation with ridges separated by approximately 25 Å.[22]

The HC phase is a flat, homogeneous single layer with the honeycomb pattern clearly observed by STM, as displayed in Figure 2c. This phase is always accompanied by clusters of oxidized TiO_2 islands. The HC islands are large, up to several tens of nanometers wide, and practically no defects are observed within the HC structure. The other wetting layer, the PW phase, shown in Figure 2d, has a more compact structure, which in the STM images resembles a pinwheel pattern with six spokes. Along the spokes and in the hub of the pinwheels there are dislocation sites resulting in larger variation in the electronic structure.[24] Also this phase forms islands that are up to several tens of nanometers wide.

The predominant TiO_x phase can be determined with LEED by virtue of having a distinctive

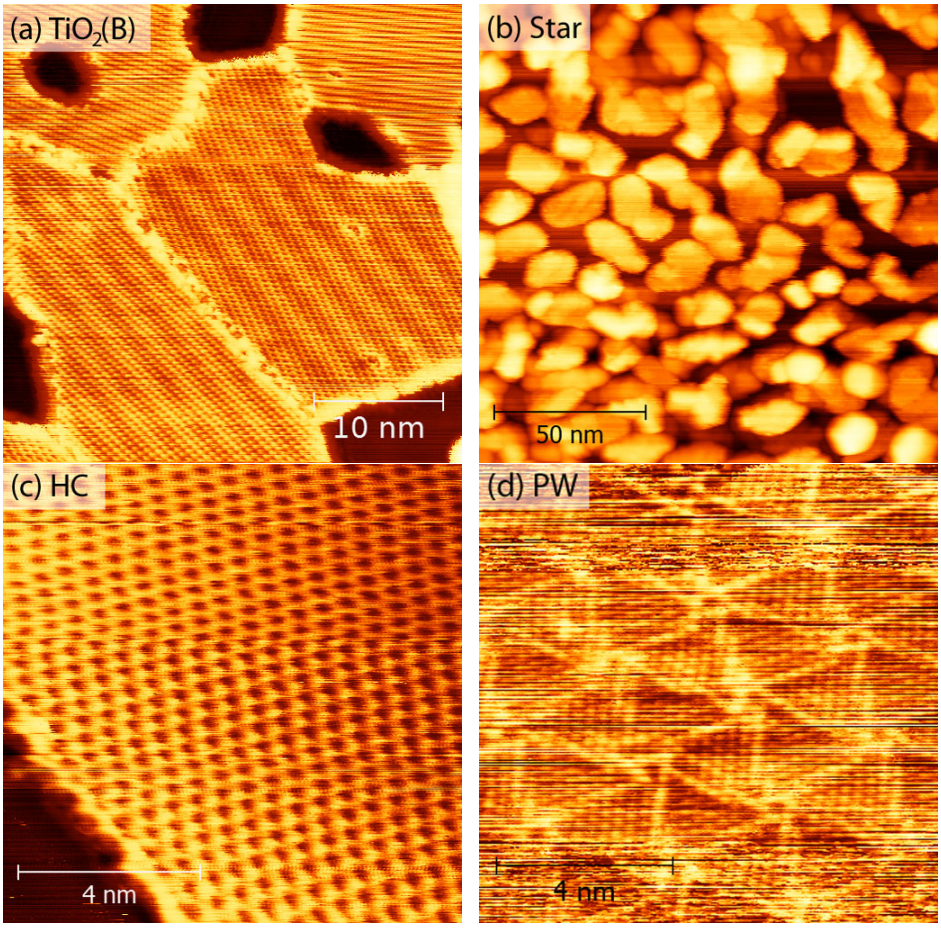

Figure 2: STM images of the four different TiO_x phases grown on Au(111). (a) Domains of the TiO_2(B) phase, separated by disordered domain boundaries and holes. The domains themselves have very few defects. (b) Star islands distributed on the Au(111) surface. (c) The honeycomb pattern of the HC phase, and (d) the structure of the PW phase.

diffraction pattern, but to get a more complete picture of each preparation HRPES spectra are imperative. The Ti 2p spectra for the four different preparations used in the water annealing series are displayed in Figure 3.

The two topmost spectra show the Ti 2p spectra of the TiO_2(B) and Star preparations, respectively. In both cases, a peak at BE 459 eV dominates. This state, labeled A, corresponds to Ti^{4+} species in accordance with these phases consisting of TiO_2. In addition to peak A, there is also a small contribution at 457.5 eV, labeled B. This peak lies within the BE region which is reported for Ti^{3+}, 455.6 eV - 458.1 eV,[30] and has been found to be connected to defects in fully oxidized phases.[22] The TiO_2(B) preparation covers 94% of the Au(111) surface and the Star preparation covers 67%.

The third spectrum in Figure 3 is the one recorded for the HC preparation. The peak at BE 456.3 eV, labeled C, is characteristic for the HC phase.[22] The BE falls within the regime of Ti^{3+}, which is in accordance with the HC phase having Ti_2O_3 stoichiometry.[22,30] Also the binding energy of the O 1s peak for this phase is different from the other phases, 529.4 eV compared to 530.5 eV. In addition, there are contributions from peaks A and B in the Ti $2p_{3/2}$ spectrum. These are assigned to TiO_2 clusters with associated defects. Overall, this preparation covers 37% of the Au(111) surface, of which 79% is HC phase and 21% TiO_2 clusters.

At the bottom in Figure 3 the Ti 2p spectrum for the PW preparation is shown. This phase is characterized by a peak at BE 455.5 eV, labeled D, in good agreement with the existence of Ti^{2+} species.[23,30] As for the HC preparation, TiO_2 clusters are also present, giving rise to contributions from peaks A and B. There is no evidence for the HC phase coexisting with the PW phase, which is expected given that the HC phase transforms to the PW phase upon annealing. The PW preparation covers 25% of the Au(111) surface, of which 92% is the PW phase itself and the remaining 8% is TiO_2 clusters.

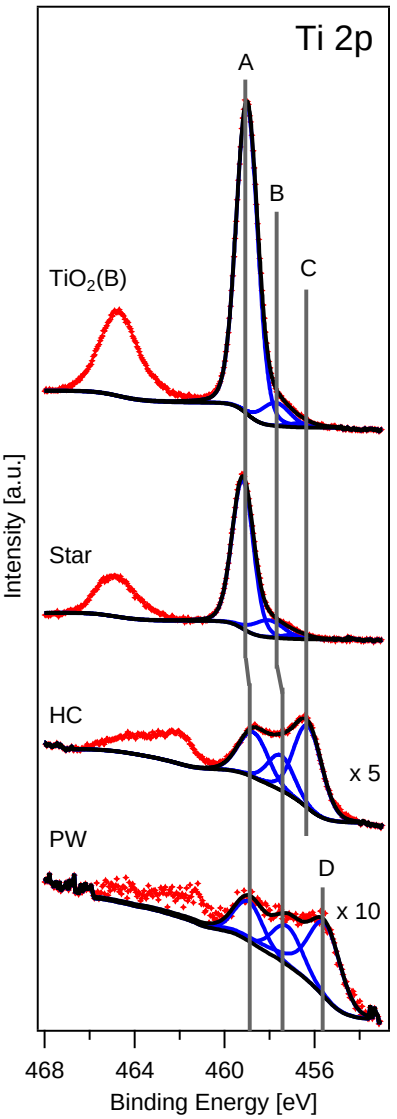

Figure 3: Ti 2p spectra for the four TiO_x thin films, as prepared. The spectra for the HC and PW phases are multiplied by a factor 5 and 10 respectively. Only the Ti $2p_{3/2}$ components have been fitted, they are labeled A, B, C and D.

Water adsorption and desorption

When 5 L D_2O is deposited at 90 K on the TiO_x/Au(111) surfaces, a thick multilayer of wa-

ter (i.e. ice) is formed, covering the entire surface including the clean Au(111) areas. By heating the sample above 160 K, the water on the clean Au(111) surface areas desorbs, leaving water only on the TiO_x phases. Thus, it is possible to selectively study the water interaction with the TiO_x phases at 170 K and above. Water annealing series were carried out for the four different TiO_x preparations, and for each temperature step in the series O 1s spectra were recorded. In Figure 4 the results of the annealing series are illustrated by fitted spectra recorded after annealing to 180 K, 220 K, 300 K and 500 K or 400 K. The modeled background was subtracted before the spectra were normalized in peak height to aid visual comparison. For TiO_2(B) preparations, generally consisting of several layers, the spectra were recorded using grazing emission (GE) in order to enhance surface sensitivity and hence the water induced contributions. For the other preparations, normal emission (NE) was chosen to maximize the count rate.

Molecular water is associated with an O 1s peak at a BE of 534 eV, while the O 1s peak due to hydroxyl contributions appears at a BE of 532 eV. As seen in Figure 4, both water and hydroxyls are present on all four preparations and both species gradually disappear with increasing temperature. In order to make a quantitative comparison between the different phases, the coverages of water and hydroxyls have been determined. The results are compared to a rutile TiO_2(110) surface, prepared to obtain a ideal, defect free stoichiometric surface.[17,31] On TiO_2 surfaces it is common to define an adsorbate coverage relative to the number of Ti atoms in the surface layer. For example, one ML on rutile TiO_2(110) corresponds to the density of fivefold-coordinated Ti-sites on the surface, which amounts to 5.2 x 10^{14} cm^{-2}. The Ti densities used for the coverage estimates in the present work are summarized in Table 1. For the TiO_2(B) phase the value for the TiO_2(B)(001) surface of type I termination was used. In the case of the Star phase, where the exact atomic structure is unknown, two estimates have been made: one that relates the adsorbate density to the unreconstructed rutile TiO_2(100) surface, Star(100), and one related to the rutile TiO_2(110) surface, Star(110). The reason for this choice is that the Star phase is assumed to be surface reconstructed rutile TiO_2(100), and this reconstruction can occur by formation of rutile TiO_2(110) facets.[29] The results of the coverage estimates are presented in Figure 5, subdivided into D_2O and OD coverages on fully oxidized TiO_2 phases and reduced phases, TiO_x, $x < 2$. The D_2O and OD coverages on rutile TiO_2 (110) are taken from ref.[32]

Table 1: Density of surface Ti sites for selected TiO_x structures.

Structure	Ti density [10^{14} cm^{-2}]
TiO_2 (B)(001), type I	8.70
Unreconstructed TiO_2(100), Star(100)	7.34
Rutile TiO_2 (110), Star(110)	5.20
HC	7.10
PW	10.80

Summarizing the results for the reference surface, rutile TiO_2(110), the first layer comprises about 0.8 ML D_2O and 0.4 ML OD. This corresponds to adsorption of 1 ML water as one water dissociation event yields two hydroxyls.[33] The molecular water within the first layer desorbs between 210 K and 300 K. Desorption of hydroxyls (by recombination) overlaps to a large extent with desorption of molecular species and the last remainder of hydroxyls desorbs between 300 and 400 K.

Fully oxidized phases

Water interacts weakly with the TiO_2(B) phase. At 170 K, the lowest temperature at which we selectively probe water on the TiO_2(B) phase, the D_2O coverage amounts to 0.5 ML. Assuming that the interaction is strongest with Ti, implies that 50% of the Ti ions are coordinated to D_2O molecules at this point. The coverage drops to 0.2 ML at 180 K after which further desorption is slow. The last D_2O has desorbed after annealing to 300 K. Thus, there are D_2O molecules with similar bonding strength as on rutile (110) but these represent minority species. A small degree of water dissociation is observed for the TiO_2(B) phase. The maximum OD coverage is 0.1 ML implying that 0.05 ML D_2O dissociates on the surface of the

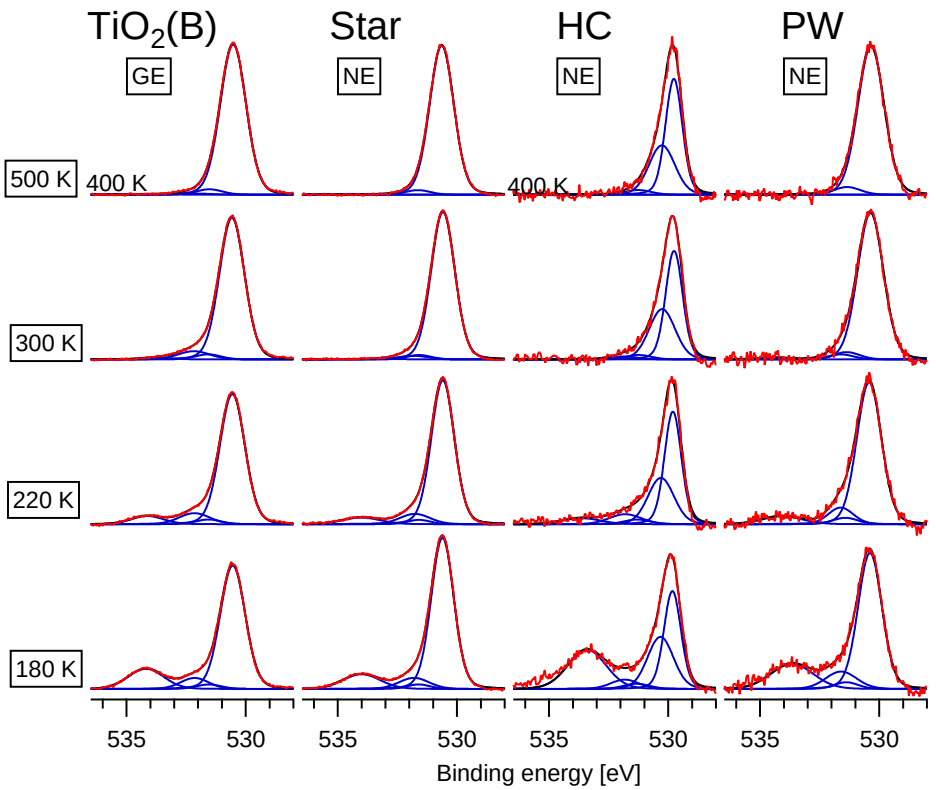

Figure 4: O 1s spectra from the water annealing series for all four preparations. The spectra were recorded using grazing emission (GE) for the TiO_2(B) phase, while normal emission (NE) was used for the other phases. The background has been subtracted and the spectra have been normalized to the thin film peak height of the 500 K (400 K) annealing step spectra for each preparation.

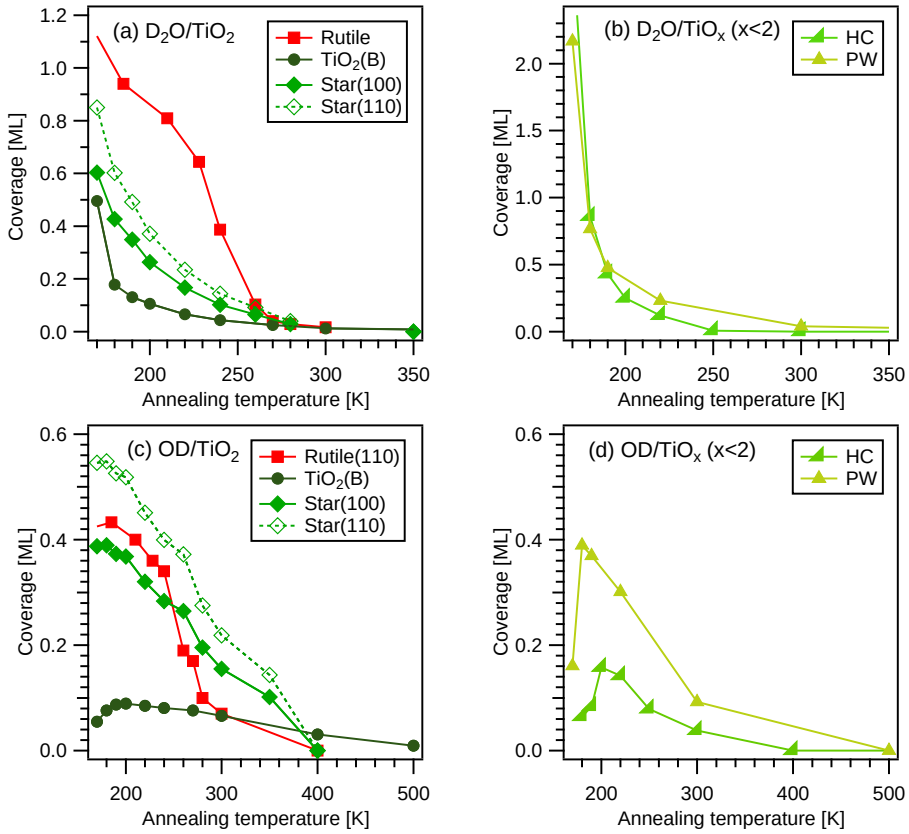

Figure 5: (a) Molecular water and (c) hydroxyl coverage as function of annealing temperature for the fully oxidized phases along with the corresponding results for stoichiometric rutile $TiO_2(110)$.[32] (b) Molecular water and (d) hydroxyls as function of annealing temperature for the reduced HC and PW phases.

TiO_2(B) phase. This in turn suggests that only about 5% of the Ti sites are active towards dissociation. Still, the hydroxyls that form on the TiO_2(B) preparation are comparatively stable; 40% of the maximum amount remains at 400 K and an annealing to 500 K is required to completely remove the hydroxyls.

On the Star surface, the water coverage at 170 K is estimated to 0.75 ± 0.15 ML, with the uncertainties given by the different Ti densities considered. The coverage decreases continuously with increasing temperature and the last D_2O species desorb at 280 - 300 K. At every temperature, the D_2O coverage is significantly lower than the coverage measured on the rutile (110) surface, indicating a weaker D_2O-TiO_2 interaction for the Star phase. The OD coverage for the Star phase is 0.47 ± 0.08 ML at 170 K. Up to 200 K only a small decrease in the OD coverage is observed, after which it decreases progressively with increasing annealing temperature. The last hydroxyls desorb between 350 and 400 K. The average OD coverage on the Star phase is observed to be comparable to the amount of hydroxyls present on the rutile (110) surface up to 250 K. However, above 250 K the OD coverage on the Star islands is higher.

Reduced phases

The HC preparation consists of a combination of areas with pure HC phase and TiO_2 clusters. The O 1s spectra shown in Figure 4 include the contributions from both phases. Since the Star preparation is a pure phase with TiO_2 islands only, those results can be used to estimate the contribution from clusters for the HC preparation. Consequently, the D_2O and OD coverages shown in Figures 5b and 5d are those obtained after subtraction of the estimated contribution from TiO_2 clusters covering 8% of the Au(111) surface and should therefore represent an estimate of the coverages solely associated with the HC phase. At 170 K, it is clear that a water multilayer is still stable on the HC structure. Increasing the temperature to 180 K leaves about 0.9 ML D_2O. A continuous decrease in coverage is noted for higher temperatures and all D_2O is desorbed by 250 K. Only a small amount of hydroxyls are observed on the HC phase, a maximum coverage of about 0.15 ML is observed at 200 K. Half of the OD species has desorbed at 250 K and the last OD desorbs between 300 and 400 K. Thus, the thermal stability of the OD species is comparable to that on the rutile (110) surface.

Also the investigated PW thin film represents a mixed preparation. Similar to the HC case the amount of water and hydroxyls on the PW phase has therefore been obtained after first subtracting the contribution associated with TiO_2 clusters covering 2% of the Au(111) surface. The fractions of water and hydroxyls associated with the PW structure are displayed in Figures 5b and 5d. The behavior of D_2O is very similar to that found for the HC phase; multilayer formation occurs $\leq$170 K and about 0.8 ML D_2O is observed upon heating to 180 K. There is a limited number of data points in this series, but the last D_2O is likely to desorb around 300 K as there is only a very small amount left at this point. The maximum amount of hydroxyls is just below 0.4 ML, observed at 180 K. This is considerably higher coverage than observed for the HC phase. About 0.1 ML OD remains at 300 K, making the hydroxyl stability similar to that found for the rutile (110) surface.

The origin of the dip in the OD coverage found below 200 K for both the reduced phases and the TiO_2(B) phase is uncertain. One possibility is attenuation of the signal from OD species due to formation of 3D D_2O-OD complexes, another possibility is a heating induced dissociation between 180 and 200 K.

Water induced effects on the TiO_x films

The effect of a water adsorption/desorption cycle on the four different TiO_x preparations has also been investigated. No changes were observed in any of the LEED patterns after the water annealing series, indicating that the overall structures remain unaltered. However, monitoring the oxidation state of Ti provides evidence for changes occurring during water exposure. This is shown for the HC preparation in Figure 6. Before the water treatment the peak due to the HC phase, peak C, is clearly dominating the Ti $2p_{3/2}$ spectrum (shown in green). After water adsorption and annealing to 160 K this contribution is reduced and has a spectral weight which is comparable to peak A, which

in turn is only slightly damped. After annealing to 400 K all D_2O and OD species have desorbed but the spectrum differs from that of the pristine film in that intensity has been redistributed towards the high BE side. That is, a certain degree of oxidation has taken place. However, curve fitting indicates that the intensity of peak C is essentially unchanged compared to that of the pristine film and that the effect is rather described by a shift of intensity from peak B to peak A. This means that the HC phase itself is not affected by water while a change in the properties of the coexisting clusters appear as a decrease in the contribution from defects. The intensity changes of the Ti $2p_{3/2}$ peak components for all four preparations are summarized in Table 2. The results for the two fully oxidized phases, TiO_2(B) and Star, show a similar tendency for loss in the intensity from defect states but the changes are less accurately determined due to the lower relative intensities. For the PW phase, however, oxidation upon water interaction is evident through pronounced reduction in the intensity of peak D.

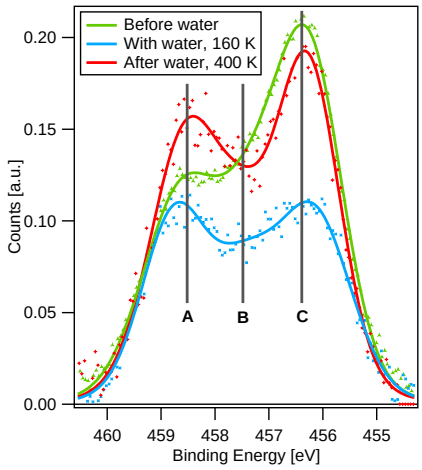

Figure 6: Ti $2p_{3/2}$ spectra of the HC phase as prepared, after water adsorption and subsequent annealing to 160 K and after water desorption at 400 K.

Table 2: Changes in peak intensities of the Ti $2p_{3/2}$ contributions after water adsorption and subsequent heating to 500 K (400 K) relative to the total intensity of the as prepared film phases. HC and Star are annealed to 400 K.

Preparation	Peak A	Peak B	Peak C / D
HC	12%	-9%	-3%
PW	12%	4%	-16%
Star	5%	-4%	-1%
TiO_2(B)	3%	-3%	-0%

Discussion

Fully oxidized phases

On the TiO_2(B) phase a low amount of hydroxyls (<0.1 ML), which persists up to 500 K is observed. Under the assumption of primary adsorption on Ti sites, formation of 0.1 ML hydroxyls implies that about 5% of the Ti sites are active towards dissociation. Hydroxyls formed at bridging oxygen vacancies on rutile TiO_2(110) show a similar thermal stability as they recombine and desorb at 490 K.[15,34] The thermal stability and low amount observed for the TiO_2(B) preparation thus suggests that the dissociation is associated with defect sites. Oxygen vacancies on rutile (110) are associated with the presence of Ti^{3+} states. The Ti^{3+} component, peak B, seen in the Ti 2p spectrum of the TiO_2(B) preparation (Figure 3) can therefore be used as a measure of the defect density. The relative intensity of the Ti^{3+} state is 10% in NE and 6% in GE, indicating that more Ti^{3+} ions are located below the surface than in the surface layer. A possible explanation is that the Ti^{3+} species are predominantly located at the domain boundaries and possibly also at the TiO_2-Au(111) interface. Judging from the STM images the estimated relative surface area of boundary lines, point defects and edges constitutes about 15% of the TiO_2(B) film. Some of these defects are expected to feature surface Ti^{3+} sites. Low amounts (0.1 ML) of D_2O persist on this surface in a rather wide temperature range, 200-270 K. It is plausible that these D_2O species are associated with imperfections of the TiO_2(B) preparation. From this follows that only about 15% of the Ti sites carry adsorbed species (D_2O and OD) above 200 K, an amount in good

agreement with the abundance of defect sites. The interaction of water with the TiO_2(B) phase itself is thus very weak, featuring only molecular adsorption. This conclusion is in good agreement with theoretical predictions, where the water interaction with the Type I termination of TiO_2(B)(001) was found to be weak with no tendency for dissociation.[27]

Water on TiO_2(B)(001) grown on Pt(111) has recently been investigated by Artiglia et al.[35] They report on a small amount of water dissociation where the hydroxyls leave the surface before 400 K. This finding is connected to the report of no surface Ti^{3+} species, excluding Ti^{3+} sites as active sites for the dissociation.[34] Instead edge sites are suggested to be active in dissociating water.[35] Compared to TiO_2(B) on Au(111) the desorption temperature is the most prominent difference, as hydroxyls are present on the surface up to 500 K for TiO_2(B) on Au(111) compared to 400 K for TiO_2(B) on Pt(111). One possible explanation for this difference lies in the morphology of the preparations. Even though TiO_2(B) forms on both Pt(111) and Au(111) the morphology is different. On Pt(111) TiO_2(B) grows on top of a reduced TiO_x wetting layer and exhibits a tendency to form 3D islands. Due to the underlying TiO_x wetting layer, the Ti^{3+} contribution seen in the Ti 2p PES spectrum is much larger (20-25%) than for the TiO_2(B) phase on Au(111). Judging from the STM images,[35] about 50% of the surface is covered by TiO_2(B)(001) islands after deposition of 4 ML(eq). On Au(111) about 90% of the surface is covered already after 3 ML(eq). TiO_2(B) on Au(111) wets the surface more efficiently, leading to merging of islands and formation of a predominantly continuous film with domain boundaries. Still, the domain sizes are comparable in the two cases. It is likely that the behavior of water at domain boundaries is different from the behavior at the edges of islands, providing an explanation for the observed difference in desorption temperature.

The structure associated with the Star preparation has previously been proposed to be similar to the rutile (100) surface, albeit with a surface reconstruction, (7x1) on Pt(111)[28] and (8x1) on Au(111).[22] A suitable starting point is therefore to compare the results for water on the Star phase with those for water on rutile (100). In a previous TPD study of H_2O/TiO_2(100)-(1x1),[34] the first layer was found to desorb between 170 K and about 400 K. Three desorption maxima were discerned, appearing at 205 K, 290 K and 305 K. It was argued that only molecularly adsorbed water desorbs up to 290 K while desorption above 290 K is associated with recombinative desorption of dissociated water.[34] This is in accordance with a valence PES study, which shows that there is no H_2O left on the TiO_2(100) surface above 290 K, only OH.[36] In the TPD study, uptake was limited to 1 ML at 170 K and it was estimated that about 50% of the water in the first layer had dissociated.[34]

On the Star preparation, all D_2O has desorbed at 300 K, implying that only OD desorb between 300 K and 400 K. No desorption is found above 400 K. These results are in agreement with the TPD and PES studies for TiO_2(100).[34,36] However, we also observe a significant loss of OD already between 200-300 K, where the OD coverage decreases from about 0.44 ML to 0.19 ML. Thus, there is an overlap between recombinative desorption of hydroxyls and desorption of molecular D_2O. This behavior is similar to that found for H_2O deposited on rutile TiO_2(110).[17]

From Figures 5a and 5c the D_2O-OD speciation for the Star preparation can be inferred. If the Ti surface density is assumed to be close to that of the rutile TiO_2 (110) surface, labeled Star(110) in Table 1, and use that one water molecule creates two hydroxyls upon dissociation, it follows that the surface coverage is 1.125ML at 170 K with 24% of the water molecules being dissociated and it is 0.88 ML at 180K of which 31% is dissociated. From this follows that the ML point is located between 170 and 180 K and about 27% of the first layer water dissociates at this point. Choosing the surface density of the unreconstructed TiO_2(100) surface, Star(100), gives a ML point below 170 K and a slightly lower amount of hydroxyls formed. In comparison with the results reported for the rutile TiO_2(100)-(1x1) surface, the temperature of the ML point is similar while the degree of dissociation is lower. In the TPD study by Henderson et al.,[34] uptake is limited to 1 ML at 170 K and it was estimated that about 50% of the water in the first layer had dissociated. On rutile TiO_2 (110), the ML point is located at 210 K at which 20% dissociation is found.[17] This degree of dissocia-

tion is only slightly lower than that found for the Star phase. From this it can be concluded that the behavior of water on the Star phase can be well described in terms of a superposition of the behaviors found on the rutile TiO_2 (100) and (110) surfaces. Therefore, the results are consistent with the concept of an (nx1) surface reconstruction of rutile (100) into (110) facets. Similar findings have also been reported for TiO_2 (100) structures on Pt(111).[35] In this case, a dissociation degree of 30% was reported. The finding of a value below 50% would then be consistent with the notion of a reconstructed surface, which indeed was found to be the case also for the film grown on Pt(111).

The effect of defects should also be considered. The Ti^{3+} contribution seen in Figure 3 for this Star preparation has a relative intensity of about 15%. The location of the defects is unknown, but the many small islands, which the Star phase consists of, provide a large amount of rim between Au(111) and TiO_x, which represents possible dissociation sites. From Table 2 it is clear that some of the Ti^{3+} defects are oxidized. However, this is a very small effect compared to the observed amount of hydroxyls for the Star preparation, and the defects are therefore not likely to play a key role in the observed water dissociation.

Reduced phases

For the HC preparation a maximum OD coverage of 0.15 ML is found. Assuming adsorption on Ti ions only, the OD coverage indicates that 8% of the Ti sites are active for dissociation. The HC phase forms a (2x2) superstructure on the Au(111) surface. If the dissociation was an inherent property of the HC phase itself the observed dissociation degree corresponds to one dissociation event per six (2x2) unit cells. Although such a OD-D_2O structure cannot be completely ruled out, it appears more likely that this small amount of hydroxyls is rather due to defects or uncertainty in the subtraction procedure undertaken to eliminate the contribution from TiO_2 clusters. Peak B is much larger compared to peak A for the HC preparation than for the Star preparation, see Figure 3, indicating that there are more defects associated with the clusters in the HC preparation. This may be caused by the lower deposition temperature of 300°C used for the HC preparation compared to the Star preparation, formed at 500°C. These extra defects may account for the remaining hydroxyls. Other possible sites for hydroxyl formation on this structure are sites along the boundary between the HC phase and the TiO_2 clusters. The changes in the Ti 2p spectra, listed in Table 2, indicate that it is the defects represented by peak B which interacts with the water species and are therefore likely to cause the observed hydroxyls. This supports the notion of the dissociation being related to TiO_2 clusters rather than the HC phase. Further support for this conjecture is the finding that no hydroxyls are left on the surface after annealing to 400 K, which makes the thermal stability of the hydroxyls observed for the HC preparation comparable to that of the Star phase, but different from both the TiO_2(B) phase and the bridging oxygen vacancies on rutile (110). This leads to the conclusion that the HC phase itself does not dissociate water, and the observed hydroxyls are attributed to the high defect contribution in the coexisting Star clusters of this preparation.

The water ML point for the PW phase is observed at about 180 K, with the composition 0.8 ML D_2O and 0.4 ML OD. Although there is a limited number of data points the thermal stability of the D_2O and OD species is quite comparable to the rutile (110) surface. Hence, the partial dissociation may be an inherent property of the PW structure itself. The STM images reveal a clear contrast between the Ti ions within the structure. Judging from the STM image shown in Figure 2d the spokes and hubs of the PW phase make up 20-30% of the phase, in reasonable correspondence with the amount of hydroxyls observed. This finding indicates that these bright features may serve as active sites for water dissociation on the PW phase. For this phase some oxidation occurs upon water adsorption and desorption. The decrease in the Ti 2p peak intensity is about 16%. This number compares well to the number of active Ti sites for dissociation, which is 20% based on the formation of 0.4 ML OD. It can therefore not be excluded that the dissociation process is related to the oxidation process. However, the particular nature of the oxidation process is not fully understood, one possibility may be abstraction of H_2.

The different behavior of the four different TiO_x

thin film phases on Au(111) towards water dissociation and thermal stability of D_2O and OD species makes these systems highly interesting for model reactions involving water. For example, in the water-gas shift reaction water dissociation is an important step which for many catalysts is the rate determining step.[37] A system which dissociates water is therefore a strong candidate as catalyst for this reaction. TiO_x nanoparticles on Au(111) have already been shown to catalyze the water-gas shift reaction.[11] The possibility to experiment with different dissociation mechanisms, oxidation states and perimeters may further the understanding of this reaction.

Conclusions

Water adsorption and desorption on four different TiO_x thin film structures on Au(111) have been reported. Water splitting was found on three of these phases. The mechanism involved in dissociating water is different for the different phases, thus it is clear that the structure is of outermost importance for the dissociation activity. The Star phase is the most efficient phase for hydroxyl formation with an amount of hydroxyls formed comparable to that observed on the rutile(110) surface. Furthermore it presents a structure dependent water dissociation mechanism. In addition, possible defects in this island structure may contribute to the amount of hydroxyls formed. The TiO_2(B) phase yields hydroxyl formation through defects such as domain boundaries, point defects and edge sites, whereas the PW phase provides reduced Ti sites available for water dissociation. Finally, the HC phase appears inactive in splitting water. The possibility to mix different TiO_x phases with different dissociation mechanisms could provide interesting model systems for tailoring catalysts for various reactions.

Acknowledgement Financial support was received from the Swedish Energy Agency (STEM), the Swedish Science Council (VR), the Trygger foundation, the Crafoord foundation, NordForsk and the Göran Gustafsson foundation. D.R. has been supported by the Anna Maria Lundins scholarship from Smålands Nation in Uppsala and L.E.W. has been supported through the Strategic Area Materials at NTNU. We thank the staff at MAX-lab for their support.

References

(1) Diebold, U. *Appl. Phys. A* **2003**, *76*, 681–687.

(2) Konstantyinou, I.; Albanis, T. *A Rev. App. Catal. B Environ.* **2004**, *49*, 1–14.

(3) Habibi, M.; Vosooghian, H. *J. Photochem. Photobiol. A Chem.* **2005**, *174*, 45–52.

(4) Maldonado, A. *Phys. Status Solidi C* **2010**, *7*, 2316–2320.

(5) Valden, M.; Pak, S.; Lai, X.; Goodman, D. *Catal. Letters* **1998**, *56*, 7–10.

(6) Jovic, V.; Chen, W.; Sun-Waterhouse, D. *J. Catal.* **2013**, *305*, 307–317.

(7) Maness, P.; Smolinski, S. *Appl. Environ. Microbiol.* **1999**, *65*, 4094–4098.

(8) Blake, D.; Maness, P. *Sep. Purif. Rev.* **1999**, *28*, 1–50.

(9) McCullagh, C.; Robertson, J. *Res. Chem. Intermed.* **2007**, *33*, 359–375.

(10) Gao, F.; Wood, T.; Goodman, D. *Catal. Letters* **2010**, *134*, 9–12.

(11) Rodriguez, J. A.; Ma, S.; Liu, P.; Evans, J.; Perez, M.; Hrbek, J. *Science* **2007**, *318*, 1757–1760.

(12) Rodríguez, J.; Hrbek, J. *Surf. Sci.* **2010**, *604*, 241–244.

(13) Farnesi Camellone, M.; Marx, D. *J. Phys. Chem. Lett.* **2013**, *4*, 514–518.

(14) Henderson, M. A. *Surf. Sci. Rep.* **2011**, *66*, 185–297.

(15) Pang, C. L.; Lindsay, R.; Thornton, G. *Chem. Soc. Rev.* **2008**, *37*, 2328–2353.

(16) Oviedo, J.; Sánchez-de Armas, R.; San Miguel, M. A.; Sanz, J. F. *J. Phys. Chem. C* **2008**, *112*, 17737–17740.

(17) Walle, L.; Borg, A.; Uvdal, P.; Sandell, A. *Phys. Rev. B* **2009**, *80*, 235436.

(18) Sebbari, K.; Domain, C.; Roques, J.; Perron, H.; Simoni, E.; Catalette, H. *Surf. Sci.* **2011**, *605*, 1275–1280.

(19) Duncan, D. A.; Allegretti, F.; Woodruff, D. P. *Phys. Rev. B* **2012**, *86*, 045411.

(20) Patel, M.; Mallia, G.; Liborio, L.; Harrison, N. M. *Phys. Rev. B* **2012**, *86*, 045302.

(21) Amft, M.; Walle, L. E. L.; Ragazzon, D.; Borg, A.; Uvdal, P.; Skorodumova, N. V.; Sandell, A. *J. Phys. Chem. C* **2013**, *117*, 17078–17083.

(22) Ragazzon, D.; Schaefer, A.; Farstad, M.; Walle, L.; Palmgren, P.; Borg, A.; Uvdal, P.; Sandell, A. *Surf. Sci.* **2013**, *617*, 211–217.

(23) Ragazzon, D.; Farstad, M. H.; Schaefer, A.; Walle, L. E.; Uvdal, P.; Borg, A.; Sandell, A. *Submitted to Surf. Sci.* **2014**,

(24) Ragazzon, D.; Farstad, M. H.; Schaefer, A.; Walle, L. E.; Uvdal, P.; Palmgren, P.; Borg, A.; Sandell, A. *In manuscript* **2014**,

(25) Nyholm, R.; Svensson, S.; Nordgren, J.; Flodström, A. *Nucl. Inst. Meth. A* **1986**, *246*, 267–271.

(26) Beamline D1011 | MAX IV Laboratory. `https://www.maxlab.lu.se/node/38`.

(27) Vittadini, A.; Casarin, M.; Selloni, A. *J. Phys. Chem. C Lett.* **2009**, *113*, 18973–18977.

(28) Cavaliere, E.; Artiglia, L.; Rizzi, G. A.; Gavioli, L.; Granozzi, G. *Surf. Sci.* **2013**, *608*, 173–179.

(29) Zschack, P.; Cohen, J.; Chung, Y. *Surf. Sci.* **1992**, *262*, 395–408.

(30) Sedona, F.; Rizzi, G. A.; Agnoli, S.; Xamena, F. X. L. i.; Papageorgiou, A.; Osterman, D.; Sambi, M.; Finetti, P.; Schierbaum, K.; Granozzi, G. *J. Phys. Chem. B* **2005**, *109*, 24411–24426.

(31) Wendt, S.; Sprunger, P.; Lira, E.; Madsen, G.; Li, Z.; Hansen, J. O.; Matthiesen, J.; Blekinge-Rasmussen, A.; Læ gsgaard, E.; Hammer, B. r.; Besenbacher, F. *Science* **2008**, *320*, 1755–1759.

(32) Walle, L. L.; Ragazzon, D.; Borg, A.; Uvdal, P.; Sandell, A. *Surf. Sci.* **2014**, *621*, 77–81.

(33) Lindan, P. J. D.; Harrison, N. M. *Phys. Rev. Lett.* **1998**, *80*, 762–765.

(34) Henderson, M. *Langmuir* **1996**, *12*, 5093–5098.

(35) Artiglia, L.; Zana, A.; Rizzi, G. A.; Agnoli, S.; Bondino, F.; Magnano, E.; Cavaliere, E.; Gavioli, L.; Granozzi, G. *J. Phys. Chem. C* **2012**, *116*, 12532–12540.

(36) Muryn, C.; Hardman, P.; Crouch, J. *Surf. Sci.* **1991**, *251-252*, 747–752.

(37) Liu, P.; Rodriguez, J. A. *J. Chem. Phys.* **2007**, *126*, 164705.

Paper V

TiO_x thin films grown on Pd(100) by chemical vapor deposition

M. H. Farstad, D. Ragazzon, H. Grönbeck, M. D. Strømsheim, J. Gustafson, A. Sandell, and A. Borg

In manuscript

TiO_x thin films grown on Pd(100) by chemical vapor deposition

M. H. Farstad[1], D. Ragazzon[2], H. Grönbeck[3], M. D. Strømsheim[4], J. Gustafson[5], A. Sandell[2], and A. Borg[1]

[1]Department of Physics, Norwegian University of Science and Technology, NO-7491 Trondheim, Norway
[2]Department of Physics and Astronomy, Uppsala University, P. O. Box 530, SE-75121 Uppsala, Sweden
[3]Competence Centre for Catalysis and Department of Applied Physics, Chalmers Univ. of Technology, SE-412 96 Göteborg, Sweden
[5]Division of Synchrotron Radiation Research, Lund University, Box 118, SE-221 00 Lund, Sweden
[4]Department of Chemical Engineering, Norwegian University of Science and Technology, NO-7491 Trondheim, Norway

Abstract

The formation of TiO_x nanostructures on Pd(100) by chemical vapor deposition, using Titanium (IV)isopropoxide (TTIP) as precursor, has been investigated by high resolution photoelectron spectroscopy, low energy electron diffraction and scanning tunneling microscopy. Three different TiO_x phases and one Pd-Ti alloy phase have been identified. The Pd-Ti alloy phase is observed at the initial stages of film growth. Density functional theory (DFT) calculations suggest that Ti is alloyed into the second layer of Pd(100). Increasing the TTIP dose yields a partially oxidized wetting layer ($TiO_x, x < 2$), consisting of a mixture of structures with (3x5) and (4x5) periodicity with respect to the Pd(100) substrate. Increasing the coverage further results in growth of a fully oxidized (TiO_2) phase on top of the partially oxidized layer. In addition, a second fully oxidized phase can be formed by post-oxidizing a partially oxidized thin film. The TiO_2 phase prepared by post-oxidation is more weakly interacting with the Pd(100) substrate than the TiO_x wetting layer. The partially oxidized phase can be recovered by annealing the post-oxidized phase in ultra-high vacuum at temperatures $\geq 500°C$.

1 Introduction

Palladium (Pd) and titanium dioxide (TiO_2) are both versatile catalysts. Pd is efficient at adsorbing and splitting molecules such as O_2, and H_2 making it a viable catalyst for oxidation of hydrocarbons [1] and CO [2] as well as hydrogenation reactions [3]. TiO_2 has found widespread use within fields such

as photocatalysis (water purification and water splitting), solar fuel cells and self-cleaning coatings [4]. The combination of the two materials in the form of TiO_2 supported Pd particles has been considered as catalyst for the water-gas shift reaction [5–7] as well as for hydrogenation of CO_2 to methanol [8].

Pd particles supported on TiO_2 is furthermore a well-known example of a system that exhibits strong metal-support interaction (SMSI) [9–13]. The SMSI can lead to encapsulation of the metal particles by a thin oxide film. Heating of Pd and Pt particles deposited on TiO_2 in a reducing atmosphere has been found to result in the formation of a TiO_x layer on the metal particles [11–14]. Such an encapsulation can potentially suppress the catalytic activity, assuming that the encapsulated layer is retained during reaction conditions. However, it has recently been demonstrated that such a thin oxide film can be further oxidized and serve as oxygen donor under reaction conditions for CO oxidation, leading to enhanced catalytic activity [15, 16]. That also oxide particles on a metallic support can lead to a catalytic activity comparable to and even superior to the more traditional metal/oxide catalyst has been demonstrated in recent years [17, 18]. Moreover, in the case of supported particles, the importance of the particle-support boundary has been recognized [19]. From this it stands clear that the connection between the traditional (metal/oxide) and inverse (oxide/metal) systems is an important but complex issue that deserves further studies.

In the present work, we address the formation of ultrathin TiO_x structures on a Pd(100) single crystal surface. The most common method for thin film growth of TiO_x on metal substrates in ultra-high vacuum (UHV) is physical vapor deposition (PVD), either as reactive PVD (rPVD) where Ti is deposited in an O_2 atmosphere, or by post-oxidation where Ti is deposited and subsequently oxidized. In these ways atomically ordered TiO_x structures on single crystals of Pt [20, 21], Au [22] and Ag [23] have been prepared. In addition, ordered TiO_x structures formed on Pd and Pt particles deposited on the rutile $TiO_2(110)$ single crystal surface by virtue of the SMSI effect have also been demonstrated [13, 14].

We have employed a more unusual preparation route, namely chemical vapor deposition (CVD), which is particularly facile as both Ti and oxygen are provided by a single precursor. Titanium (IV)isopropoxide (TTIP) is such a single-source precursor for TiO_2 and we have recently demonstrated that well-ordered TiO_x films with a comparably low amount of defects can be grown on Au(111) in UHV by exposure to TTIP [24–26]. One advantage with CVD over PVD is the possibility to uniformly coat rough and porous materials, which enables the realization of a high surface area inverse catalyst [27].

The TiO_x thin films grown on Pd(100) using TTIP have been characterized by high-resolution photoelectron spectroscopy (HRPES), low energy electron diffraction (LEED) and scanning tunneling microscopy (STM). Furthermore, the thermal stability of the thin films in UHV has been tested. Three as deposited phases have been distinguished, a Pd-Ti surface alloy phase, one partially oxidized phase ($TiO_x, x < 2$) and one fully oxidized phase (TiO_2). An additional TiO_2 phase has been observed upon post-oxidation of the partially oxidized phase. In UHV the thin film phases start to reduce upon heating around 500°C and substantial reduction is observed around 600°C.

2 Experimental

HRPES and STM measurements were conducted in separate ultra high vacuum (UHV) chambers with base pressures in the low 10^{-10} mbar range. Both chambers were equipped with LEED, sputter gun and sample heating possibilities. The HRPES experiments were conducted at beamline I311 of the MAX II ring [28] at the MAX IV Laboratory in Sweden. Ti 2p spectra were measured with a photon energy of 590 eV, 650 eV were used for recording the O 1s spectra and both 400 eV and 460 eV were used for measuring Pd 3d core level spectra. The STM experiments were performed in our home laboratory at Norwegian University of Science and Technology with an Omicron STM 1 instrument. Tungsten tips were used for recording the STM images. The Pd(100) crystal (Surface Preparation Laboratory) was cleaned by cycles of Ar-sputtering and annealing with and without oxygen until no contaminants (typically carbon and sulfur) were detected by HRPES and a sharp (1x1) LEED pattern was observed.

The TiO_x thin film growth was performed by CVD using TTIP (Sigma Aldrich, purity 99.999%) as precursor. A glass tube containing TTIP was mounted on a leak valve connected to the chamber, and a tube doser made of stainless steel was used to direct the TTIP molecules towards the sample surface. The opening of the doser was positioned about 5 cm away from the sample surface. Dosing pressures ranged from $8 \cdot 10^{-9}$ mbar to $3 \cdot 10^{-8}$ mbar. The TTIP was purified by freeze–pump–thaw cycles and the gas line was baked in order to remove water.

Growth series of TiO_x thin films were performed in a stepwise manner, where small amounts of TTIP were dosed with the sample kept at selected temperatures followed by cooling down to room temperature (RT) for characterization by HRPES or STM and LEED. Prior to the HRPES measurements the sample was flashed to the growth temperature, unless otherwise stated, to remove unreacted TTIP adsorbed on the surface while cooling down.

The Pd 3d core level spectrum of clean Pd(100) has a surface contribution which is clearly observed when measured at photon energy 400 eV. The relative intensity of the surface component was used to estimate the amount of surface covered by TiO_x. The TiO_x thin film thickness was estimated by the attenuation of the Pd $3d_{5/2}$ bulk peak measured with a photon energy of 460 eV, taking uncovered areas into account if present. The Pd $3d_{5/2}$ spectra of the clean Pd(100) surface were fitted according to the procedure by Göthelid et al. [29, 30]. This means that three Doniach-Sunijc line profiles were used, one for the bulk peak at 334.86 eV, one for the surface contribution which is shifted -0.44 eV compared to the bulk peak and last one shifted 0.4 eV to higher binding energy (BE) compared to the bulk peak representing the rapidly varying density of states around the Fermi level [30–32].

3 Computational

Density functional theory (DFT) was employed using an implementation with plane-waves and pseudo-potentials [33,34]. The Perdew-Burke-Ernzerhof (PBE) approximation was used for the exchange and correlation (xc) functional [35] and ultrasoft scalar-relativistic pseudo-potentials were used to describe the

interaction between the valence electrons and the core [36]. The number of electrons treated variationally for each element was ten for Pd and twelve for Ti. A plane-wave kinetic energy cut-off of 380 eV was used to expand the Kohn-Sham orbitals. The lattice constant for Pd (fcc) was calculated to be 3.93 Å which is close to the experimental value of 3.89 Å.

The bare Pd(100) surface was represented by eleven atomic layers in a p(2x2) surface cell. Repeated slabs are separated by 16 Å vacuum. Reciprocal space integration over the Brillouin zone was approximated with a finite sampling of 13 special k-points. Structural optimization was performed without any constraints. The core level shifts for Pd(3d) were evaluated by the use of pseudo-potentials that were generated with an electron hole in the 3d shell. The approach assumes complete screening of the core-hole and has been used successfully over the years [37, 38].

4 Results and discussion

4.1 Growth and structure of TiO_x on Pd(100)

Growth of TiO_x phases on Pd(100) by CVD was performed at different temperatures ranging from 300°C to 500°C. When using TTIP it is however important to ensure complete precursor reaction. If the temperature is too low ligand residues will become incorporated in the film. This effect was apparent at 300°C while at 500°C the contribution from TTIP residues was minimal.

Still, at 500°C small amounts of atomic carbon could be detected in the C 1s spectrum at low coverages, that is, when free Pd surface was present. It is possible that this peak is due to adventitious carbon in the bulk diffusing to the surface during deposition but there could also be a contribution from a TTIP decomposition process. With respect to the TiO_x structures formed at 300°C, LEED shows similar patterns as for 500°C. The patterns are more diffuse, indicating a lower degree of order as compared to growth at 500°C. It is likely that the lower degree of order can be ascribed to ligand residues. Consequently, in the following we will focus on the films grown at 500°C as they are more pure and better ordered.

Ti $2p_{3/2}$ and Pd $3d_{5/2}$ spectra recorded after selected thin film deposition steps performed at 500°C are presented in Fig. 1. Results from curve fittings are included. For each situation, we have used the Pd $3d_{5/2}$ spectra to determine the fraction of the Pd(100) surface covered upon deposition as well as the average thickness of the deposited structures. These quantities are provided on the right side of Fig. 1. Four different contributions can be observed in the Ti $2p_{3/2}$ spectra upon increasing film thickness. In the following, the different situations encountered during the growth series will be presented and discussed. The results are subdivided into the Pd-Ti alloy formed at the initial stages of growth and the different TiO_x phases observed at the later stages of growth.

Pd-Ti alloy formation

At the lowest coverages studied, the Ti $2p_{3/2}$ core level spectrum has one main contribution at BE 454.98 eV. This state is indicated in yellow in Fig. 1.

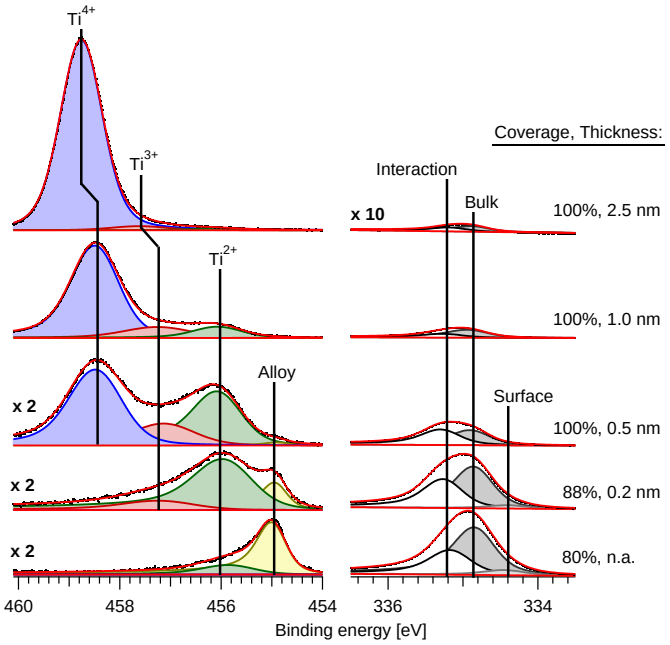

Figure 1. Selected Ti $2p_{3/2}$ and Pd $3d_{5/2}$ core level spectra from a TiO_x thin film growth series at 500°C. The three lower Ti spectra have been multiplied by a factor two, and the topmost Pd spectrum have been multiplied by a factor 10. The surface coverage and TiO_x average film thickness for each deposition is given on the right side of the plot.

The corresponding spectra of the O 1s region give no clear evidence for the presence of O species, although the identification is hampered by the overlap with the Pd $3p_{3/2}$ level. In the Pd $3d_{5/2}$ spectrum, the surface component decreases while a contribution shifted 0.35 eV to higher BE compared to the bulk component emerges. Only the 1x1 LEED pattern of Pd(100) is observed, that is, no ordered superstructure forms at this stage. The presence of Ti and absence of O indicate Pd-Ti alloy formation. Pd-Ti alloying has previously been studied with X-ray photoemission spectroscopy (XPS) [38]. The BE of the Ti $2p_{3/2}$ peak shifts towards higher binding energies relative to pure Ti when alloyed with Pd, the exact position depending on the amount of Ti relative to Pd. Smaller amounts of Ti gave larger shifts and a BE of 454.98 eV is consistent with formation of a low Ti content Pd-Ti alloy [38]. Alloying Pd with Ti also affects the Pd 3d peak, which shifts towards higher BE for increasing Ti content. The observed peak shift about 0.35 eV in the Pd $3d_{5/2}$ spectrum is also consistent with a low Ti content Pd-Ti alloy [38]. Moreover, using the Ti $2p_{3/2}$ peak at 454.98 eV as a signature of alloy formation, deposition at different temperatures indicates that Pd-Ti alloying requires a deposition temperature above 400°C.

When increasing the coverage the attenuation of the Pd $3d_{5/2}$ surface component shows that almost 80% of the surface are affected by Ti before a discernible oxygen contribution appears in the O 1s core level region. At this stage a second contribution, shifted towards higher BE is also emerging in the Ti $2p_{3/2}$ spectrum, as shown in the lower spectrum in Fig. 1.

To investigate the potential Pd-Ti alloy configurations, we have applied DFT calculations for determining Ti-induced BE shifts in the Pd $3d_{5/2}$ core level spectra. The Pd 3d surface core level shift (SCLS) of the clean Pd(100) surface is calculated to be -0.33 eV, slightly lower than the shift reported experimentally [32,39] and in agreement with previous calculations [40]. From our spectra we obtain a SCLS of -0.44 eV.

The option of having Ti adsorbed in four-fold hollow sites on top of the Pd surface at a coverage of 0.25 ML leads to a Pd 3d surface core level shift of 0.71 eV, which is too large compared to the experimental finding of 0.35 eV. Alloying of Ti into the first and second layer of the Pd(100) surface, illustrated for 0.25 ML coverage in Fig. 2, results in BE shifts for different Pd atoms in the surface region given in the figure.

Substitution of Ti into the outermost surface yields two distinct shifts for atoms in the first layer. Pd atoms directly bonded to Ti have an SCLS of 0.06 eV, whereas second nearest neighbors have a negative shift of -0.43 eV. Atoms in the second surface layer (all are coordinated to Ti) have a positive shift of 0.47 eV.

The alternative location of Ti in the second layer at the same 0.25 ML coverage results in a CLS of 0.05 eV for Pd atoms in the first layer. In the second layer, nearest and next-nearest neighbors to the Ti atom have shifts of 0.21 and 0.40 eV, respectively. Also the third layer is affected by the Ti substitution and atoms have CLS of 0.23 eV. For this coverage, incorporated Ti atoms will be observed as a loss of intensity in the surface contribution compared to the bulk contribution, as a shift of 0.05 eV is too small to be resolved from the bulk peak experimentally. The calculated shifts for the second and third Pd layer are in reasonable agreement with the experimental results, obtained at photon energies of 400 eV and 460 eV, which also indicate that these shifts originate from atoms below the surface.

Larger amounts of Ti yield significantly larger shifts, which are inconsistent with the experimental results, supporting that a low amount (less than 25% of a monolayer) of Ti is alloyed into the Pd substrate surface region. The comparison between the HRPES experiments and the DFT calculations suggests that Ti is substituted in either the first or the second surface layer.

The formation of a Pd-Ti surface alloy is a consequence of the positive surface segregation energy of Ti impurities in a Pd host [41, 42]. From our DFT calculations, we have determined the relative stability of alloying Ti into different layers in the surface region of Pd(100). The results, presented in Fig. 3, clearly demonstrate that Ti located in the second layer is energetically favorable for low Ti contents. Ti will remain in the second layer until the coverage is sufficient for continued diffusion into the bulk of the crystal. The difference between Ti in the surface and the interior of the slab gives an estimate of the surface segregation energy (0.66 eV). Although there is a strong thermodynamic preference for alloying, the process is associated with energy barriers and at this point we do not know how facile the Ti diffusion

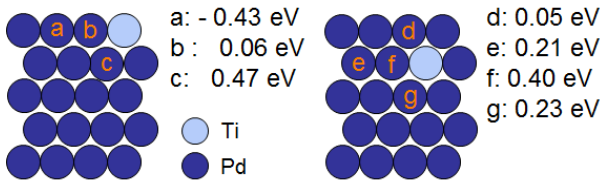

Figure 2. Schematic illustrations of the models used to calculate the Pd 3d core level shifts relative to a Pd atom in the bulk, for a coverage corresponding to 0.25 ML (side view).

into the bulk is.

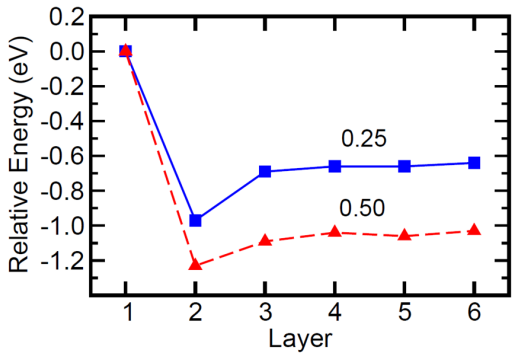

Figure 3. Calculated relative energies of Ti alloyed into different layers of Pd(100) for two different amounts of Ti, 0.25 and 0.5 of one full Pd layer.

STM images, shown in Fig. 4, recorded of the alloy phase, exhibit a slightly buckled 1x1 surface layer. As will be discussed below, the surface alloy has in this case been formed by reduction of a film covering a larger portion of the surface in UHV by annealing to 540°C (temperature measured by pyrometer). The buckling is most likely caused by strain due to Ti atoms incorporated into the Pd(100) second layer. The wormlike structures seen on top of the surface layer as well as decorating step edges, originate from carbon segregating to the surface in the annealing process [43], as any residues after TTIP decomposition are expected to decompose or evaporate when the surface is annealed above 500°C.

Oxide formation

Increasing the TTIP exposure leads to appearance and growth of a second contribution in the Ti $2p_{3/2}$ core level spectra (indicated in green in Fig. 1). The BE is 455.9 eV, which is typical for Ti species with oxidation state ranging from 2+ to 3+ [20]. For convenience this Ti-peak will be referred to as Ti^{2+}. This peak is accompanied by a contribution in the O 1s spectrum, at BE

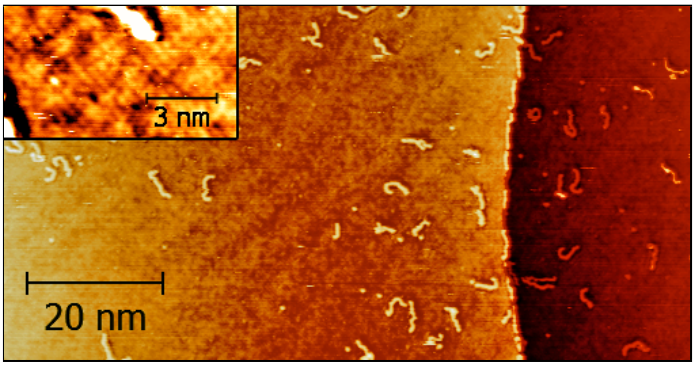

Figure 4. STM images of the alloy phase. The worm like structures are surface carbon contamination. A long range order can be seen as a buckling of the surface. The inset shows the atomic structure of this surface, which appears somewhat disordered, however there are no obvious regular additional atoms.

529.8 eV. The presence of Ti of oxidation state less than +4 and O thus shows that, a partially oxidized phase ($TiO_x, x < 2$) has formed. The Pd $3d_{5/2}$ core level spectrum displays a peak shifted 0.4-0.5 eV relative to the bulk peak. As judged from the photon dependent intensity variations of the spectral features, this contribution originates from the surface of the Pd crystal. It should be noted that atomic oxygen adsorbed on the Pd(100) surface yields similar shifts to higher binding energies [44]. Thus, we cannot distinguish between effects on Pd due to alloy formation and oxide formation. At this point, a small contribution in the Ti $2p_{3/2}$ spectra (shown in red) at BE 457.0 eV also appears. This peak has a BE consistent with Ti^{3+} species [20].

The LEED pattern of this partially oxidized phase is displayed in Fig. 5. It can be interpreted in terms of a combination of two independent patterns, corresponding to a (4x5) structure and a (3x5) structure. That is, two different structures of TiO_x coexist on the surface. The diffraction spots due to the two patterns are indicated as green (4x5) and red (3x5) circles overlaid the right side of the LEED pattern in Fig. 5. STM images reveal that this phase consists of many small domains covering the surface, as shown in Fig. 6. Two domain orientations can be discerned, rotated 90° with respect to each other. The inset shows the structure of one domain, atomically resolved, displaying the 3x5 periodicity observed in LEED. The atomic structure of this phase comprises triple rows of atoms separated by a 'trench'. The atoms are close packed along these triple rows. If the lines of atoms running about 60° to the trenches are studied more closely it becomes apparent that every fourth row has a slightly lower apparent height than the neighboring rows. These rows are indicated with gray dash lines in the inset of Fig. 6. Based on observations by STM the two structures must be either quite closely related resulting in the same contrasts seen by STM or they may be two different relaxations of the same structure. Due to the close relationship between these to structures the combination of them are referred to as the partially oxidized phase.

HRPES measurements indicate that this phase is slightly below 0.2 nm thick, corresponding to a single layer of TiO_x on top of the Pd(100) surface. This phase continues to spread until it covers about 90% of the Pd(100) surface, thus forming a wetting layer. The STM results, shown in Fig. 6, furthermore indicate that only small gaps between the different domains remain at this stage.

There are reports of STM images with a striking resemblance to the one displayed in Fig. 6, in particular the z-TiO_x phase reported on Pt(111) [12,20]. The z-phase on Pt(111) also exhibit triple rows, but the zigzag contrast along the triple rows is more prominent than on the Pd(100). Moreover, on Pt(111) every second row running at 60° to the trenches are lower than the others, in contrast to every fourth on Pd(100). This also allows for a smaller unit cell on Pt(111). By comparing the sizes of the unit cells is it evident that the TiO_x structure is more closely packed on Pd(100) than on Pt(111).

A 3x5 LEED pattern was also observed for a TiO_x phase grown on Pt(100) [45]. Furthermore, the Ti $2p_{3/2}$ peak was reported at 455.9 eV, as for the partially oxidized phase on Pd(100), indicating that these two structures could be similar. However, the structures observed by STM are quite different, a difference which needs further studies to clarify.

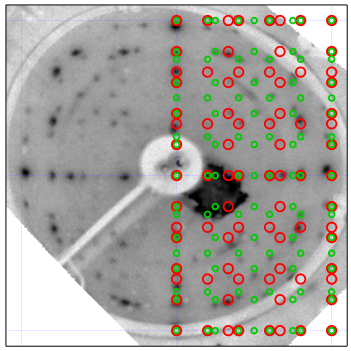

Figure 5. LEED pattern of the partially oxidized phase. The superimposed circles on the right half is a possible interpretation of the LEED pattern from the partially oxidized phase, a combination of a 3x5 (red circles) and a 4x5 (green circles) pattern.

When the coverage of TiO_x on Pd(100) exceeds 100% the alloy contribution quickly diminishes in the Ti $2p_{3/2}$ spectra. At the same time, one new, major contribution develops at BE 458.5 eV, indicated in blue in Fig. 1. This BE is characteristic of Ti^{4+} species [20]. Thus fully oxidized titania, TiO_2, has been formed at this coverage. This phase does not affect the shape of the Pd $3d_{5/2}$ core level spectrum; there is only a damped intensity due to growing film thickness. The initial growth of this phase is accompanied by a significant contribution of Ti^{3+}. However, there is no significant increase of Ti^{3+} species once Ti^{4+} has started to form. With increasing TiO_x film thickness the peaks shift to higher BE, which may be related to band bending (initial state) and/or screening (final state) effects. The bright clusters observed in

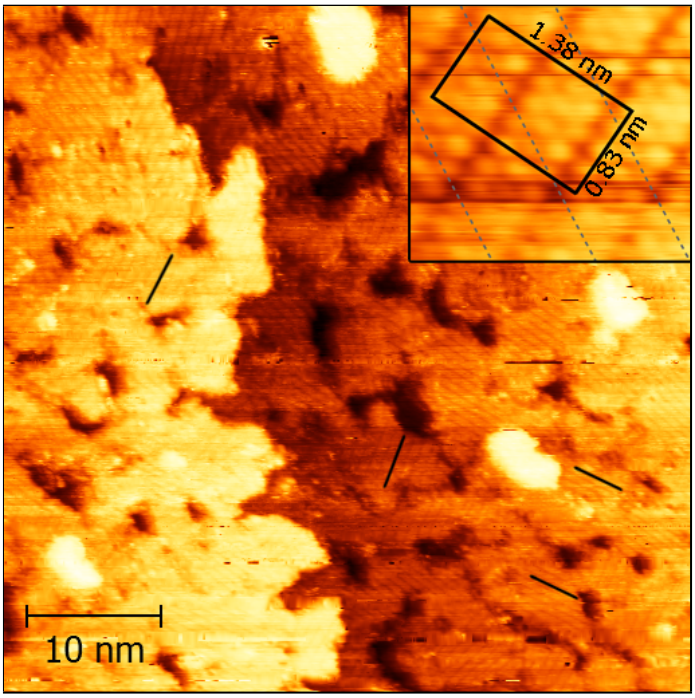

Figure 6. STM image of the partially oxidized phase revealing domains of two orientations, indicated by black lines for four domains. The inset shows this phase atomically resolved with the 3x5 unit cell observed in LEED drawn on top. The gray dashed lines indicates rows of lower apparent height.

Fig. 6 are likely to be the signature of initial fully oxidized phase formation. The fully oxidized phase has a more easily interpreted LEED pattern, which can be seen in Fig. 7. The simulated LEED pattern marked by green circles in Fig. 7 yields a $\begin{pmatrix} -2 & 1 \\ 1 & 1 \end{pmatrix}$ structure. Some of the LEED spots are smeared into triangles indicating strain in the structure. A slight decrease in the (2,1) matrix element leads to a distortion (red spots) in the simulated pattern which nicely accounts for the observed smearing in the LEED pattern. However, the specific structure of the fully oxidized phase grown on Pd(100) remains to be determined as the unit cell lengths obtained from the LEED pattern do not coincide with unit cells of any low index surfaces of rutile or anatase. It can be noted, though, that the LEED pattern observed for the TiO_2 phase on Pd(100) is distinctly different from those reported for Au(100) and Ag(100), where Rutile TiO_2(100)(1x1) [46] and Rutile TiO_2(110) [23] have been observed, respectively.

As is evident from Fig. 1 and the discussion above, the chemical composition of the deposited TiO_x thin films changes significantly with coverage. The behavior is summarized in Fig. 8, showing the development of the peak area

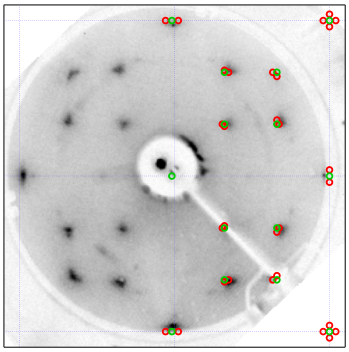

Figure 7. LEED image with suggested interpretation for the fully oxidized phase, including the simulated LEED pattern (green circles) and the corresponding simulation of the distortion (red circles) superimposed on the right half of the image.

of the Ti $2p_{3/2}$ peaks as well as the O 1s peak as function of the TiO_x coverage on the Pd(100) surface. The spectra were normalized to ring current and number of sweeps before background subtraction. The Ti $2p_{3/2}$ intensities are color coded in accordance with the coloring applied in Fig. 1. The intensity observed for the alloy contribution indicate that the surface can only accommodate a limited amount of alloyed Ti upon exposure to TTIP at 500°C. Noteworthy, when the Pd(100) surface is completely covered by oxidized Ti species, the alloy contribution disappears, implying that all deposited Ti is oxidized at this stage.

The Ti^{3+} contribution appears as the partially oxidized layer reaches close to full coverage. Relatively more Ti^{3+} species arise at the point where the Ti^{4+} component appears. After the Ti^{2+} and Ti^{3+} contributions have reached their respective maximum intensities, at film thickness of about 1 nm for the Ti^{3+} contribution, their spectral weights decrease at similar rate, indicating that both the partially oxidized phase and the Ti^{3+} species are covered by the Ti^{4+} phase in a comparable manner. At these coverages the intensities of the Ti^{4+} and O 1s components also increases at similar rates supporting this conjecture. As the Ti^{2+} phase is already seen to wet the Pd(100) surface it is reasonable to conclude that Ti^{3+} are primarily distributed in a layer just on top of the Ti^{2+} wetting layer. The observed behavior of the Ti^{3+} species implies that these species primarily serve as a transition layer between the partially oxidized and the fully oxidized phases. A schematic representation of the growth of TiO_x on Pd(100) is presented in Fig. 9.

A similar growth behavior has been observed for TiO_2(B)(001) grown on Pt(111) where an ultrathin film of TiO_x is formed on the Pt surface upon which the fully oxidized TiO_2(B) phase grows [47]. In particular, on surfaces of Pt-Ti alloys, a wetting layer of partially oxidized TiO_x tends to form upon which fully oxidized TiO_2 grow [48]. The results of TiO_x thin films growth on Pd(100) reported in the present work may indicate that this behavior is a general trend for reactive surfaces.

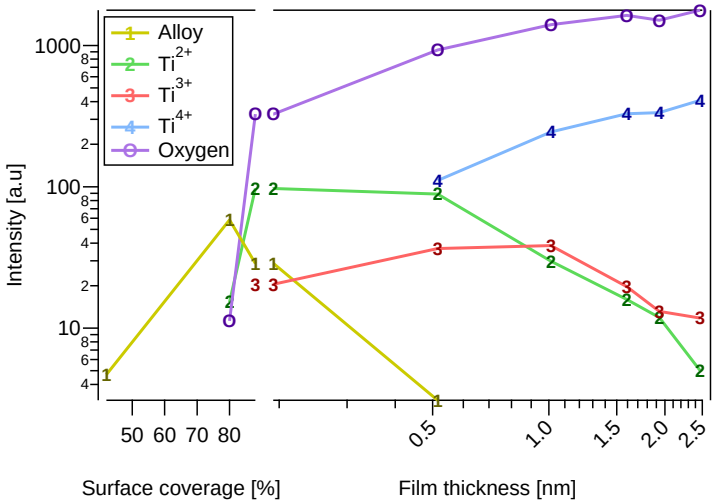

Figure 8. Development of peak area for the four different Ti $2p_{3/2}$ core level contributions as well as the O 1s peak during the 500°C growth series. The Ti peaks are numbered according to increasing oxidation state, 1 corresponds to the alloy component and 4 to Ti^{4+} component. The oxygen component is labeled O.

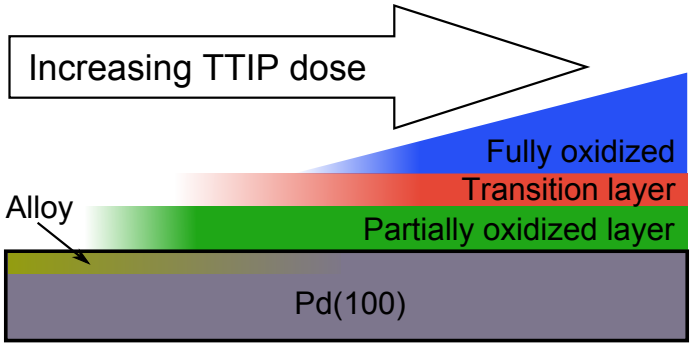

Figure 9. Schematic presentation of the observed TiO_x growth on Pd(100).

4.2 Oxidation and reduction of the TiO_x structure

The stability of the partially oxidized wetting layer with respect to oxidation and subsequent heating under UHV conditions has also been investigated.

Oxidation of the TiO_x phase was achieved by simultaneously dosing O_2 and heating the sample to 500°C. Fig. 10 displays corresponding Ti $2p_{3/2}$ (left) and Pd $3d_{5/2}$ (right) core level spectra of an as deposited partially oxidized thin film (A), the same film, after subsequent oxidation at 500°C in $5 \cdot 10^{-5}$mbar of O_2 (B) and heating to 500°C in UHV (C). In the Ti $2p_{3/2}$ spectrum of the as deposited film the Ti^{2+} component clearly dominates but the curve fitting reveals contributions from the alloy phase and initial Ti^{3+} and Ti^{4+} states. The corresponding Pd $3d_{5/2}$ core level spectrum is dominated by the TiO_x-induced peak at 335.3 eV. Apart from the TiO_x-induced state and the bulk state there is also a tiny feature due to free Pd surface (at BE 334.5 eV). The low intensity of the surface component shows that the surface is almost completely covered (99%) by the partially oxidized phase. The average thickness of this preparation is about 0.6 nm.

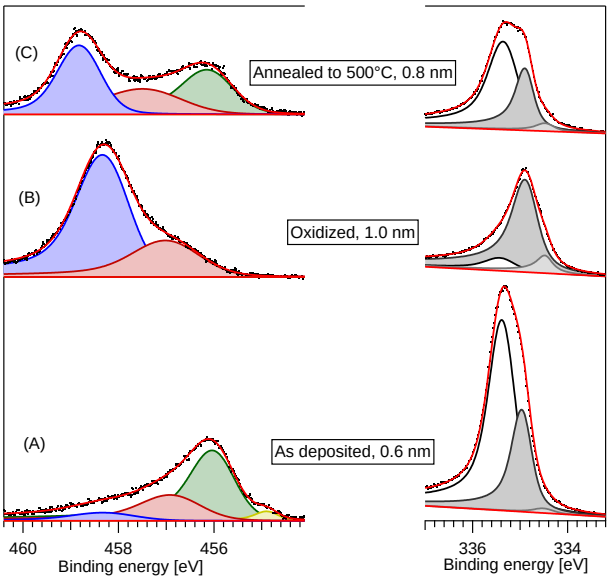

Figure 10. Ti $2p_{3/2}$ (left) and Pd $3d_{5/2}$ (right) core level spectra including curve fittings. Panel (A) displays the spectra for the as deposited film, (B) shows spectra after the preparation after oxidation at 500°C in $5 \cdot 10^{-5}$ mbar of O_2, and (C) shows the resulting spectra after subsequent annealing to 500°C in UHV. The film thickness is indicated for each step.

After oxidation (panel (B) in Fig. 10), the Ti^{4+} state dominates the Ti $2p_{3/2}$ spectrum. Thus, a fully oxidized film, i.e. with TiO_2 stoichiometry, has formed. There is also a significant amount of Ti^{3+} states, but there is

no clear trace of Ti^{2+} species. The film thickness has increased to 1.0 nm during the oxidation process and the surface contribution in the Pd $3d_{5/2}$ spectrum has increased slightly, now indicating a coverage of about 95%. The LEED pattern is different from any of the patterns observed for the previously discussed phases. It displays a (12x 4/3) structure relative to Pd(100), see Fig. 11a, where the simulated pattern of this structure is superimposed the LEED pattern in the right part of the figure. Immediately after oxidation there may also be (2x2) spots present from oxygen adsorbed on exposed Pd(100) areas as well as some elongated spots at (2x 12/11). However, both these sets of spots can be removed by a dose of about 10 L CO at room temperature, which supports the notion that the (2x2) spots originates oxygen adsorbed on Pd(100). The origin of the (2x 12/11) spots are not known at this point.

The Pd $3d_{5/2}$ spectrum furthermore indicates that the interaction between the Pd(100) substrate and the as deposited TiO_x phase is different from that between the substrate and the TiO_2 phase formed upon post-oxidation. The peak at 335.3 eV has almost disappeared, there is only a weak peak at 335.4 eV. Its position and relative intensity is in fact in agreement with the extra peak needed to fit clean Pd spectra as reported in [30]. Consequently, the spectrum suggests that the Pd atoms in contact with the TiO_2 overlayer have a Pd $3d_{5/2}$ core level BE similar to Pd atoms in the bulk. In an initial state picture, the Pd 3d chemical shifts suggest that the Ti^{2+} wetting layer interacts more strongly with the Pd(100) surface than the fully oxidized layer formed upon oxidation of the partially oxidized phase.

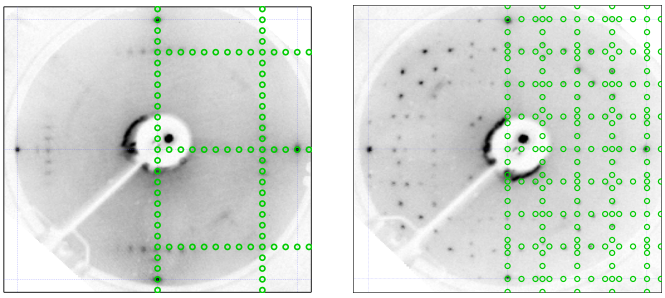

(a) **(b)**

Figure 11. LEED patterns with suggested interpretation overlaid on the right side. (a) After oxidizing the reduced phase, which results in a (12x 4/3) structure, and (b) after subsequent annealing and reduction back to a reduced phase with a (4x10) structure.

When the post-oxidized phase is annealed at 500°C in UHV the film becomes reduced again. The Ti $2p_{3/2}$ core level spectrum in panel (C) of Fig. 10 displays a substantial decrease in the intensity of the Ti^{4+} peak, and the Ti^{2+} peak has reappeared. In the Pd $3d_{5/2}$ spectrum the TiO_x-induced peak at 335.3 eV has returned, supporting the interpretation that this peak is related to the Ti^{2+} wetting phase. Also the surface contribution has decreased in intensity and the film thickness is reduced. At this point the LEED pattern

shows a (4x10) structure relative to Pd(100). This pattern is interpreted as a structure related to the (4x5) structure observed for the partially oxidized phase, by a doubling of the unit cell in one direction. On this basis, we propose the following oxidation-reduction scheme: Upon oxidation of the TiO_x film the wetting layer is transformed into a fully oxidized (TiO_2) layer on top of the Pd(100) surface which is interacting less strongly with the underlying substrate. When this film releases oxygen and the interaction with Pd(100) increases again, the resulting TiO_x structure may be allowed to form a more stable configuration resulting in a larger coincidence cell, possibly due to larger TiO_x islands. If the annealing temperature is increased, further reduction of the TiO_x thin film is observed. Full reduction with only the Pd-Ti alloy phase remaining can be obtained after annealing to about 690°C in UHV, a procedure which was used for obtaining the STM image of the alloy phase presented in Fig. 4.

The different structures and oxidation states available through TiO_x thin film phases grown on Pd(100), in combination with post-oxidation and reduction, provide a versatile model system for investigating selected catalytic reactions. The Ti oxidation state can be tailored, which allows for tuning the influence of the oxide as source and reservoir for oxygen in oxidation and reduction reactions. Furthermore, different configurations for boundaries between the metal substrate and partially and fully oxidized phases can be prepared suited for addressing the particular influence on reactivity. Systems such as FeO on Pt [15,16] and Au on TiO_2 [19] with high activity towards CO oxidation give an idea of what is possible both in terms of understanding the underlying mechanisms and for tailoring future catalysts by studying these types of systems.

5 Conclusions

Three different phases have been identified upon CVD growth of TiO_x thin films on Pd(100), using TTIP as precursor. A growth temperature of 500°C is required to form clean films upon deposition. At the lowest coverages a Pd-Ti alloy phase is formed. DFT calculations suggest that the Ti is alloyed into the second layer of Pd(100) and the calculated Ti-induced BE shifts in the Pd $3d_{5/2}$ core level spectra for this configuration is consistent with the experimental findings. Increasing coverage yields a partially oxidized, TiO_x with $x < 2$, wetting layer, consisting of domains with (3x5) and (4x5) periodicity with respect to the Pd(100) substrate. Increasing the coverage further results in growth of a fully oxidized phase on top of the this layer. The partially oxidized phase can be fully oxidized by heating in oxygen at 500°C. The resulting thin film presents a system more weakly interacting with the Pd(100) substrate than the TiO_x wetting layer. The partially oxidized TiO_x phase can be recovered by annealing in UHV at temperatures $\geq$ 500°C. As partially and fully oxidized phases can be prepared alongside clean Pd(100) surface areas, these configurations can provide an interesting testbed for investigations of cooperative effects in the Pd/TiO_x system, displaying strong metal support interaction.

6 Acknowledgments

Financial support was received from the Swedish Energy Agency (STEM), the Swedish Science Council (VR), the Trygger foundation, the Crafoord foundation, NordForsk and the Göran Gustafsson foundation. We thank the staff at MAX-lab for their support.

References

[1] W. Wu, H. Jiang, *Acc. Chem. Res.* **45**, 1736 (2012).

[2] J. Szanyi, W. Kuhn, D. Goodman, *J. Phys. Chem.* **98**, 2978 (1994).

[3] D. Teschner, J. Borsodi, A. Wootsch, Z. Révay, M. Hävecker, A. Knop-Gericke, S. D. Jackson, R. Schlögl, *Science* **320**, 86 (2008).

[4] M. A. Henderson, *Surf. Sci. Rep.* **66**, 185 (2011).

[5] L. Millard, M. Bowker, *J. Photochem. Photobiol. A Chem.* **148**, 91 (2002).

[6] P. Panagiotopoulou, D. I. Kondarides, *Catal. Today* **112**, 49 (2006).

[7] P. Panagiotopoulou, *J. Catal.* **225**, 327 (2004).

[8] L. Fan, K. Fujimoto, *Bull. Chem. Soc. Jpn.* **67**, 1773 (1994).

[9] M. Spencer, *J. Catal.* **93**, 216 (1985).

[10] T. Suzuki, R. Souda, *Surf. Sci.* **448**, 33 (2000).

[11] O. Dulub, W. Hebenstreit, U. Diebold, *Phys. Rev. Lett.* **84**, 3646 (2000).

[12] M. Bowker, P. Stone, P. Morrall, R. Smith, R. Bennett, N. Perkins, R. Kvon, C. Pang, E. Fourre, M. Hall, *J. Catal.* **234**, 172 (2005).

[13] M. Bowker, E. Fourré, *Appl. Surf. Sci.* **254**, 4225 (2008).

[14] D. Jennison, O. Dulub, W. Hebenstreit, U. Diebold, *Surf. Sci.* **492**, L677 (2001).

[15] Y.-N. Sun, Z.-H. Qin, M. Lewandowski, E. Carrasco, M. Sterrer, S. Shaikhutdinov, H.-J. Freund, *J. Catal.* **266**, 359 (2009).

[16] Y.-N. Sun, L. Giordano, J. Goniakowski, M. Lewandowski, Z.-H. Qin, C. Noguera, S. Shaikhutdinov, G. Pacchioni, H.-J. Freund, *Angew. Chem. Int. Ed. Engl.* **49**, 4418 (2010).

[17] J. A. Rodriguez, S. Ma, P. Liu, J. Evans, M. Perez, J. Hrbek, J. Evans, M. Perez, *Science* **318**, 1757 (2007).

[18] J. Graciani, K. Mudiyanselage, F. Xu, A. E. Baber, J. Evans, S. D. Senanayake, D. J. Stacchiola, P. Liu, J. Hrbek, J. F. Sanz, J. A. Rodriguez, *Science* **345**, 546 (2014).

[19] I. X. I. Green, W. Tang, M. Neurock, J. T. J. Yates, J. T. Y. Jr, J. T. J. Yates, *Science* **333**, 736 (2011).

[20] F. Sedona, G. A. Rizzi, S. Agnoli, F. X. L. i. Xamena, A. Papageorgiou, D. Osterman, M. Sambi, P. Finetti, K. Schierbaum, G. Granozzi, *J. Phys. Chem. B* **109**, 24411 (2005).

[21] S. Agnoli, T. Orzali, M. Sambi, A. Vittadini, M. Casarin, G. Granozzi, *J. Phys. Chem. C* **112**, 20038 (2008).

[22] C. Wu, M. S. J. Marshall, M. R. Castell, *J. Phys. Chem. C* **115**, 8643 (2011).

[23] A. Atrei, A. M. Ferrari, D. Szieberth, B. Cortigiani, G. Rovida, *Phys. Chem. Chem. Phys.* **12**, 11587 (2010).

[24] D. Ragazzon, A. Schaefer, M. Farstad, L. Walle, P. Palmgren, A. Borg, P. Uvdal, A. Sandell, *Surf. Sci.* **617**, 211 (2013).

[25] D. Ragazzon, M. H. Farstad, A. Schaefer, L. E. Walle, P. Uvdal, A. Borg, A. Sandell, *Submitted to Surf. Sci.* (2014).

[26] D. Ragazzon, M. H. Farstad, A. Schaefer, L. E. Walle, P. Uvdal, P. Palmgren, A. Borg, A. Sandell, *In manuscript* (2014).

[27] A. Schaefer, D. Ragazzon, L. Walle, M. Farstad, A. Wichmann, M. Bäumer, A. Borg, A. Sandell, *Appl. Surf. Sci.* **282**, 439 (2013).

[28] R. Nyholm, J. Andersen, U. Johansson, B. Jensen, I. Lindau, *Nucl. Inst.Meth. A* **467-468**, 520 (2001).

[29] M. Göthelid, H. von Schenck, J. Weissenrieder, B. Å kermark, A. Tkatchenko, M. Galván, *Surf. Sci.* **600**, 3093 (2006).

[30] M. Göthelid, M. Tymczenko, W. Chow, S. Ahmadi, S. Yu, B. Bruhn, D. Stoltz, H. von Schenck, J. Weissenrieder, C. Sun, *J. Chem. Phys.* **137**, 204703 (2012).

[31] G. Wertheim, P. Citrin, *Photoemiss. Solids I*, M. Cardona, L. Ley, eds. (Springer Berlin Heidelberg, Berlin, Heidelberg, 1978), vol. 26 of *Topics in Applied Physics*, pp. 197–236.

[32] R. Nyholm, M. Qvarford, *J. Phys. Condens. Matter* **4**, 277 (1992).

[33] M. C. Payne, M. P. Teter, D. C. Allan, T. A. Arias, J. D. Joannopoulos, *Rev. Mod. Phys.* **64**, 1045 (1992).

[34] S. J. Clark, M. D. Segall, C. J. Pickard, P. J. Hasnip, M. J. Probert, K. Refson, M. C. Payne, *Zeitschrift fuer Kristallographie* **220**, 567 (2005).

[35] J. P. Perdew, K. Burke, M. Ernzerhof, *Phys. Rev. Lett.* **77**, 3865 (1996).

[36] D. Vanderbilt, *Phys. Rev. B* **41**, 7892 (1990).

[37] E. Pehlke, M. Scheffler, *Phys. Rev. Lett.* **71**, 2338 (1993).

[38] R. Westerström, *et al.*, *Phys. Rev. B* **83**, 115440 (2011).

[39] L. Walle, H. Grönbeck, V. Fernandes, S. Blomberg, M. Farstad, K. Schulte, J. Gustafson, J. Andersen, E. Lundgren, A. Borg, *Surf. Sci.* **606**, 1777 (2012).

[40] J. Andersen, D. Hennig, E. Lundgren, M. Methfessel, R. Nyholm, M. Scheffler, *Phys. Rev. B* **50**, 17525 (1994).

[41] A. Ruban, H. Skriver, J. Nørskov, *Phys. Rev. B* **59**, 15990 (1999).

[42] A. Ruban, H. Skriver, J. Nørskov, *Surface Alloys and Alloys Aurfaces*, vol. 10 of *The Chemical Physics of Solid Surfaces* (Elsevier, 2002).

[43] M. Bowker, J. Counsell, K. El-Abiary, L. Gilbert, C. Morgan, S. Nagarajan, C. S. Gopinath, *J. Phys. Chem. C* **114**, 5060 (2010).

[44] M. Todorova, E. Lundgren, V. Blum, A. Mikkelsen, S. Gray, J. Gustafson, M. Borg, J. Rogal, K. Reuter, J. Andersen, M. Scheffler, *Surf. Sci.* **541**, 101 (2003).

[45] T. Matsumoto, M. Batzill, S. Hsieh, B. E. Koel, *Surf. Sci.* **572**, 127 (2004).

[46] A. Calloni, A. Ferrari, A. Brambilla, F. Ciccacci, L. Duò, *Thin Solid Films* **520**, 3922 (2012).

[47] L. Artiglia, A. Zana, G. A. Rizzi, S. Agnoli, F. Bondino, E. Magnano, E. Cavaliere, L. Gavioli, G. Granozzi, *J. Phys. Chem. C* **116**, 12532 (2012).

[48] U. Bardi, *Catal. Letters* **5**, 81 (1990).

Paper VI

TiO_x thin films grown on Pd(111) by chemical vapor deposition

M. H. Farstad, D. Ragazzon, M. D. Strømsheim, J. Gustafson, A. Sandell, and A. Borg

In manuscript

Growth and oxidation/reduction behavior of TiO_x thin films on Pd(111)

M. H. Farstad[1], D. Ragazzon[2], M. D. Strømsheim[3], J. Gustafson[4], A. Sandell[2], and A. Borg[1]

[1]Department of Physics, Norwegian University of Science and Technology, NO-7491 Trondheim, Norway
[2]Department of Physics and Astronomy, Uppsala University, P. O. Box 530, SE-75121 Uppsala, Sweden
[3]Department of Chemical Engineering, Norwegian University of Science and Technology, NO-7491 Trondheim, Norway
[4]Division of Synchrotron Radiation Research, Lund University, Box 118, SE-221 00 Lund, Sweden

Abstract

The formation of TiO_x thin film phases on Pd(111) by chemical vapor deposition, using Titanium (IV)isopropoxide (TTIP) as precursor, has been investigated by high resolution photoelectron spectroscopy (HRPES), low energy electron diffraction (STM) and scanning tunneling microscopy (STM). Three different as-deposited phases, an alloy phase, a partially oxidized phase (TiO_x; $x<2$) and a fully oxidized (TiO_2 phase), are observed. The HRPES results show that these phases chemically are quite similar to those observed for growth of TiO_x thin films on Pd(100) [1]. The LEED pattern recorded of the fully oxidized phase suggests that this phase may have a TiO_2(B)(001) structure, with an expanded unit cell. The partially oxidized phase forms a wetting layer with a rectangular unit cell, as determined by LEED, consisting of a double row zigzag structure at the atomic level. Oxidation of this partially oxidized phase yields a different fully oxidized phase, which only partly covers the Pd(111) surface. This phase may also be reversibly reduced back to the original phase. The combination of an easily and reversibly oxidizable phase with exposed Pd areas makes the partially oxidized TiO_x phase on Pd(111) promising as a model catalyst.

1 Introduction

Palladium (Pd) and titanium dioxide (TiO_2) are both materials known to be versatile catalysts. Pd, efficiently splitting molecules such as H_2 and O_2 upon adsorption, is used as catalyst in oxidation of hydrocarbons [2] and CO [3]. Furthermore, palladium is highly suited for catalyzing hydrogenation reactions [4]. The applications of TiO_2 range from photocatalysis for water

purification and water splitting, solar fuel cells and self-cleaning coatings [5]. Combining the two materials in the form of TiO_2 supported Pd particles has been considered as catalyst for the water-gas shift reaction [6–8] as well as for hydrogenation of CO_2 to methanol [9].

Particles of Pd supported on TiO_2 moreover represents a prototype system exhibiting strong metal-support interaction (SMSI) [10–14]. SMSI can cause the metal particles to be coated by a TiOx layer potentially quenching the catalytic activity. However, it has recently been demonstrated that such a thin oxide film can be further oxidized and serve as oxygen donor under reaction conditions for CO oxidation, leading to enhanced catalytic activity [15, 16]. That oxide particles on a metallic support, commonly referred to as an inverse catalyst system, can lead to a catalytic activity comparable to and even superior to the more traditional metal/oxide catalyst has been shown during recent years [17, 18]. For such materials configurations, the importance of the particle-support boundary has been recognized [19], motivating further studies of oxide on metal systems. In the present work, we address the formation of ultrathin TiO_x structures on a Pd(111) single crystal surface as model system in this context.

TiO_x phases on Au(111) and Pt(111) have recently been investigated, motivated by the catalytic behavior of these materials systems. Furthermore, Au represents a more inert substrate than Pt, which affects the TiO_x phases formed. Applying physical vapor deposition, Wu et al. [20] obtained three different ordered TiO_x film structures on Au(111) with increasing amount of deposited Ti, a (2x2) honeycomb structure, a pinwheel structure and triangular islands which coalesce as coverage increases. Similar structures have been obtained by chemical vapor deposition using Titanium (IV)isopropoxide (TTIP) as precursor in combination with annealing [21,22]. In addition, a fully oxidized TiO_2(B)(001) phase is obtained [23]. On Pt(111), Sedona et al. [24] demonstrated formation of six different long range ordered TiO_x phases by a combination of reactive evaporation of Ti in oxygen and annealing at selected conditions, including an incommensurate nonwetting, fully oxidized rect-TiO_2 phase. More recently, a TiO_2(B)(001) polymorph has also been reported [25].

In this paper, TiO_x thin films were grown on Pd(111) by means of CVD using TTIP as precursor. The resulting thin films have been characterized by high-resolution photoelectron spectroscopy (HRPES), low energy electron diffraction (LEED) and scanning tunneling microscopy (STM). Three as-deposited phases have been distinguished, a Pd-Ti surface alloy phase, one partially oxidized (TiO_x; $x<2$) phase and one fully oxidized phase (TiO_2). Another fully oxidized TiO_2 have been identified upon post-oxidation of as deposited partially oxidized thin films. The stability of the resulting thin film structure upon heating in ultra high vacuum (UHV) and in a background pressure of CO and subsequent reoxidation were investigated. Reversible oxidation and reduction of the TiO_x thin films were demonstrated.

2 Experimental

HRPES and STM measurements were performed in separate ultra high vacuum (UHV) chambers with base pressures in the low 10^{-10} mbar range. Both chambers were equipped with LEED, sputter gun and sample heating capabil-

ities. The HRPES experiments were performed at beam line I311 of the MAX II ring [26] at the MAX IV Laboratory. The HRPES spectra were measured with photon energies of 650 eV for O 1s, 560 eV for Ti 2p and both 400 eV and 460 eV were used for recording the Pd 3d core level spectra. The STM measurements were conducted in our home lab at Norwegian University of Science and Technology with an Omicron VT-STM operated at room temperature. The STM images were recorded using tungsten tips. Noise removal by Fast Fourier Transformation (FFT) has been applied to the STM images.

The Pd(111) crystal was cleaned by cycles of Ar-sputtering and annealing both in O_2 and in UHV until no carbon or sulfur contaminants were observed by HRPES and a well defined (1x1) LEED pattern was obtained.

The TiO_x thin film growth was performed by CVD using TTIP (Sigma Aldrich, purity 99.999%) as precursor. TTIP was dosed from a glass tube mounted on a leak valve which was connected to a stainless steel tube doser. The doser opening was positioned about 5 cm from the crystal surface. The dosing pressure was about $2 \cdot 10^{-8}$ mbar. The TTIP was thoroughly purified by freeze–pump–thaw cycles and the gas line was baked in order to remove water prior to deposition.

Growth series of TiO_x thin films were conducted in a stepwise manner, where small amounts of TTIP were dosed with the sample kept at selected temperatures followed by cooling down to room temperature (RT) for characterization by HRPES or STM and LEED. Before any measurements, each deposition was followed by a flash to the deposition temperature when all TTIP remnants had been pumped out in order to remove unreacted TTIP adsorbed on the surface while cooling down.

The Pd 3d core level spectrum of Pd(111) has a surface contribution, which can be identified for spectra measured at 400 eV. The relative intensity of the surface component was utilized to estimate the amount of surface covered by the TiO_x thin films. The film thicknesses were estimated by the attenuation of the Pd $3d_{5/2}$ bulk peak measured with a photon energy of 460 eV, taking uncovered areas into account if present. The Pd $3d_{5/2}$ spectra of the clean Pd(111) surface was fitted according to the procedure by Göthelid et al. [27, 28]. This means that three Doniach-Sunijc line profiles was used, one for the bulk peak at 334.86 eV, one for the surface contribution, shifted -0.28 eV to lower binding energy compared to the bulk peak, and a third peak shifted 0.4 eV to higher binding energy compared to the bulk component, representing the rapidly varying density of states around the Fermi level [28–30].

3 Results and discussion

3.1 Thin film growth by TTIP CVD on Pd(111)

TiO_x was grown on Pd(111) by CVD at substrate temperatures ranging from 300°C to 500°C. The temperature dependent growth behaviour was found to be very similar to corresponding TiO_x thin film growth on Pd(100) [1]: Carbon containing species resulting from the decomposition of TTIP remaining adsorbed on the Pd(111) surface at temperatures below 500°C. At 500°C the TiO_x structures were grown without any carbon residues. The observed TiO_x structures were the same for the different temperatures as judged from LEED.

The LEED patterns recorded at temperatures below 500°C were however more diffuse, indicating less ordered structures. Thus, to ensure complete precursor reaction and to present results from well-ordered thin film structures, we have chosen to focus on the 500°C growth series in this work.

Ti $2p_{3/2}$ and Pd $3d_{5/2}$ core level spectra recorded after stepwise thin film deposition performed at 500°C, including curve fittings, are displayed in Fig. 1. As will be discussed below, four different contributions are identified in the Ti $2p_{3/2}$ spectra depending on TiO_x coverage. Generally, the HRPES results show strong similarities to the results reported for TiO_x thin films grown on Pd(100) by the same method [1].

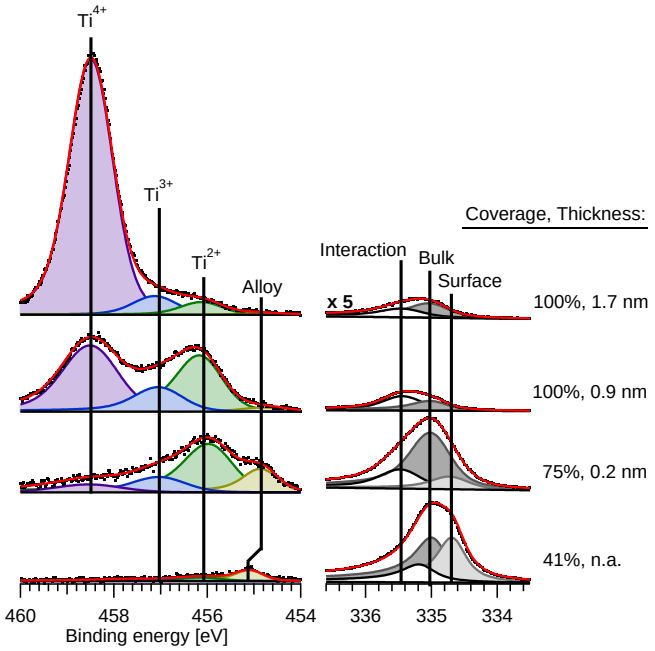

Figure 1. Selected Ti $2p_{3/2}$ (left) and Pd $3d_{5/2}$ (right) core level spectra from a TiO_x thin film growth series performed the 500°C. The surface coverage and average TiO_x film thickness is given on the right side of the plotted spectra.

At the lowest coverages investigated, a single contribution to the Ti $2p_{3/2}$ core level spectrum at binding energy 455 eV is observed. This state is indicated in yellow in the left part of Fig. 1. At this point, no evidence for presence of oxygen is discernible in the O 1s spectra. It should however be noted that the identification of oxygen species is hampered by the overlap with the Pd $3p_{3/2}$ core level contribution. The corresponding Pd $3d_{5/2}$ spectrum displays a reduced surface contribution as well as an increased relative intensity of the high binding energy contribution, in this case shifted 0.2 eV

to higher binding energy compared to the bulk component. These findings indicate formation of a Pd-Ti alloy in the surface region. This conjecture is supported by comparing to measurements conducted on Pd-Ti alloys [31] where a binding energy shift of about 0.86 eV for Ti in a Pd_3Ti alloy was reported compared to the Ti $2p_{3/2}$ core level binding energy in pure Ti. For alloys with higher Ti content smaller shifts were reported [31]. The observed shift towards lower binding energy for increasing alloy content seen in Fig. 1 is consistent with these findings.

STM images of the alloy phase are presented in Fig. 2. As compared to the clean Pd(111) surface, displaying flat, featureless terraces at this magnification and rather straight step edges, two distinct features can be discerned. The STM results reveal areas of alloy formation on the terraces as well as growth of this phase from step edges. Noteworthy is the quite irregular step edges, showing that steps are strongly affected by the alloy formation. Darker spots distributed on the terraces are also seen for the alloy phase, which could be a signature of smaller ensembles of Ti atoms serving as nucleation sites for the more extended alloy areas. The alloy island formation may be explained by the concentration dependency of the ordering energy, driving a nonstoichiometric alloy to undergo phase separation [32]. In the present case, the Ti content is much less than what is required to form a surface alloy covering the entire sample resulting in islands of what is likely to be a Pd_3Ti alloy, as judged by the phase diagram of Pd-Ti alloys [33] and the observed binding energy of the Ti $2p_{3/2}$ peak.

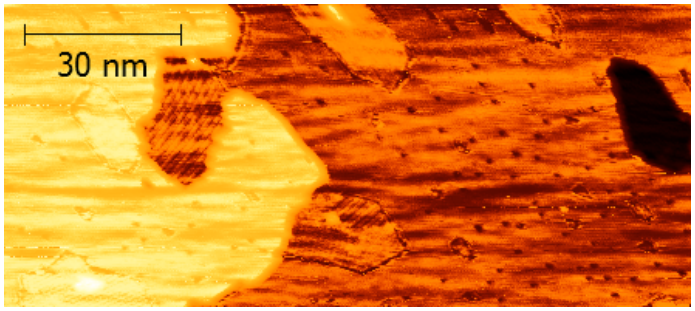

Figure 2. STM image of the alloy phase formed at low coverage of Ti deposited on Pd(111). Embedded domains as well as small dark spots on the terraces can be identified. The Pd step edges are irregular compared to the step edges of clean Pd(111), showing that the development of the Pd-Ti alloy is strongly affecting the step structure.

Upon increasing the amount of TiO_x deposited on the Pd(111) surface, new spectral contributions appear in the Ti $2p_{3/2}$ core level spectra. The second contribution developing has a binding energy of 456.1 eV and is colored green in Fig. 1. The binding energy of this component suggests that the oxidation state is somewhere between Ti^{2+} and Ti^{3+} [24]. For convenience this peak has been labeled Ti^{2+} and it is thus the signature of a partially oxidized phase,

TiO_x with x<2. A clear O 1s peak is observed at this point and a new, distinct LEED pattern has evolved, which is displayed in Fig. 3. The unit cell derived from the LEED pattern is a rectangular incommensurate cell, rotated about 8° with respect to the Pd(111) unit cell. No major changes are seen in the Pd $3d_{5/2}$ core level spectra except for further decrease in the surface contribution and relative growth in intensity of the high binding energy contribution which also moves in binding energy, yielding a shift of 0.45 eV compared to the bulk peak. From the attenuation of the Pd $3d_{5/2}$ bulk contribution a thickness of about 0.2 nm is estimated.

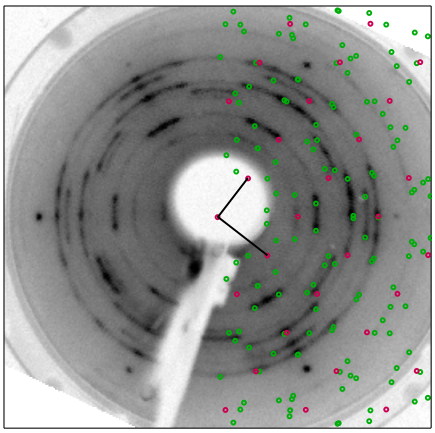

Figure 3. LEED pattern for the partially oxidized phase (TiO_x; x<2). The simulated LEED pattern based on a rectangular unit cell is superimposed on the right half of the pattern. The reciprocal unit cell vectors are indicated by black lines, and spots from one domain orientation are colored in red.

STM images recorded of the partially oxidized phase, displayed in Fig. 4, reveal a wetting layer consisting of domains rotated by 60°and about 15°, where the latter is a result of the 8° rotation relative to the Pd(111) substrate. The atomic structure consists of double rows, where the STM contrast shows a zigzag pattern. This structure strongly resembles the structure observed for partially oxidized TiO_x layers grown on Pd(100) [1] and the z-phase on Pt(111) [24], except that the zigzag pattern for Pd(111) is constructed by one row less. The observation of these row structures with zigzag patterns in the STM contrast on both (111) and (100) surfaces indicates that this type of structures is an inherent property of the partially oxidized TiO_x wetting layers formed on substrate with which there is a strong interaction, recognized by a tendency to form bimetallic alloys.

Further deposition of TTIP results in a TiO_x film with increasing level of oxidation, manifested by two additional contributions appearing in the Ti $2p_{3/2}$ core level spectra, one peak at binding energy 457.0 eV (indicated in blue in Fig. 1) and one peak at binding energy 458.5 eV (marked in purple in Fig. 1). These two contributions are known to correspond to Ti^{3+} and

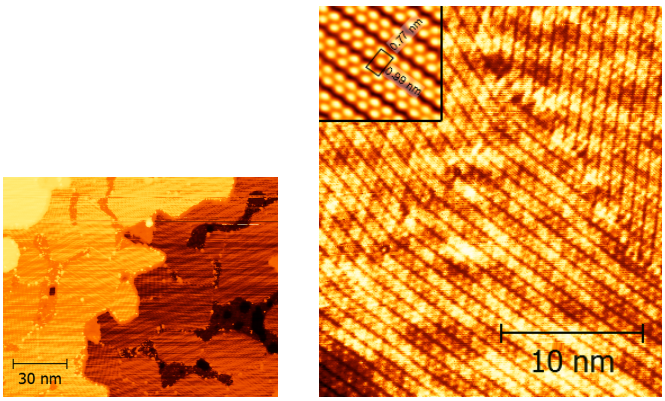

(a) (b)

Figure 4. STM images of the partially oxidized phase TiO_x with x<2. (a) The partially oxidized phase covering most of the surface. The step edges are highly influenced by the TiO_x growth. (b) Close up of three domains in the partially oxidized wetting layer, two are rotated by 60°, and the last one by about 15°. The inset shows a section from the center domain. The periodic features have been enhanced by FFT filtering and the unit cell derived from the corresponding LEED pattern, shown in Fig. 3, is superimposed.

Ti^{4+}, respectively [24]. The Ti^{3+} contribution is relatively stronger at the lower coverages. This contribution has previously been attributed to defect states in deposited TiO_2 thin films [21, 34], but also been attributed to a transition layer between the partially oxidized TiO_x wetting layer and the fully oxidized TiO_2 phase grown on Pd(100) [1]. The Ti^{4+} peak, which is the signature of a fully oxidized TiO_2 phase being formed, dominates the Ti $2p_{3/2}$ spectrum for increasing film thickness and is accompanied by the appearance of a new LEED pattern, which is displayed in Fig. 5. Rotations relative to the Pd(111) unit cells observed for the partially oxidized phase are not observed for the fully oxidized phase. A matter of fact, the LEED pattern has a striking resemblance to the one representing the TiO_2(B) phase on Pt(111) [25] and on Au(111) [23]. In the case of Au(111), the unit cell vectors resulting from the LEED pattern are a= 3.75 Å and b= 6.38 Å with $\alpha = 107.1°$ [23], while the corresponding vectors obtained from Fig. 5 are a= 4.15 Å and b= 7.03 Å, i.e. unit cell vectors which are 10% longer than those describing the TiO_2(B)(001) Type 1 termination [35]. This expansion is too large to draw the conclusion that this TiO_2 phase has a TiO_2(B)(001) structure, based on the LEED results only.

Overall, the TiO_x thin film growth on Pd(111) is chemically very similar to the growth observed on Pd(100). At the lowest coverages an alloy phase is formed, followed by formation of a partially oxidized wetting layer, TiO_x with x<2. On top of this wetting layer a fully oxidized phase TiO_x forms. As seen for Pd(100) [1], the Ti $2p_{3/2}$ core level spectra indicate that the Ti^{3+} species

appear primarily in a transition region between the wetting layer and the fully oxidized phase. Turning to the observed thin films structures, the surface unit cell difference of the two substrates must be taken into consideration. The Ti-Pd alloy formation appears to be quite different on the Pd(111) surface compared to the Pd(100) surface. STM indicates that there are well defined domains in the outer surface layer and a substantial rearrangement of the Pd step edges on Pd(111) in contrast to the apparently evenly distributed second layer alloy observed on Pd(100) [1]. This difference may however, at least partly, be due to the alternative preparation method used to examine the Ti-Pd alloy on Pd(100) by STM. For the partially oxidized TiO_x wetting phase, the STM images indicate similar zigzag type structures, but with different number of rows, 2 vs 3, making up the zigzag structure. The LEED patterns are not able to pick up these similarities both due to different substrates and different unit cells for the thin films. Finally, the fully oxidized phases display different LEED patterns revealing completely different unit cells indicating that there are at least different exposed surfaces if not two completely different structures. To determine the TiO_2 thin film structures additional STM investigations are called for.

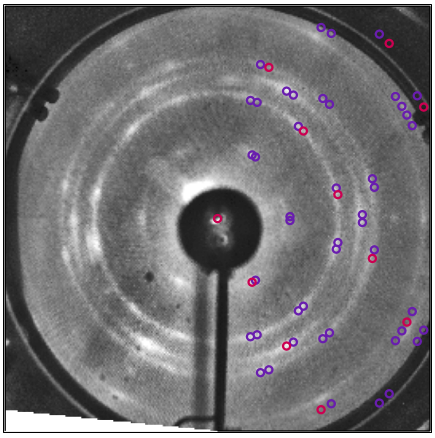

Figure 5. LEED pattern of the fully oxidized phase. The superimposed LEED pattern, overlayed on the right half side, reveals a unit cell which is 10% larger than the TiO_2(B)(001) unit cell.

3.2 Oxidation, reduction and re-oxidation of as-deposited, partially oxidized TiO_x thin films

For catalytic applications the oxidation/reduction behavior of the catalyst system is of high significance for the reactivity. For the TiO_x thin film phases grown on Pd(111) we have addressed this issue through examining the behavior in terms of oxidation and reduction more closely for the partially oxidized phase. A preparation consisting of the partially oxidized phase covering about 95% of the Pd(111) surface was prepared. The observed LEED pattern for

the preparation was the same as the one in Fig. 3. The Ti $2p_{3/2}$ and Pd $3d_{5/2}$ core level spectra of the as prepared TiO_x thin film are displayed in Fig. 6 together with the spectra recorded after each oxidation and reduction step, as described in the following.

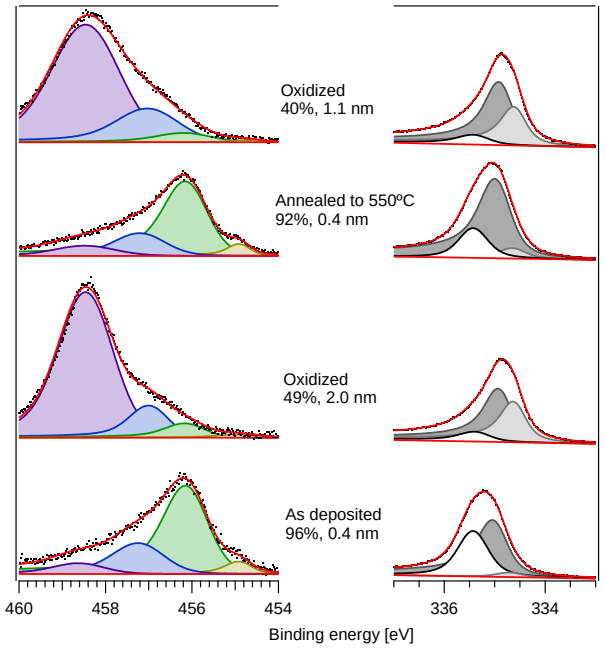

Figure 6. Ti $2p_{3/2}$ (left) and corresponding Pd $3d_{5/2}$ (right) spectra after oxidation, reduction and re-oxidation of the partially oxidized phase. The spectra for the as deposited film are also presented for comparison. Surface coverage and thin film thickness are indicated for each step.

The as prepared phase was oxidized at 500°C in $5 \cdot 10^{-7}$ mbar of oxygen. This procedure is denoted post-oxidation. As is evident from the Ti $2p_{3/2}$ spectrum, the oxidation resulted in a film of fully oxidized TiO_2, although some Ti^{3+} and Ti^{2+} species were still present. Noteworthy is the absence of any alloy contribution to the spectrum. The intensity of the Ti^{2+} contribution is consistent with the wetting layer residing underneath the fully oxidized phase. This interpretation is corroborated with changes observed in the Pd $3d_{5/2}$ spectrum, where the surface contribution has grown significantly revealing uncovered surface areas on Pd(111), and the interaction peak at the high binding energy side has decreased significantly indicating that the partially oxidized wetting layer is almost gone. The TiO_2 phase covers only 49% of the surface area. Furthermore the thickness of the film has increased substantially, suggesting formation a structure consisting of tall islands, which may also explain the relatively higher amount of Ti^{3+} species being present,

tentatively assigned to undercoordinated TiO_2 sites associated with the island structure. The accompanying LEED pattern is a combination of the moire pattern presented in Fig. 7 and an additional unknown structure. The extra spots do not coincide with any of the known structures of oxygen on Pd(111) [36]. However, the LEED pattern of the rect-TiO_2 structure seen on Pt(111) [24] is a potential match. Thus, the fully oxidized phase formed upon oxidation of a partially oxidized thin film is quite different from the fully oxidized phase obtained by the CVD growth.

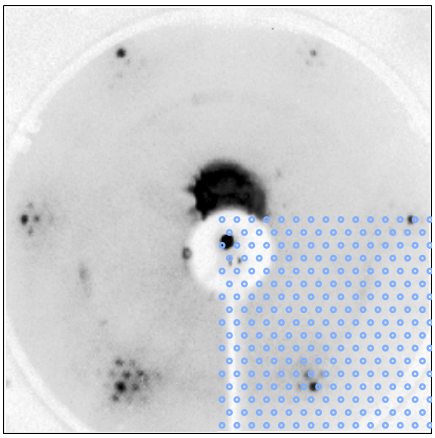

Figure 7. LEED image recorded after re-oxidation (second oxidation in this case) of the partially oxidized phase. The simulated (13x13) LEED pattern is overlayed the bottom right quarter of the LEED image.

As the second step, the preparation was annealed in UHV. During the annealing, which was performed by gradually increasing the sample temperature, the Ti $2p_{3/2}$ core level region was monitored. At temperature 550°C a Ti $2p_{3/2}$ spectrum similar to that of the as prepared film had developed (shown in Fig. 6) and the annealing was stopped. The resulting LEED pattern was, except for having more well-defined peaks, identical to the pattern observed for the as grown partially oxidized phase, see Fig. 3. Both surface coverage and film thickness were similar to before oxidation. This cycle can be repeated, as illustrated by the Ti $2p_{3/2}$ and Pd $3d_{5/2}$ core level spectra recorded after a second oxidation, referred to as re-oxidation, at the same conditions as applied during the first oxidation step, however, with a slight reduction in the Ti 2p signal. After re-oxidation the LEED pattern displayed in Fig. 7 was observed. This LEED pattern appear to be a moire-pattern with (13x13) periodicity with the Pd(111) substrate.

Preparations which predominantly consist of the alloy phase, i.e. lower initial TiO_x coverage, were investigated in the same manner. Upon oxidation the same LEED pattern as presented in Fig. 7 was obtained. An annealing temperature of 545°C was required to reach a similar alloy phase contribution in the Ti $2p_{3/2}$ spectrum, while a spectrum similar to the one recorded for

the reduced phase in Fig. 6 resulted after annealing to 500°C. Thus, a fully reduced alloy phase can be obtained upon reduction in UHV, however, the temperature at which the partial and full reduction occur depends on the initial amount of TiO_x thin film deposited.

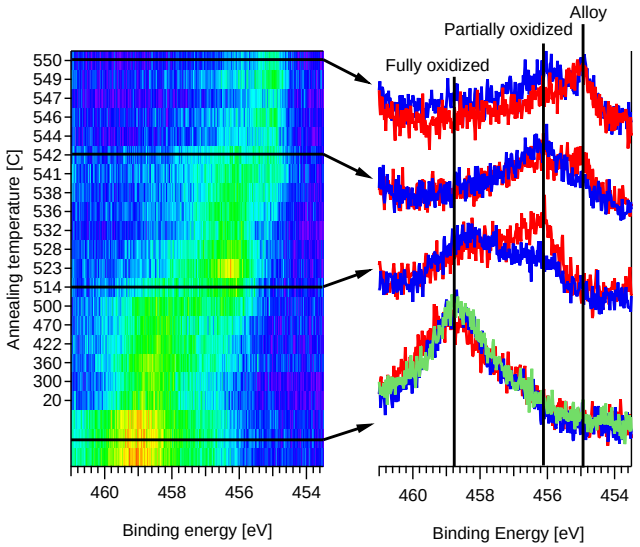

Figure 8. Ti $2p_{3/2}$ spectra recorded during annealing in UHV of a TiO_x thin film prepared by CVD followed by oxidation at 500°C. On the right side single spectra for selected temperatures are compared to the corresponding spectra of the same preparation when annealed in CO. The red spectra are from annealing the UHV and blue spectra are from annealing in CO. The green spectrum was measured prior to introduction of CO in the annealing in CO series.

Another question regarding the rediction of the TiO_x thin film phases on Pd(111), is if the fully (and partially) oxidized phases are affected by adding a model reactant during annealing. The results of such an experiment are shown in Fig. 8, where an as prepared TiO_x thin film with a significant alloy phase content has been oxidized, according to the procedure described above, and subsequently reduced in UHV and in $5 \cdot 10^{-8}$ mbar of CO. The Ti $2p_{3/2}$ core level region was recorded during the annealing sequences, shown in the left panel of Fig. 8 for the experiment performed in UHV. Line spectra measured at selected temperatures are compared in the right panel of Fig. 8. The red spectra show results for the annealing in UHV while the blue lines are measurements during annealing in CO. The green spectrum superimposed the room temperature spectra is the spectrum recorded before introducing CO in the CO annealing series, shown to illustrate that introduction of CO itself at this temperature does not cause any reduction of the fully oxidized TiO_2 phase. The experimental results reveal that reduction proceeds similarly in

the presence of CO. The main difference is that a slightly higher annealing temperature is required to reach the same oxidation state compared to annealing in UHV. Whether CO actually stabilizes the film or if this is simply an effect of the pressure during the experiments is not yet established.

The different structures and oxidation states available by TiO_x thin film phases grown on Pd(111), in combination with post-oxidation and reduction, provide a versatile model system for investigating selected catalytic reactions. The Ti oxidation state of the thin films can be tailored, which allows for tuning the influence of the oxide as source and reservoir for oxygen in oxidation and reduction reactions. Moreover, post-oxidation in this case yields relatively large clean Pd(111) areas in between tall TiO_2 structures, a configuation which is particularly suited for addressing the influence of boundaries between the oxide particles and the metal substrate on reactivity. Systems such as FeO on Pt [15, 16] and Au on TiO_2 [19] with high activity towards CO oxidation give an idea of what is possible address, both in terms of understanding the underlying mechanisms and for tailoring future catalysts by studying these types of systems.

4 Conclusion

An alloy phase, a partially oxidized phase (TiO_x; x<2) and a fully oxidized (TiO2 phase), are observed upon growth of TiO_x thin films on Pd(111) by CVD using TTIP as precursor. HRPES results show that these phases chemically are quite similar to those observed for growth of TiO_x thin films on Pd(100) [1]. The LEED pattern recorded of the fully oxidized phase suggests that this phase may have a TiO_2(B)(001) structure, with an expanded unit cell. The partially oxidized phase forms a wetting layer with a rectangular unit cell, as determined by LEED, consisting of a double row zigzag structure at the atomic level. Oxidation of this partially oxidized phase yields a different fully oxidized phase, which only partly covers the Pd(111) surface. This phase may also be reversibly reduced back to the original phase. The combination of an easily and reversibly oxidizable phase with exposed Pd areas makes the partially oxidized TiO_x phase on Pd(111) promising as a model catalyst.

References

[1] M. H. Farstad, D. Ragazzon, M. D. Strømsheim, A. Borg, A. Sandell, *In manuscript* (2014).

[2] W. Wu, H. Jiang, *Acc. Chem. Res.* **45**, 1736 (2012).

[3] J. Szanyi, W. Kuhn, D. Goodman, *J. Phys. Chem.* **98**, 2978 (1994).

[4] D. Teschner, J. Borsodi, A. Wootsch, Z. Révay, M. Hävecker, A. Knop-Gericke, S. D. Jackson, R. Schlögl, *Science* **320**, 86 (2008).

[5] M. A. Henderson, *Surf. Sci. Rep.* **66**, 185 (2011).

[6] L. Millard, M. Bowker, *J. Photochem. Photobiol. A Chem.* **148**, 91 (2002).

[7] P. Panagiotopoulou, D. I. Kondarides, *Catal. Today* **112**, 49 (2006).

[8] P. Panagiotopoulou, *J. Catal.* **225**, 327 (2004).

[9] L. Fan, K. Fujimoto, *Bull. Chem. Soc. Jpn.* **67**, 1773 (1994).

[10] M. Spencer, *J. Catal.* **93**, 216 (1985).

[11] T. Suzuki, R. Souda, *Surf. Sci.* **448**, 33 (2000).

[12] O. Dulub, W. Hebenstreit, U. Diebold, *Phys. Rev. Lett.* **84**, 3646 (2000).

[13] M. Bowker, P. Stone, P. Morrall, R. Smith, R. Bennett, N. Perkins, R. Kvon, C. Pang, E. Fourre, M. Hall, *J. Catal.* **234**, 172 (2005).

[14] M. Bowker, E. Fourré, *Appl. Surf. Sci.* **254**, 4225 (2008).

[15] Y.-N. Sun, Z.-H. Qin, M. Lewandowski, E. Carrasco, M. Sterrer, S. Shaikhutdinov, H.-J. Freund, *J. Catal.* **266**, 359 (2009).

[16] Y.-N. Sun, L. Giordano, J. Goniakowski, M. Lewandowski, Z.-H. Qin, C. Noguera, S. Shaikhutdinov, G. Pacchioni, H.-J. Freund, *Angew. Chem. Int. Ed. Engl.* **49**, 4418 (2010).

[17] J. A. Rodriguez, S. Ma, P. Liu, J. Evans, M. Perez, J. Hrbek, J. Evans, M. Perez, *Science* **318**, 1757 (2007).

[18] J. Graciani, K. Mudiyanselage, F. Xu, A. E. Baber, J. Evans, S. D. Senanayake, D. J. Stacchiola, P. Liu, J. Hrbek, J. F. Sanz, J. A. Rodriguez, *Science* **345**, 546 (2014).

[19] I. X. I. Green, W. Tang, M. Neurock, J. T. J. Yates, J. T. Y. Jr, J. T. J. Yates, *Science* **333**, 736 (2011).

[20] C. Wu, M. S. J. Marshall, M. R. Castell, *J. Phys. Chem. C* **115**, 8643 (2011).

[21] D. Ragazzon, A. Schaefer, M. Farstad, L. Walle, P. Palmgren, A. Borg, P. Uvdal, A. Sandell, *Surf. Sci.* **617**, 211 (2013).

[22] D. Ragazzon, M. H. Farstad, A. Schaefer, L. E. Walle, P. Uvdal, P. Palmgren, A. Borg, A. Sandell, *In manuscript* (2014).

[23] D. Ragazzon, M. H. Farstad, A. Schaefer, L. E. Walle, P. Uvdal, A. Borg, A. Sandell, *Submitted to Surf. Sci.* (2014).

[24] F. Sedona, G. A. Rizzi, S. Agnoli, F. X. L. i. Xamena, A. Papageorgiou, D. Osterman, M. Sambi, P. Finetti, K. Schierbaum, G. Granozzi, *J. Phys. Chem. B* **109**, 24411 (2005).

[25] E. Cavaliere, L. Artiglia, G. A. Rizzi, L. Gavioli, G. Granozzi, *Surf. Sci.* **608**, 173 (2013).

[26] R. Nyholm, J. Andersen, U. Johansson, B. Jensen, I. Lindau, *Nucl. Inst.Meth. A* **467-468**, 520 (2001).

[27] M. Göthelid, H. von Schenck, J. Weissenrieder, B. Å kermark, A. Tkatchenko, M. Galván, *Surf. Sci.* **600**, 3093 (2006).

[28] M. Göthelid, M. Tymczenko, W. Chow, S. Ahmadi, S. Yu, B. Bruhn, D. Stoltz, H. von Schenck, J. Weissenrieder, C. Sun, *J. Chem. Phys.* **137**, 204703 (2012).

[29] G. Wertheim, P. Citrin, *Photoemiss. Solids I*, M. Cardona, L. Ley, eds. (Springer Berlin Heidelberg, Berlin, Heidelberg, 1978), vol. 26 of *Topics in Applied Physics*, pp. 197–236.

[30] R. Nyholm, M. Qvarford, *J. Phys. Condens. Matter* **4**, 277 (1992).

[31] A. Bzowski, T. Sham, *Phys. Rev. B* **48**, 7836 (1993).

[32] A. Ruban, H. Skriver, J. Nørskov, *Surface Alloys and Alloys Aurfaces*, vol. 10 of *The Chemical Physics of Solid Surfaces* (Elsevier, 2002).

[33] H. Okamoto, *J. Phase Equilibria Diffus.* **34**, 74 (2012).

[34] L. Artiglia, A. Zana, G. A. Rizzi, S. Agnoli, F. Bondino, E. Magnano, E. Cavaliere, L. Gavioli, G. Granozzi, *J. Phys. Chem. C* **116**, 12532 (2012).

[35] M. Ben Yahia, F. Lemoigno, T. Beuvier, J.-S. Filhol, M. Richard-Plouet, L. Brohan, M.-L. Doublet, *J. Chem. Phys.* **130**, 204501 (2009).

[36] G. Zheng, E. Altman, *Surf. Sci.* **462**, 151 (2000).